VILNIUS UNIVERSITY
CENTER FOR PHYSICAL SCIENCES AND TECHNOLOGY

LAIMA RADŽIŪTĖ

RESEARCH ON PARITY AND TIME-REVERSAL VIOLATION IN ATOMIC PHYSICS

Doctoral dissertation
Physical Sciences, Physics (02 P)

Vilnius, 2017

Doctoral Dissertation was completed during 2012-2016 at Vilnius University, Institute of Theoretical Physics and Astronomy.

Scientific supervisor - prof. habil. dr. Gediminas Gaigalas (Vilnius University, Physical sciences, Physics – 02 P).

Scientific consultant - habil. dr. Jacek Bieroń (Poland, Jagiellonian University, Physical sciences, Physics – 02 P).

VILNIAUS UNIVERSITETAS
FIZINIŲ IR TECHNOLOGIJOS MOKSLŲ CENTRAS

LAIMA RADŽIŪTĖ

LYGINUMO IR LAIKO APGRĄŽOS PAŽEIDIMO TYRIMAS ATOMO FIZIKOJE

Daktaro disertacija
Fiziniai mokslai, fizika (02 P)

Vilnius, 2017

Daktaro disertacija rengta 2012-2016 metais Vilniaus universiteto Teorinės fizikos ir astronomijos institute.

Mokslinis vadovas - prof. habil. dr. Gediminas Gaigalas (Vilniaus universitetas, fiziniai mokslai, fizika – 02 P).

Mokslinis konsultantas - habil. dr. Jacek Bieroń (Lenkija, Jogailos universitetas, fiziniai mokslai, fizika – 02 P).

Table of Contents

Publications on the subject of the dissertation

A1 **L. Radžiūtė**, J. Ekman, P. Jönsson, and G. Gaigalas, *Extended calculations of level and transition properties in the nitrogen isoelectronic sequence: Cr XVIII, Fe XX, Ni XXII, and Zn XXIV*, A&A **582**, A61 (2015). Data Tables are available at Strasbourg Astronomical Data Center (CDS) (`http://cdsarc.u-strasbg.fr/viz-bin/qcat?J/A+A/582/A61`).

A2 P. Jönsson, **L. Radžiūtė**, G. Gaigalas, M. R. Godefroid, J. P. Marques, J. Ekman, T. Brage, C. Froese Fischer, and I. P. Grant, *Accurate multiconfiguration calculations of energy levels, lifetimes, and transition rates for the silicon isoelectronic sequence Ti IX Ge XIX, Sr XXV, Zr XXVII, Mo XXIX*, A&A **585**, A26 (2016). Data Tables are available at Strasbourg Astronomical Data Center (CDS) (`http://cdsarc.u-strasbg.fr/viz-bin/qcat?J/A+A/585/A26`).

A3 **L. Radžiūtė**, G. Gaigalas, D. Kato, P. Jönsson, P. Rynkun, S. Kučas, V. Jonauskas, and R. Matulianec, *Energy level structure of* Er^{3+}, J. Quant. Spectrosc. Radiat. Transfer **152**, 94 (2015).

A4 **L. Radžiūtė**, D. Kato, G. Gaigalas, P. Jönsson, P. Rynkun, V. Jonauskas, and S. Kučas, *Energy level structure of the ground configuration in the* Er^{3+} *free ion*, Phys. Scr. **90**, 054001 (2015).

A5 **L. Radžiūtė**, E. Gaidamauskas, G. Gaigalas, J. Li, C. Dong, and P. Jönsson, *Weak- and hyperfine interaction induced* $1s2s\ ^1S_0 \rightarrow 1s^2\ ^1S_0$ *E1 transition rates of He-like ions*, Chin. Phys. B **24**, 043103 (2015).

A6 **L. Radžiūtė**, P. Jönsson, G. Gaigalas, and J. Bieroń, *Multiconfiguration Dirac - Hartree-Fock calculations of atomic electric dipole moments of* ^{225}Ra, ^{199}Hg, *and* ^{171}Yb, Phys. Rev. A **90**, 012528 (2014).

A7 **L. Radžiūtė**, G. Gaigalas, P. Jönsson, and J. Bieroń, *Electric dipole moments of superheavy elements: A case study on copernicium*, Phys. Rev. A **93**, 062508 (2016).

Proceedings

A8 G. Gaigalas, J. Bieroń, and **L. Radžiūtė**, *Multiconfiguration Dirac-Hartree-Fock calculations of EDM for Ra, Hg, Yb*, J. Phys.: Conf. Ser. **488**, 122001 (2014).

Other scientific papers

A9 V. Jonauskas, T. Pütterich, S. Kučas, Š. Masys, A. Kynienė, G .Gaigalas, R. Kisielius, **L. Radžiūtė**, P. Rynkun, and G. Merkelis, *Cascade emission in electron beam ion trap plasma of W^{25+} ion*, J. Quant. Spectrosc. Radiat. Transfer **160**, 22 (2015).

A10 V. Jonauskas, A. Kynienė, G. Merkelis, G. Gaigalas, R. Kisielius, S. Kučas, Š. Masys, **L. Radžiūtė**, and P. Rynkun, *Contribution of high-nl shells to electron-impact ionization processes*, Phys. Rev. A **91**, 012715 (2015).

A11 V. Jonauskas, A. Kynienė, P. Rynkun, S. Kučas, G. Gaigalas, R. Kisielius, Š. Masys, G. Merkelis, and **L. Radžiūtė**, *Theoretical investigation of spectroscopic properties of W^{26+} in EBIT plasma*, J. Phys. B. Mol. Opt. Phys. **48**, 135003 (2015).

Proceedings

A12 V. Jonauskas, A. Kynienė, P. Rynkun, **L. Radžiūtė**, G. Gaigalas, R. Kisielius, S. Kučas, Š. Masys, and G. Merkelis, *Theoretical investigation of spectroscopic properties of W^{27+} ion*, J. Phys.: Conf. Ser. **635**, 052059 (2015).

A13 V. Jonauskas, A. Kynienė, Š. Masys, R. Kisielius, S. Kučas, P. Rynkun, **L. Radžiūtė**, G. Gaigalas, and G. Merkelis, *Theoretical study of W^{27+} spectra in EBIT plasma*, J. Phys.: Conf. Ser. **635**, 052090 (2015).

Conference presentations

C1 G. Gaigalas, J. Bieroń, and **L. Radžiūtė**, *Multiconfiguration Dirac - Hartree - Fock calculations of EDM for Ra, Hg, Yb*, 28th International Conference on Photonic, Electronic and Atomic Collisions (XXVIII ICPEAC), Book of Abstract, 24-30 July, 2013, Lanzhou, (China) Abstract ID 17308.

C2 **L. Radžiūtė**, G. Gaigalas, and J. Bieroń, *Multiconfiguration Dirac - Hartree - Fock calculations of atomic EDM for Ra, Hg, Yb, Xe and Rn,* 40st Lithuanian National Conference of Physics Book of Abstract, 10-12 Ju, 2013, Vilnius, (Lithuania) p. 214.

C3 **L. Radžiūtė**, D. Kato, G. Gaigalas, P. Jönsson, P. Rynkun, V. Jonauskas, and S. Kučas, *Energy levels of* Er^{3+} *free ion*, International Conference on Atomic and Molecular Data and Their Applications (ICAMDATA 90), Book of Abstracts, 21-25 September, 2014 Jena, (Germany) p. 91.

C4 **L. Radžiūtė**, G. Gaigalas, P. Jönsson, and J. Ekman, *Multiconfiguration Dirac-Hartree-Fock computation of energy spectrum of ions: Cu XV, Zn XVI, Ga XVII, and Ge XVIII* 41st Lithuanian National Conference of Physics Book of Abstract, 17-19 June, 2015, Vilnius, (Lithuania) p. 147.

Acknowledgments

I would like to express my special appreciation and thanks to my scientific supervisor prof. habil. dr. Gediminas Gaigalas for the excellent guidance and valuable discussions.

I would like to express my very profound gratitude to my consultant habil. dr. Jacek Bieroń, for all his support, especially during my Erasmus visit.

I would like to thank my colleague dr. Pavel Rynkun for daily discussions and remarks on my PhD thesis.

I would also like to thank prof. Per Jönsson and dr. Jörgen Ekman for the useful and interesting exchanges and collaborations.

I would like to take opportunity to thank all members of the Computational Atomic Structure (CompAS) group.

The author is thankful for the high performance computing resources provided by the Information Technology Open Access Center of Vilnius University.

List of the abbreviations

AS active set
ASF atomic state function
BPRM Breit-Pauli R-matrix
C charge conjugation
CSF configuration state function
EAL extended average level
EDM electric dipole moment
eEDM electron electric dipole moment
EOL extended optimal level
FAC flexible atomic code
GRASP general-purpose relativistic atomic structure package
MBPT many-body perturbation theory
MCDHF multiconfiguration Dirac-Hartree-Fock
MCHF-BP multiconfiguration Hartree-Fock Breit-Pauli
MR multi-reference
MRMP multireference Møller-Plesset perturbation theory
MR-MP multireference many-body perturbation
NIST National Institute of Standards and Technology
NSM nuclear Schiff moment
QED quantum electrodynamics
PNC Parity non-conservation
RCI relativistic configuration-interaction
RMBPT relativistic many body perturbation theory
SCF self-consistent field
SD single double
SE semi-empirical
SrD single restricted double
P Parity
PSS pseudoscalar-scalar
T Time
TPT tensor-pseudotensor

Chapter 1

Introduction

The existence of a non-zero permanent electric dipole moment (EDM) of an elementary particle, or in a nondegenerate system of particles, would be one manifestation of violation of parity (P) and time-reversal (T) symmetries [1, 2]. Violation of P symmetry has been observed in the β-decay of ^{60}Co [3] followed by decay of muons [4] and pions [5]. Violation of charge and parity (CP) symmetry has been observed in the weak decay of neutral kaons K^0 [6]. Both CP and T symmetry violations have been observed in the neutral kaon system [7], although direct T symmetry violation has been disputed [8, 9]. More recently a direct observation of the T symmetry violation in the B meson system has been reported [10].

The violations of P, C, CP, and T symmetries are predicted by the Standard Model of particle physics [11, 12]. **Relevance** of problem is caused by several unexplained issues, such as the origin of baryogenesis, the mass hierarchy of fundamental particles, the number of particle generations, the matter-antimatter-asymmetry observed in the universe, and the nature of the dark matter. These and other issues are addressed within a large number of extensions of the present version of the Standard Model. Several of these extensions predict EDMs induced by the P and T violating interactions and also EDMs of the fundamental particles significantly larger than the values predicted by the Standard Model itself.

The search for a permanent electric dipole moment of an elementary particle, or a composite system of particles (see [1], or reference [13] for a recent review), is a challenge, not only for experiments, but also for theories of composite systems. Electric dipole moments have not yet been detected experimentally. The experimental **searches have been going on for the last 50 years**, and the role of theory is not only to provide the limits on the fundamental parameters, but also to guide the experimentalists to various systems with suitable enhancement factors, such as paramagnetic atoms (thallium experiment [14]),

diamagnetic atoms (mercury [15]), molecules [16, 17], neutrons [18], and other species [1, 19, 20]. Experimentalists need to know (order of magnitude of) enhancement factors before they set up their apparatus to detect EDM in a new species [2]. Heavy atoms are excellent examples of composite systems with large EDMs, due to the existence of mechanisms which may induce atomic EDMs several orders of magnitude larger than an intrinsic particle EDM. The present thesis is intended to present the calculations of EDMs, carried out with the multiconfiguration Dirac-Hartree-Fock theory, of a superheavy element $^{285}_{112}$Cn.

An EDM experiment on a short-lived superheavy element is impractical at this time. However, the techniques for trapping atoms [21, 22], controlling quantum systems [23, 24], and performing spectroscopic investigations of radioactive [25] and superheavy elements [26] advance rapidly. At the same time the quest for the superheavy island of stability continues [27, 28], and sooner or later one may expect a breakthrough of laser spectroscopic methods into the realm of superheavy elements [26]. The EDM experiments with superheavy elements, if ever becoming feasible, would probably constitute the final frontier for atomic tests of violation of parity (P) and time reversal (T) symmetries.

Weak interaction effects in atomic physics play a very important role in searching for new physics beyond the Standard Model of elementary particles. There are several experimental and theoretical investigations of parity violation effects in heavy neutral atoms [19, 29]. However, correlation effects are the main source of uncertainty in theoretical results. Therefore, it looks promising to investigate relatively simple highly charged few-electrons He-like ions in order to minimize the impact of correlation effects.

Radial integrals involving matrix elements of P,T-odd interactions contain factors, which effectively cut-off integration outside the nucleus. These matrix elements require exact radial wave functions at the origin. Meanwhile, radial wave functions for matrix elements of electric dipole moment must be accurate in outer parts of the wave functions. The differences between the transition parameters evaluated with the two gauges can be used as a test of accuracy [30]. N- and Si-like sequences were chosen for this analysis.

Electron correlation effects must be very carefully evaluated in order to obtain accurate atomic state functions, necessary for determination of electric dipole moments. At the same time expansions of configuration state function basis should be reasonable. Er^{3+} ground configuration was chosen for testing correlation effects.

The main goal of present work

- To investigate parity and time-reversal violation in atomic theory, by using multiconfiguration Dirac-Hartree-Fock method, and to suggest most suitable elements for atomic electric dipole moment experiments.

The main tasks of the thesis:

1. To expand multiconfiguration Dirac-Hartree-Fock method:
   - to derive expressions for matrix elements of P,T-odd interactions between states of different parity for multiconfiguration Dirac-Hartree-Fock method;
   - to create programs and tools for computation of these matrix elements;
   - to test programs and tools created for electric dipole moment investigations.
2. To perform large scale calculation for atomic parameters of light and heavy ions:
   - to investigate properties of N-like isoelectronic sequence in nonorthogonal orbital basis;
   - to study parameters of ions in Si-like isoelectronic sequence;
   - to investigate energy spectrum of ground configuration for Er^{3+} ion.
3. To analyse transitions in He-like isoelectronic sequence induced by a weak interaction parity nonconserving term:
   - to identify Z and N dependence of transition probability induced by a P-odd term;
   - to analyse influence of quantum electrodynamic effects on energy spectrum and transition probabilities;
   - to evaluate results, comparing with theoretical computations by other authors.
4. To investigate permanent electric dipole moments of heavy elements:
   - to perform research on electric dipole moments of Hg, Yb, and Ra elements;
   - to analyse electric dipole moment dependence on Z in homologous sequence: Zn, Cd, Hg, Cn;
   - to evaluate results, comparing with data from other theoretical computations.

The scientific novelty

1. Full set of atomic data: excitation energies, A_J and B_J hyperfine constants, Landé g_J-factors, mass- and field shift parameters, E1, E2, and M1 transition parameters, were computed for the first time with *ab initio* method for ions Cr XVIII, Fe XX, Ni XXII, and Zn XXIV in very high precision, and may serve as benchmarks for other calculations.

2. All energy levels for $3s^2 3p^2$, $3s3p^3$, and $3s^2 3p3d$ configurations, and transitions properties (excitation energies, lifetimes and transition rates) between these configurations were computed for the first time for the Si-like ions Ti IX - Ge XIX, Sr XXV, Zr XXVII, and Mo XXIX. Energies are in excellent agreement with observations (up to 0.03%) and computed wavelengths are almost of spectroscopic accuracy, and may serve as benchmark for other calculations.

3. The energy spectrum of the [Xe]$4f^{11}$ configuration of the Er^{3+} ion was computed in *ab initio* method for the first time in very high accuracy and at the same time the influences of different types of correlation effects on energy levels were estimated.

4. Weak and hyperfine interaction induced $1s2s\ ^1S_0 \rightarrow 1s^2\ ^1S_0$ E1 transition rates were computed with *ab initio* method for the He-like isoelectronic sequence, and for the first time exponential Z-dependence of matrix element for weak interaction was observed.

5. Calculation of atomic electric dipole moment arising from P,T-odd tensor-pseudotensor and pseudoscalar-scalar electron-nucleon interactions, nuclear Schiff moment, and interaction of electron electric dipole moment with nuclear magnetic field for $^{285}_{112}$Cn were performed for the first time.

6. Exponential Z-dependence of atomic electric dipole moment in homologous sequence (Zn, Cd, Hg, Cn) was determined for the first time.

Statements to defend

1. $^{151}_{63}$Eu, $^{155}_{64}$Gd, $^{229}_{90}$Th and $^{231}_{91}$Pa ions of He-like isoelectronic sequence are the most promising candidates for experiments of parity nonconservation effects, due to the high values of the weak and hyperfine interaction induced transition rates.

2. Electric dipole moment of an atom arising from parity and time symmetries violating tensor-pseudotensor, pseudoscalar-scalar nucleon-electron interactions, as well as nuclear Schiff moment, and electron electric dipole moment, have exponential dependence on atomic number Z.

3. Isotopes of superheavy elements No, Cn, Nh, Lv, Ts, Og, E119, and E120 with sufficiently long half-lives would be most suitable for searching for parity and time nonconservation in atomic experiments, because their EDM enhancement factors are of the order of 30 times bigger than those of currently studied systems.

Personal contribution

I have participated in computation, collected and analysed data from references for the Tables in paper and in Strasbourg Astronomical Data Center (CDS), prepared manuscript of article **A1** and have led submission procedure. I have performed part of computation and analysis of energy spectrum and transition parameters analysis in **A2**. I have done analysis of energy spectrum, as well as of *LSJ* and *jj* applicability in **A3**. I have been involved in analysis of data, preparation of paper **A4** and its submission. I have written parts of the manuscript **A5** and I have done analysis of the results. I have participated in the creation of programs for EDM computations and of electron correlation strategies. I have performed computations for EOL analysis, and Rydberg series analysis. I prepared first manuscript of **A6** article and lead submission procedure. I have improved electron correlation strategy and computed EDMs of $^{69}_{30}$Zn, $^{111}_{48}$Cd, $^{199}_{80}$Hg, $^{285}_{112}$Cn. I took part in all steps of preparation and submission of manuscript **A7**.

Thesis outline

The doctoral dissertation consist of 8 chapters. Chapter 1 introduces research problem, actuality, scientific novelty, main goal and tasks of study, and statements for defence. Chapter 2 describes different terms of the weak interaction Hamiltonian, represented by neutral currents: parity nonconserving (P-odd) vector-pseudovector product (vector-axial vector), parity and time-reversal symmetry violating (P,T-odd) tensor-pseudotensor and pseudoscalar-scalar terms. The remaining part of chapter 2 is dedicated to description of MCDHF method and the theory of weak and hyperfine interaction induced transition probabilities, as well as Schiff moment and electron electric dipole moment. In Chapter 3 atomic properties for N- and Si-like isoelectronic sequences are presented. In Chapter 4 the results of calculations for energy spectrum of Er^{3+} ion ground configuration are presented. In Chapter 5 results of vector-pseudovector (vector-axial vector) product in weak interaction induced transitions in He-like ions are presented. This term of weak interaction mixes states of opposite parity. Vector-pseudovector is usually called - parity nonconserving weak interaction, so in this work this convention will be followed. Chapter 6 presents the analysis of the calculations performed for the electric dipole moments. Chapter 7 is the continuation of the research on electric dipole moments, but from a different perspective. The main goal of this chapter are suggestions of isotopes suitable for EDM experiments. The last chapter presents main conclusions.

Chapter 2

Theoretical background

2.1 Weak interaction [A5, A6]

Beta decay ($n \to p + e^- + \tilde{\nu}_e$) was postulated by Fermi [31] as a following expression:

$$H_v = \frac{G}{\sqrt{2}}[\overline{p}(x)\gamma_\mu n(x)][\overline{e}(x)\gamma_\mu \tilde{\nu}(x)] + herm.conj. \tag{2.1.1}$$

Here $p(x), n(x), e(x), \tilde{\nu}(x)$ are wave functions of corresponding particles, and G is constant characterizing the interaction strength, γ_μ are Dirac matrices, and all particles interact at the same point (x) of space and time. This expression is scalar product of two four-vectors or two charged currents. Later this expression of beta decay was extended to:

$$H_\beta = \frac{G}{\sqrt{2}}[\overline{p}(x)(1+\lambda\gamma_5)n(x)][\overline{e}(x)\gamma_\mu(1+\gamma_5)\tilde{\nu}_e(x)] + herm.conj, \tag{2.1.2}$$

here $\lambda = 1.25$, $\gamma_5 = -i\gamma_0\gamma_1\gamma_2\gamma_3$. This expression is a scalar product, but now each of them is constructed as linear combinations of vector and axial vectors, which behave differently under coordinate reversal. This Hamiltonian violates parity, by not transforming into itself under space inversion.

Later the interaction of neutral currents was added to the weak interaction charged currents. It is mediated by Z neutral boson and does not change the charges of particles (proton (p) or neutron (n)):

$$\begin{aligned}
\hat{H}_{e-p}(x) \;=\; & G_S p\bar{(x)}p(x)\bar{e}(x)e(x) + G_P\bar{p}\gamma_5 p\bar{e}\gamma_5 e \\
& + G_V\bar{p}\gamma_\mu p\bar{e}\gamma_\mu e + G_A\bar{p}\gamma_\mu\gamma_5 p\bar{e}\gamma_\mu\gamma_5 e + G_T\bar{p}\sigma_{\mu\nu}p\bar{e}\sigma_{\mu\nu}e \\
& + G'_V\bar{p}\gamma_\mu p\bar{e}\gamma_\mu\gamma_5 e + G'_A\bar{p}\gamma_\mu\gamma_5 p\bar{e}\gamma_\mu e \\
& + iG'_S\bar{p}p\bar{e}\gamma_5 e + iG'_P\bar{p}\gamma_5 p\bar{e}e + iG'_T\bar{p}\gamma_5\sigma_{\mu\nu}p\bar{e}\sigma_{\mu\nu}e.
\end{aligned} \tag{2.1.3}$$

Here we will consider only electron-nucleons (e-N) interaction. The general expression of weak e-N interaction due to the exchange of neutral Z^0 bosons between the electron and nucleus can be written according to [1, 29, 20]:

$$\begin{aligned}\hat{H}_{e-N}(x) \;=\; & \\ & \sum_{i=1}^{A}(G_S\bar{N}_iN_i\bar{e}e + G_P\bar{N}_i\gamma_5N_i\bar{e}\gamma_5e \\ & + G_V\bar{N}_i\gamma_\mu N_i\bar{e}\gamma_\mu e + G_A\bar{N}_i\gamma_\mu\gamma_5N_i\bar{e}\gamma_\mu\gamma_5e + G_T\bar{N}_i\sigma_{\mu\nu}N_i\bar{e}\sigma_{\mu\nu}e \\ & + G'_V\bar{N}_i\gamma_\mu N_i\bar{e}\gamma_\mu\gamma_5e + G'_A\bar{N}_i\gamma_\mu\gamma_5N_i\bar{e}\gamma_\mu e \\ & + iG'_S\bar{N}_iN_i\bar{e}\gamma_5e + iG'_P\bar{N}_i\gamma_5N_i\bar{e}e + iG'_T\bar{N}_i\gamma_5\sigma_{\mu\nu}N_i\bar{e}\sigma_{\mu\nu}e). \end{aligned} \tag{2.1.4}$$

N_i represents neutron and protons, $\sigma_{\mu\nu} = 1/2(\gamma_\mu\gamma_\nu - \gamma_\nu\gamma_\mu)$ and $i = \sqrt{-1}$ is the imaginary unit, the sum is taken over all nucleons in nucleus. G_S, G_P, G_V, G_A, G_T are coupling constants, describing strengths of interactions. The indices are derived from descriptors of nucleon-nucleon interactions (scalar, pseudo-scalar, vector, axial, and tensor, respectively). Usually these constant are expressed in terms of Fermi's constant G_F and C_S, C_P, C_V, C_A, and C_T. This interaction is considered to be local (all four particles interact at point x). The last five terms of equation (2.1.4) are P-odd. These terms have primed constants. To obtain P-odd terms additional matrix γ_5 or $i\gamma_5$ is inserted in to one scalar term of the bilinear structure (with unprimed coupling constant). It should be noted that $\gamma_5^2 = 1$. The last three terms are not invariant under T transformation.

2.1.1 Parity nonconservation

Let us examine P-odd, but T-even terms of equation (2.1.4) of vector and axial vector products (V-A). In this and following sections this term of weak interaction will be called parity nonconserving weak interaction, following [32, 33]

$$\hat{h} = -\frac{G_F}{\sqrt{2}}\sum_{i=1}^{A}(C_V^N\bar{N}_i\gamma_\mu N_i\bar{e}\gamma_\mu\gamma_5e + C_A^N\bar{N}_i\gamma_\mu\gamma_5N_i\bar{e}\gamma_\mu e). \tag{2.1.5}$$

Here $G_F = 1.027\times10^{-5}/m_p^2$ is the Fermi constant. G'_V and G'_A are related to C_V^N and C_A^N in the following way: $G'_V = -\frac{G_F}{\sqrt{2}}C_V^N$ and $G'_A = -\frac{G_F}{\sqrt{2}}C_A^N$. The dimensionless coupling constants C_V^N and C_A^N give different weights to the contributions of protons and neutrons to the parity violating interaction: $C_V^p = 0.04$, $C_V^n = -0.5$,

and $C_A^p = -C_A^n = 0.05$.

In nonrelativistic approximation interaction between nucleons and electrons can by expressed by the nuclear spin-independent Hamiltonian [19, 29]:

$$\hat{h} = -\frac{G_F}{\sqrt{2}}\gamma_5[ZC_V^p\rho_p(r) + NC_V^n\rho_n(r)], \tag{2.1.6}$$

where Z and N are the numbers of protons and neutrons, respectively. Densities $\rho_{n,p}(r) = \rho(r)$ of neutrons and protons are normalized to unity and assumed they coincide; we use the Fermi nuclear density function normalized to unity.

In the lowest order in the electroweak interaction weak charge of the nucleus is:

$$Q_W = Z(1 - 4\sin^2\Theta_W) - N \approx -N. \tag{2.1.7}$$

In our calculations we assumed $\sin^2\Theta_W = 0.2312$ for the Weinberg angle Θ_W [34]. So, according to [19, 29], the Hamiltonian (equation 2.1.6) reduces to (in a.u.):

$$\hat{H}_W \;=\; -\frac{G_F}{2\sqrt{2}}\,Q_W \sum_{j=1}^{M} \gamma_{5\,j}\,\rho\,(r_j)\,. \tag{2.1.8}$$

here M is number of electrons. This interaction mixes atomic states with different parities, but only with the same electron angular momentum (it is a scalar), and also opens new decay channels. The total atomic wave function with mixed parities can be expressed as:

$$\widetilde{\Psi}\,(\gamma PJM_J) \;=\; b_0\Psi\,(\gamma PJM_J) \;+\; \sum_{i=1}^{m} b_i\,\Psi\,(\gamma_i(-P)J_iM_{J_i})\,. \tag{2.1.9}$$

The parity non-conserving interaction, like the off-diagonal hyperfine interaction, is quite weak and the coefficient b_0 of the dominant function can be set to 1 and expansion coefficients can also be perturbatively approximated as:

$$b_i \;=\; \frac{\left\langle \Psi\,(\gamma_i(-P)J_iM_{J_i})\,|\hat{H}_W|\Psi\,(\gamma PJM_J)\right\rangle}{E\,(\gamma PJ) \;-\; E\,(\gamma_i(-P)J_i)}. \tag{2.1.10}$$

For the general tensor operator $\hat{T}_q^k$, the matrix element between states of dif-

ferent parity can be expressed by Wigner-Eckart theorem as:

$$\left\langle \Psi(\gamma PJM_J)\,|\hat{T}^k_0|\Psi(\gamma_i(-P)J_iM_{J_i})\right\rangle \;=$$

$$(-1)^{J-M_J}\;\sqrt{2J+1}\begin{pmatrix} J & k & J_i \\ -M_J & 0 & M_{J_i}\end{pmatrix}\times\left[\Psi(\gamma PJ)\,\|\hat{T}^k\|\Psi(\gamma_i(-P)J_i)\right]. \quad (2.1.11)$$

Applying Wigner-Eckart theorem, the matrix element of the weak interaction operator can be expressed as:

$$\left\langle \Psi(\gamma PJM_J)\,|\hat{H}_W|\Psi(\gamma_i(-P)J_iM_{J_i})\right\rangle = \delta(J,J_i)\delta(M_J,M_{J_i})\left[\Psi(\gamma PJ)\,\|\hat{H}_W\|\Psi(\gamma_i(-P)J_i)\right], \quad (2.1.12)$$

where $\langle\gamma_i J_i\|H_W\|\gamma J\rangle = \sqrt{2J'+1}[\gamma_i J_i\|H_W\|\gamma J]$. Using multiconfiguration expansions the reduced matrix elements of the general spherical tensor operator T^k_q can be expressed by the following equation

$$\left[\Psi(\gamma PJ)\,\|\hat{T}^k\|\Psi(\gamma_i(-P)J_i)\right] \;=\; \sum_{p,i}\,c_pc_i\left[\Phi(\gamma_pPJ)\,\|\hat{T}^k\|\Phi(\gamma_i(-P)J_i)\right]. \quad (2.1.13)$$

Reduced matrix elements of one-electron operator between configuration state functions can be expressed as sums over terms involving single-particle orbitals:

$$\left[\Phi(\gamma_pPJ)\,\|\hat{T}^k\|\Phi(\gamma_i(-P)J_i)\right] = \sum_{a,b} d^k_{ab}(ps)\left[n_a\kappa_a\|\hat{t}^k\|n_b\kappa_b\right], \quad (2.1.14)$$

where $d^k_{ab}(ps)$ are spin-angular coefficients that arise from using Racah's algebra in the decomposition of the many-electron matrix elements [35, 36]. The expressions (2.1.11), (2.1.13) and (2.1.14) are general and can be used for any one-particle operator. The single-particle reduced matrix element can be further factorized into a reduced angular matrix element and a radial integral. Here we give the factorization of the reduced matrix element of the weak interaction ($k = 0$):

$$\left[n_a\kappa_a\|\hat{h}_W\|n_b\kappa_b\right] \;=\; \delta(-\kappa_a,\kappa_b)i\tfrac{G_F}{2\sqrt{2}}Q_W\;\int_0^\infty(P_bQ_a\;-\;P_aQ_b)\;\rho(r)\,dr, \quad (2.1.15)$$

where $i=\sqrt{-1}$ is the imaginary unit. In the radial integral P and Q are the large and small components of the relativistic one-electron radial wave functions, respectively. For the calculations of the matrix elements we extended the

GRASP2K relativistic atomic structure package. The extension, presented in this work, includes programs for the weak interaction matrix elements.

2.1.2 Tensor-pseudotensor interaction

The last term in the expression (2.1.4), one of the possible sources of the EDM in diamagnetic atoms, is the tensor-pseudotensor interaction between electrons and nucleons, violating both parity (P) and time (T)-reversal invariance

$$iG'_T \bar{N} \gamma_5 \sigma_{\mu\nu} N \bar{e} \sigma_{\mu\nu} e, \tag{2.1.16}$$

constant G'_T is replaced by $\frac{G_F}{\sqrt{2}} C_T$. C_T is a dimensionless coupling constant of the TPT interaction and it is of interest for ongoing EDM experiments. It can be expressed as [1, 19]:

$$\hat{H}_{TPT} \;=\; i\sqrt{2} G_F C_T \sum_{j=1}^{M} \left(<\boldsymbol{\sigma}_A> \cdot \boldsymbol{\gamma}_j \right) \rho\left(r_j\right). \tag{2.1.17}$$

A is the number of nucleons, $\boldsymbol{\gamma}_j$ is the Dirac matrix. C_T is equal to zero within the standard model, but it is finite in some theories beyond the standard model of elementary particle physics. According to Dzuba et al [19, 37]:

$$C_T <\boldsymbol{\sigma}_A> = \left\langle C_T^p \sum_p \boldsymbol{\sigma}_p + C_T^n \sum_n \boldsymbol{\sigma}_n \right\rangle, \tag{2.1.18}$$

where $\langle ... \rangle$ represents average over the nuclear state with the nuclear spin $\boldsymbol{I}$. C_T^p and C_T^n are tensor-pseudotensor interaction constants between proton-electron (e-p) and neutron-electron (e-n).

The single-particle reduced matrix element $\left[n_a \kappa_a \| \hat{t}^k \| n_b \kappa_b \right]$ in equation (2.1.14) for the tensor-pseudotensor interaction has the form:

$$\left[n_a \kappa_a \| \hat{h}^1_{TPT} \| n_b \kappa_b \right] = \sqrt{2}\, G_F\, C_T \;<\boldsymbol{\sigma}_A>\; \left[n_a \kappa_a \| i\, \hat{\gamma}^1\, \rho\left(r\right) \| n_b \kappa_b \right] =$$

$$-\sqrt{2}\, G_F\, C_T \;<\boldsymbol{\sigma}_A> \times$$

$$\times \left\{ \left[-\kappa_a \| \sigma^1 \| \kappa_b \right] \int_0^\infty P_b Q_a\, \rho\left(r\right) dr + \left[\kappa_a \| \sigma^1 \| -\kappa_b \right] \int_0^\infty P_a Q_b\, \rho\left(r\right) dr \right\} \tag{2.1.19}$$

where the single-particle angular reduced matrix elements can be expressed as:

$$\begin{aligned}&\left[-\kappa_a\|\sigma^1\|\kappa_b\right] \;=\\ &\frac{\left\langle l_b\tfrac{1}{2}0\tfrac{1}{2}|j_a\tfrac{1}{2}\right\rangle\left\langle l_b\tfrac{1}{2}0\tfrac{1}{2}|j_b\tfrac{1}{2}\right\rangle-\left\langle l_b\tfrac{1}{2}1\,-\tfrac{1}{2}|j_a\tfrac{1}{2}\right\rangle\left\langle l_b\tfrac{1}{2}1\,-\tfrac{1}{2}|j_b\tfrac{1}{2}\right\rangle}{\left\langle j_b1\tfrac{1}{2}0|j_a\tfrac{1}{2}\right\rangle},\end{aligned}\tag{2.1.20}$$

$$\begin{aligned}&\left[\kappa_a\|\sigma^1\|-\kappa_b\right] \;=\\ &\frac{\left\langle l_a\tfrac{1}{2}0\tfrac{1}{2}|j_a\tfrac{1}{2}\right\rangle\left\langle l_a\tfrac{1}{2}0\tfrac{1}{2}|j_b\tfrac{1}{2}\right\rangle-\left\langle l_a\tfrac{1}{2}1\,-\tfrac{1}{2}|j_a\tfrac{1}{2}\right\rangle\left\langle l_a\tfrac{1}{2}1\,-\tfrac{1}{2}|j_b\tfrac{1}{2}\right\rangle}{\left\langle j_b1\tfrac{1}{2}0|j_a\tfrac{1}{2}\right\rangle}.\end{aligned}\tag{2.1.21}$$

2.1.3 Pseudoscalar-scalar interaction

The penultimate term in the expression (2.1.4) is also P,T-odd interaction between the electrons and the nucleus:

$$iG'_P\bar{N}\gamma_5 N\bar{e}e. \tag{2.1.22}$$

The Hamiltonian for the pseudoscalar-scalar reads [1, 19]:

$$\hat{H}_{PSS} \;=\; \frac{-G_F\,C_P}{2\sqrt{2}m_pc}\sum_{j=1}^{M}\gamma_0\left(\boldsymbol{\nabla}_j\rho\left(r_j\right)<\boldsymbol{\sigma}_A>\right). \tag{2.1.23}$$

C_P is a dimensionless coupling constant of the *PSS* interaction ($iG'_P=\frac{-G_F}{\sqrt{2}}C_P$).

Analogously to the TPT interaction, C_P constant is zero within the standard model. According to Dzuba et al [37]

$$C_P<\boldsymbol{\sigma}_A>=\left\langle C_P^p\sum_p\boldsymbol{\sigma}_p+C_P^n\sum_n\boldsymbol{\sigma}_n\right\rangle, \tag{2.1.24}$$

C_P^p and C_P^n are PSS interaction constants between e-p and e-n.

The single-particle reduced matrix element $\left[n_a\kappa_a\|\hat{t}^k\|n_b\kappa_b\right]$ in the equation (2.1.14) for the pseudoscalar-scalar interaction has the following form:

$$\begin{aligned}\left[n_a\kappa_a\|\hat{h}^1_{PSS}\|n_b\kappa_b\right]&=-\frac{G_F\,C_P}{2\sqrt{2}m_pc}<\boldsymbol{\sigma}_A>\left[n_a\kappa_a\|\gamma_0\,\nabla^1\rho\left(r\right)\|n_b\kappa_b\right]=\\ &-\frac{G_F\,C_P}{2\sqrt{2}m_pc}<\boldsymbol{\sigma}_A>\left[\kappa_a\|C^1\|\kappa_b\right]\int_0^\infty\left(P_aP_b\;-\;Q_aQ_b\right)\frac{d\rho\left(r\right)}{dr}\,dr.\end{aligned}\tag{2.1.25}$$

2.2 Computation methods

2.2.1 Multiconfiguration Dirac-Hartree-Fock

In the multiconfiguration Dirac-Hartree-Fock (MCDHF) method [35, 38, 39, 40, 41, 42], an atomic state function (ASF) of parity P, $\Psi(\gamma PJ)$, is expressed as a linear combination of symmetry-adapted configuration state functions (CSFs) with the same parity, $\Phi(\gamma_i PJ)$, i.e.

$$\Psi(\gamma PJ) = \sum_i^{N_{CSF}} c_i \Phi(\gamma_i PJ), \tag{2.2.1}$$

where J is the total angular momentum of the configuration. The multiconfiguration energy functional is based on the Dirac-Coulomb Hamiltonian, given by (in a.u.),

$$\hat{H}_{DC} = \sum_{j=1}^{M} \Big(c\boldsymbol{\alpha}_j \cdot \boldsymbol{p}_j + (\beta_j - 1)c^2 + V(r_j) \Big) + \sum_{j<k}^{M} \frac{1}{r_{jk}}, \tag{2.2.2}$$

where $\boldsymbol{\alpha}$ and β are the fourth-order Dirac matrices, $\boldsymbol{p}$ is the momentum operator, and $V(r_j)$ is the electrostatic electron-nucleus interaction.

In all calculations reported here, the nuclear charge density distribution $\rho(r)$ is normalized to unity two-parameter Fermi function [38]

$$\rho(r) = \frac{\rho_0}{1 + e^{(r-b)/a}}, \tag{2.2.3}$$

where parameters a and b depend on the mass of the isotope.

The configuration state functions $\Phi(\gamma_i PJ)$ are antisymmetrized linear combinations of products of relativistic orbitals:

$$\phi(r) = \frac{1}{r} \begin{pmatrix} P_{n\kappa}(r)\chi_{\kappa m}(\hat{r}) \\ iQ_{n\kappa}(r)\chi_{-\kappa m}(\hat{r}) \end{pmatrix}. \tag{2.2.4}$$

Here κ is the relativistic angular quantum number, $P_{n\kappa}(r)$ and $Q_{n\kappa}(r)$ are the large and small components of radial wave function, respectively, and $\chi_{\kappa m}(\hat{r})$ is the spinor spherical harmonic in the lsj coupling scheme

$$\chi_{\kappa m}(r) = \sum_{m_l, m_s} \langle l1/2 m_l m_s | jm \rangle \, Y_{lm_l}(\theta, \varphi) \xi_{m_s}(\sigma). \tag{2.2.5}$$

The radial functions $P_{n\kappa}(r)$ and $Q_{n\kappa}(r)$ are numerically represented on a logarithmic grid and are required to be orthonormal within each κ symmetry as follows:

$$\int_0^\infty [P_{n'\kappa}(r)P_{n\kappa}(r) + Q_{n'\kappa}(r)Q_{n\kappa}(r)]\,dr = \delta_{n'n}. \tag{2.2.6}$$

In the multiconfiguration self-consistent field (SCF) procedure both the radial functions and the expansion coefficients for the configuration state functions are optimised to self consistency.

Wave functions can be optimised with two forms of the energy functional: Extended Optimal Level (EOL) and Extended Average Level (EAL). Both energy functionals are implemented in the GRASP2K [43, 44] package.

One-electron orbitals based on the EOL form are optimised to minimise the energy functional, which is defined through the equation (39) in reference [38], where generalised weights (equation (40) in ref. [38]) determine a specific atomic state ASF (or a set of ASFs). Consequently, the orbitals in the EOL approach are optimal for a specific atomic state ASF or a set of ASFs.

One-electron orbitals based on the EAL form are optimised to minimise the (optionally weighted) sum of energies of all ASFs which may be constructed from a given set of CSFs, so eventually it yields an (optionally weighted) average energy of a set of atomic states. This approach is computationally much cheaper, but usually less accurate than the approach based on the EOL functional.

2.2.2 Breit interaction

Once a set of radial orbitals has been obtained, configuration interaction calculations can be performed with the RCI program [42]. In RCI calculations the wave function is expanded in terms of CSFs, but now only the expansion coefficients are determined. This is done by diagonalizing the Hamiltonian matrix. In the RCI calculations the transverse photon interaction

$$\hat{H}_{\text{Breit}} = -\sum_{i<j}^{M}\left[\boldsymbol{\alpha}_i\cdot\boldsymbol{\alpha}_j\frac{\cos(\omega_{ij}r_{ij}/c)}{r_{ij}} + (\boldsymbol{\alpha}_i\cdot\boldsymbol{\nabla}_i)(\boldsymbol{\alpha}_j\cdot\boldsymbol{\nabla}_j)\frac{\cos(\omega_{ij}r_{ij}/c)-1}{\omega_{ij}^2 r_{ij}/c^2}\right] \tag{2.2.7}$$

may be included in the Hamiltonian. The photon frequency ω_{ij} used by the RCI program in calculating the matrix elements of the transverse photon interaction is taken to be the difference between the diagonal Lagrange multipliers ε_i and

ε_j associated with the orbitals. In general, diagonal Lagrange multipliers are approximate electron removal energies only when orbitals are spectroscopic and singly occupied. Thus it is not known how well the multiconfiguration Dirac-Fock method can determine the full transverse photon interaction when correlation orbitals are present. Frequently, only the low frequency limit $\omega_{ij} \longrightarrow 0$, referred to as the Breit interaction, is used.

2.2.3 Computation of transition parameters

The transition parameters, such as rates (probabilities) for spontaneous decay, for multipole transitions between two atomic states $\gamma J M_J$ and $\gamma' J' M'_J$ can be expressed in terms of reduced transition matrix elements

$$\left\langle \gamma J \| \hat{\mathbf{Q}}_k^{(\lambda)} \| \gamma' J' \right\rangle, \tag{2.2.8}$$

where $\hat{\mathbf{Q}}_k^{(\lambda)}$ is the electromagnetic multipole operator of order k in Coulomb or Babushkin gauge [45]. The superscript designates the type of multipole: $\lambda = 1$ for electric multipoles and $\lambda = 0$ for magnetic multipoles. Standard Racah algebra assumes that the atomic state functions are built from the same orthogonal radial orbital set [46]. However, this restriction can be relaxed. To compute transition matrix elements between two atomic state functions described by independently optimised orbital sets, transformations of the atomic state functions are performed in such a way that the orbital sets become biorthogonal, in which case the calculation can be handled using standard techniques [47]. For electric dipole (E1) and electric quadrupole (E2) transitions there are two forms of the transition operator, the length (Babushkin) form and the velocity (Coulomb) form. The length form is more sensitive to the outer parts of the wave functions and it usually is the preferred form.

The differences between the transition parameters evaluated with the two forms can be used as an indicator of the uncertainty [30]. The quantity δT, characterizing the uncertainty of the computed transition rates, is defined as

$$\delta T = \frac{|A_l - A_v|}{\max(A_l, A_v)}, \quad \delta T = \frac{|S_l - S_v|}{\max(S_l, S_v)}, \tag{2.2.9}$$

where A_l and A_v are transitions rates, S_l and S_v - line strengths in length and velocity form, respectively.

2.2.4 Hyperfine interaction

The hyperfine structure of atomic energy level is the result of the interaction between the electrons and the electromagnetic multipole moments of nucleus. The Hamiltonian of this interaction can be expressed as a multipole expansion [48]:

$$\hat{H}_{hfs} = \sum_{k\geq 1} \hat{\mathbf{T}}^{(k)} \cdot \hat{\mathbf{M}}^{(k)}, \tag{2.2.10}$$

where $\hat{\mathbf{T}}^{(k)}$ and $\hat{\mathbf{M}}^{(k)}$ are spherical tensor operators of rank k in the electronic and nuclear spaces, respectively. The $k = 1$ represents the magnetic dipole interaction and the $k = 2$ – electric quadrupole. Below are presented the magnetic dipole tensor operator in the electronic space for M-electron atom (in a.u.):

$$\hat{\mathbf{T}}^{(1)} = \sum_{j=1}^{M} \hat{\mathbf{t}}^{(1)}(j) = -i\alpha \left(\boldsymbol{\alpha}_j \cdot \mathbf{l}_j \mathbf{C}^{(1)}(j) \right) r_j^{-2}, \tag{2.2.11}$$

and the electric quadrupole tensor operator:

$$\hat{\mathbf{T}}^{(2)} = \sum_{j=1}^{M} \hat{\mathbf{t}}^{(2)}(j) = \mathbf{C}^{(2)}(j) r_j^{-3}. \tag{2.2.12}$$

Here α is the fine structure constant, $\mathbf{l}$ is orbital angular momentum, $\mathbf{C}^{(k)}$ is the spherical tensor related to the spherical harmonic as:

$$\mathbf{C}_q^{(k)} = \sqrt{\frac{4\pi}{2k+1}} Y_{kq}. \tag{2.2.13}$$

In the presence of hyperfine interaction the coupled wave function of the total system of the electrons and the nucleus can be written as:

$$\Psi(\gamma\nu PJIFM_F) = \sum_{M_J M_I} \langle JIM_J M_I | JIFM_F \rangle \; \Psi(\gamma PJM_J) \; \Psi(\nu IM_I), \tag{2.2.14}$$

where the expansion coefficients are the Clebsch-Gordan coefficients. The wave function $\Psi(\nu IM_I)$ corresponds to the state of the nucleus. More details can be found in [48].

The nuclear tensor operators are related to the usual nuclear magnetic dipole moment μ_I and electric quadrupole moment Q_I through relations:

$$\mu_I = \left\langle \Psi(\nu I M_I) | \hat{\mathbf{M}}_0^{(1)} | \Psi(\nu I M_I) \right\rangle, \tag{2.2.15}$$

$$Q_I = 2\left\langle \Psi(\nu I M_I) | \hat{\mathbf{M}}_0^{(2)} | \Psi(\nu I M_I) \right\rangle, \tag{2.2.16}$$

where $M_I = I$. The hyperfine interaction couples the nuclear I and electronic J angular momenta into the total momentum $F = I + J$. The diagonal and off-diagonal matrix elements of the magnetic dipole and electric quadrupole terms of the hyperfine interaction are expressed as:

$$W_{M1} = \left\langle \Psi(\gamma\nu PJIFM_F) | \hat{\mathbf{T}}^{(1)} \cdot \hat{\mathbf{M}}^{(1)} | \Psi\left(\gamma\nu PJ'IFM_F\right) \right\rangle, \quad J' = J, J-1, \tag{2.2.17}$$

$$W_{E2} = \left\langle \Psi(\gamma\nu PJIFM_F) | \hat{\mathbf{T}}^{(2)} \cdot \hat{\mathbf{M}}^{(2)} | \Psi\left(\gamma\nu PJ'IFM_F\right) \right\rangle. \quad J' = J, J-1, J-2. \tag{2.2.18}$$

Usually, the interaction energies are expressed in terms of the hyperfine interaction factors A and B:

$$\begin{aligned}
A_J &= \frac{\mu_I}{I} \frac{1}{[J(J+1)]^{1/2}} \left\langle \Psi(\gamma PJM_J) | \hat{\mathbf{T}}^{(1)} | \Psi(\gamma PJM_J) \right\rangle, \\
A_{J,J-1} &= \frac{\mu_I}{I} \frac{1}{[J(2J-1)]^{1/2}} \left\langle \Psi(\gamma PJM_J) | \hat{\mathbf{T}}^{(1)} | \Psi\left(\gamma P(J-1)M_{(J-1)}\right) \right\rangle, \\
B_J &= 2Q_I \left[\frac{J(2J-1)}{(J+1)(2J+3)}\right]^{1/2} \left\langle \Psi(\gamma PJM_J) | \hat{\mathbf{T}}^{(2)} | \Psi(\gamma PJM_J) \right\rangle, \\
B_{J,J-1} &= \frac{Q_I}{2} \left[\frac{J(J-1)}{(J+1)(2J-1)}\right]^{1/2} \left\langle \Psi(\gamma PJM_J) | \hat{\mathbf{T}}^{(2)} | \Psi\left(\gamma P(J-1)M_{(J-1)}\right) \right\rangle, \\
B_{J,J-2} &= \frac{Q_I}{4} \left[\frac{J(J-1)(2J-1)}{(2J-3)}\right]^{1/2} \left\langle \Psi(\gamma PJM_J) | \hat{\mathbf{T}}^{(2)} | \Psi\left(\gamma P(J-2)M_{(J-2)}\right) \right\rangle.
\end{aligned} \tag{2.2.19}$$

2.2.5 Biorthogonal transformation of atomic state functions

Calculation of several properties (e.g. transitions probabilities, electric dipole moments) a basis build from orthogonal orbitals is necessary. For this reason biorthogonal transformation is implemented in the GRASP2K package (program `biotra2` [47, 49]). Applying linear transformation, this program convert two

nonorthogonal orbital bases $\{\phi_i^L\}$ and $\{\phi_j^R\}$

$$\left\langle \phi_i^L | \phi_j^R \right\rangle = S_{ij}^{LR}, \tag{2.2.20}$$

(where S_{ij}^{LR} is the overlap matrix [47]) into new orbital sets:

$$\phi^A = \phi^L \mathbf{C}^{LA}; \quad \phi^B = \phi^R \mathbf{C}^{RB}, \tag{2.2.21}$$

which are biorthonormal:

$$\left\langle \phi_i^A | \phi_j^B \right\rangle = \delta_{ij}. \tag{2.2.22}$$

This transformation allows to use standard Racah algebra in evaluation of various atomic properties, including EDM.

2.3 Extension of MCDHF method for P- and P,T-odd interactions [C1, C2]

2.3.1 Transitions induced by parity mixing interactions

The rate of the spontaneous one-photon electric dipole (E1) transition between two atomic states with mixed parity is given by (in a. u.) [50, 51]:

$$A \;=\; \frac{4\omega^3}{3c^3} \sum_{M_F,q} \left| \left\langle \widetilde{\Psi}(\gamma \nu I F M_F) \,|\hat{Q}_q^1|\widetilde{\Psi}(\gamma' \nu I F' M_F') \right\rangle \right|^2, \tag{2.3.1}$$

where $\hat{Q}^1$ is the operator of the electric dipole transition.

In the presence of hyperfine interaction the coupled wave function of the total system of the electrons and the nucleus is written as expression (2.2.14): Taking the off-diagonal part of the hyperfine interaction into account the total wave function of an atom can be expressed as:

$$\Psi(\gamma \nu P I F M_F) \;=\; a_0 \Psi(\gamma \nu P J I F M_F) + \sum_{l=1}^{n} a_l \, \Psi(\alpha_l \nu P J_l I F M_F). \tag{2.3.2}$$

The off-diagonal hyperfine interaction is quite weak and the coefficient a_0 of the dominant function can be set to 1 and the expansion coefficients can be perturbatively approximated as:

$$a_l \;=\; \frac{\left\langle \Psi\left(\alpha_l \nu P J_l I F M_F\right) \left| \hat{H}_{hfs} \right| \Psi\left(\gamma \nu P J I F M_F\right) \right\rangle}{E\left(\gamma P J\right) \;-\; E\left(\alpha_l P J_l\right)}, \tag{2.3.3}$$

where $\hat{H}_{hfs}$ is the hyperfine interaction operator [48]. In the analysis of the weak interaction only the nuclear magnetic dipole hyperfine interaction was considered.

Substituting eq. (2.3.2) and eq. (2.1.9) into expression (2.3.1) and summing over the projections of the angular momenta one obtains:

$$\begin{aligned} A \;=\; & \frac{4\omega^3}{3c^3} \frac{1}{2F'+1} \\ & \times \left| \sum_{l,r,l',r'} \; a_l^* a_l' b_r^* b_{r'} \left\langle \Psi\left(\gamma_{lr} \nu P_r J_l I F\right) || \hat{Q}^1 || \Psi\left(\gamma_{l'r'} \nu P_{r'} J_{l'} I F'\right) \right\rangle \right|^2 . \end{aligned} \tag{2.3.4}$$

The perturbative formalism (2.3.3) does not include the radiation-damping effects, which are important when radiative line width is comparable to the separation between fine structure levels [52].

The reduced matrix (submatrix) element of the electric dipole transition operator can be expressed as:

$$\begin{aligned} & \left\langle \Psi\left(\gamma_{lr} \nu P_r J_l I F\right) || \hat{Q}^1 || \Psi\left(\gamma_{l'r'} \nu P_{r'} J_{l'} I F'\right) \right\rangle = \\ & \qquad (-1)^{I+J_l+F'+1} \; \delta(P_r, -P_{r'}) \; \sqrt{(2F+1)(2F'+1)} \\ & \qquad \times \left\{ \begin{array}{ccc} J & F & I \\ F' & J_{l'} & 1 \end{array} \right\} \left\langle \Psi\left(\gamma_{lr} P_r J_l\right) \| \hat{Q}^1 \| \Psi\left(\gamma_{l'r'} (-P_r) J_{l'}\right) \right\rangle . \end{aligned} \tag{2.3.5}$$

The square of the reduced matrix element on the right hand side of the equation 2.3.5 is the line strength.

2.3.2 P,T-odd interactions and permanent electric dipole moment of an atom

This section of the work is based on the review by Ginges and Flambaum [19]. We present here only the expressions for the four P,T-odd operators and the corresponding matrix elements necessary for the discussion of the results. The reader is referred to the review [19] for full explanation, and to the paper [37] for the explicit form of the matrix elements (the only difference is the prefactor $1/r$,

which is absorbed in the definition of radial wave functions).

The interactions which mix atomic states of different parities and induce a static electric dipole moment of an atom are quite weak. Therefore an ASF of a mixed parity state can be expressed as in 2.1.9. The expansion coefficients of opposite parity ($-P$) admixtures, b_i can be found in 2.1.10.

$\hat{H}_{int}$ represents the Hamiltonian of the P,T-odd interaction, which mixes states of opposite parities. The mixed-parity state of a particular atomic level $^{2S+1}L_J$ induces a static EDM of an atom:

$$d_{at}^{int} = \left\langle \widetilde{\Psi}(\gamma JM_J)\,|\hat{D}_z|\widetilde{\Psi}(\gamma JM_J)\right\rangle \;=$$
$$2\sum_i b_i \left\langle \Psi(\gamma PJM_J)\,|\hat{D}_z|\Psi(\gamma_i(-P)J_iM_{J_i})\right\rangle, \tag{2.3.6}$$

where $\hat{D}_z$ represents the z projection of the electric-dipole moment operator. Eventually an EDM of atoms can be written as a sum:

$$d_{at}^{int} =$$
$$2\sum_i \frac{\left\langle \Psi(\gamma PJM_J)\,|\hat{D}_z|\Psi(\gamma_i(-P)J_iM_{J_i})\right\rangle \left\langle \Psi(\gamma_i(-P)J_iM_{J_i})\,|\hat{H}_{int}|\Psi(\gamma PJM_J)\right\rangle}{E_{\gamma PJM_J} - E_{\gamma_i(-P)J_iM_{J_i}}},$$
$$J_i = J \pm 1. \tag{2.3.7}$$

For group 12 elements (Zn, Cd, Hg, Cn), analysed in this work, equation (2.3.7) can be simplified to:

$$d_{at}^{int} = 2\sum_i \frac{\left\langle 0|\hat{D}_z|i\right\rangle \left\langle i|\hat{H}_{int}|0\right\rangle}{E_0 - E_i}, \tag{2.3.8}$$

where $|0\rangle$ represents the ground state $|\Psi(\gamma PJM_J)\rangle$, with $J=0$ and even parity, and the summation runs over excited states $|\Psi(\gamma_i(-P)J_iM_{J_i})\rangle$, with $J_i=1$ and odd parity. E_0 and E_i are energies of ground and excited states, respectively. In practice this sum needs to be truncated at some state.

Calculations of an atomic EDM require evaluation of both matrix elements, $\left\langle 0|\hat{D}_z|i\right\rangle$ and $\left\langle i|\hat{H}_{int}|0\right\rangle$, in the numerator of the equation (2.3.8). The operators associated with the above matrix elements are all one-particle operators.

We consider the following four mechanisms which may induce atomic EDM: tensor-pseudotensor ($\hat{H}_{TPT}$), pseudoscalar-scalar ($\hat{H}_{PSS}$), Schiff moment ($\hat{H}_{SM}$),

and electron EDM interaction with the nuclear magnetic field ($\hat{H}_B$). The interactions, which are all of rank $k = 1$, are discussed in more detail in the next sections. In addition the expression for the electric dipole interaction is given.

2.3.3 Electric dipole operator

The electric-dipole moment operator has the rank $k = 1$ in (2.1.11), (2.1.13), and (2.1.14), and the single-particle reduced matrix element $\left[n_a\kappa_a\|\hat{t}^k\|n_b\kappa_b\right]$ in equation (2.1.14) can be written as

$$\left[n_a\kappa_a\|\hat{d}^1\|n_b\kappa_b\right] = -\left[\kappa_a\|C^1\|\kappa_b\right] \int_0^\infty (P_aP_b + Q_aQ_b)\, r\, dr. \tag{2.3.9}$$

The single-particle angular reduced matrix elements can be expressed as:

$$\left[\kappa_a\|C^k\|\kappa_b\right] = (-1)^{j_a+1/2}\sqrt{2j_b+1}\begin{pmatrix} j_a & k & j_b \\ 1/2 & 0 & -1/2 \end{pmatrix}\pi(l_a,l_b,k), \tag{2.3.10}$$

where $\pi(l_a,l_b,k)$ is defined as:

$$\pi(l_a,l_b,k) = \begin{cases} 1; & \text{if } l_a+k+l_b \text{ even,} \\ 0; & \text{otherwise.} \end{cases} \tag{2.3.11}$$

2.3.4 Electron electric dipole moment

Electron electric dipole moment (d_e) may contribute to the atomic EDM (d_{at}^{eEDM}) in different ways. First case is projection of d_e along the total angular momentum of an atom. In the second case the electron EDM interacts with electric and magnetic fields of the atom [53]. In this section we analyse the operator for the electron EDM interaction with the magnetic field of a nucleus [37]:

$$\hat{H}_B = -id_e\sum_{j=1}^{M}(\boldsymbol{\gamma}_j\,\boldsymbol{B}), \tag{2.3.12}$$

where d_e represents the electron electric dipole moment, and $\boldsymbol{B}$ the magnetic field of the nucleus.

The single-particle reduced matrix element $\left[n_a\kappa_a\|\hat{t}^k\|n_b\kappa_b\right]$ in expansion (2.1.14) for operator of electron EDM interaction with magnetic field of a nucleus can be factorized into reduced angular matrix element and radial integral [37]:

$$\left[n_a\kappa_a\|\hat{h}_B^{el}\|n_b\kappa_b\right] \;=$$

$$\frac{d_e\mu}{2m_pc}\left\{-3\left[-\kappa_a\|C^1\|-\kappa_b\right]\int_R^\infty\frac{Q_aP_b}{r^3}\,dr\;-\;3\left[\kappa_a\|C^1\|\kappa_b\right]\int_R^\infty\frac{P_aQ_b}{r^3}\,dr\right.$$

$$-\;\left[-\kappa_a\|\sigma^1\|\kappa_b\right]\int_R^\infty\frac{Q_aP_b}{r^3}\,dr-\;\left[\kappa_a\|\sigma^1\|-\kappa_b\right]\int_R^\infty\frac{P_aQ_b}{r^3}\,dr$$

$$\left.+\,2\left[-\kappa_a\|\sigma^1\|\kappa_b\right]\int_0^R\frac{Q_aP_b}{R^3}\,dr\;+2\left[\kappa_a\|\sigma^1\|-\kappa_b\right]\int_0^R\frac{P_aQ_b}{R^3}\,dr\right\}, \quad (2.3.13)$$

where R and μ represent the nuclear radius and nuclear magnetic moment, respectively.

2.3.5 Schiff moment

Schiff moment is a nuclear electric dipole moment, generated by intrinsic electric dipole moments of valence nucleons, or by CP-odd interactions between nucleons [54]. The interaction with Schiff moment would lead to rearrangement of the electronic cloud and consequently would induce an atomic EDM [55]. The Hamiltonian of this interaction can be expressed as [19, 56]:

$$\hat{H}_{SM} \;=\; \frac{3}{B}\sum_{j=1}^{M}\left(\boldsymbol{S}\cdot\boldsymbol{r}_j\right)\,\rho\left(r_j\right). \quad (2.3.14)$$

The Schiff moment $\boldsymbol{S}$ is directed along the nuclear spin $\boldsymbol{I}$ and $\boldsymbol{S}\equiv S\boldsymbol{I}/I$, with S being the coupling constant, and $B=\int_0^\infty\rho(r)r^4dr$.

The single-particle reduced matrix element $\left[n_a\kappa_a\|\hat{t}^k\|n_b\kappa_b\right]$ in expansion (2.1.14) for the Schiff moment can be factorized into reduced angular matrix element and radial integral [37]

$$\left[n_a\kappa_a\|\hat{h}^1_{SM}\|n_b\kappa_b\right]=\frac{3}{B}\,S\,\left[n_a\kappa_a\|\hat{r}^1\,\rho\left(r\right)\|n_b\kappa_b\right]=$$

$$\frac{3}{B}\,S\,\left[\kappa_a\|C^1\|\kappa_b\right]\int_0^\infty\!\!\left(P_aP_b\,+\,Q_aQ_b\right)\,\rho\left(r\right)r\,dr\,. \quad (2.3.15)$$

2.3.6 Summary

Matrix elements of interaction: P-odd vector-axial and of P,T-odd tensor-pseudotensor and pseudoscalar-scalar electron-nucleon are presented in subsections 2.1.1, 2.1.2, and 2.1.3, respectively. Factorized and reduced angular matrix element and radial integrals of these interactions are presented in equations (2.1.15, 2.1.19, 2.1.21, 2.1.20 and 2.1.25). Also nuclear Schiff moment interaction with electrons and electron electric dipole moment interaction with nuclear magnetic field, was presented in subsection 2.3.5 and 2.3.4, respectively, and factorized matrix element are given in equations (2.3.15 and 2.3.13).

2.4 Code development

We extended the GRASP2K [43] package for calculations of single-particle reduced matrix elements (2.3.9), (2.1.19), (2.1.25), (2.3.15), and (2.3.13). The extension, presented in this work, includes subroutines for calculations of matrix elements of type $\langle i|\hat{H}_{int}|0\rangle$ in equation (2.3.8) for tensor-pseudotensor $\hat{H}_{TPT}$, pseudoscalar-scalar $\hat{H}_{PSS}$, Schiff moment $\hat{H}_{SM}$, electron EDM interaction with nuclear magnetic field $\hat{H}_B$, and electric dipole moment $\hat{D}_z$.

Figure 2.4.1 describes program flow in EDM computation procedure. Section from `iso` to `biotra2` is well known and more detailed description can be found in [43]. Computation of ASF can be performed in orthogonal or nonorthogonal approach. Wave functions for ground and excited states (even and odd states) in orthogonal computation are generated simultaneously and biorthogonal transformation is not necessary. On the other hand, for nonorthogonal ASFs the biorthogonal transformation procedure must be applied. The program `biotra` from GRASP2K package [43] is used for this procedure. In figure 2.4.1 double arrows show the flow of files for that section of the calculation, when the ground and excited states are generated separately.

The program `biotraEDM2015` for computations of matrix elements can only be used, when ASFs are either orthogonal or biorthogonal. Matrix elements for each operator – D_z, TPT, PSS, SM, and eEDM — are obtained in separate calculations.

Output files from program `biotraEDM2015`, called `name1.name2.*` (see figure 2.4.1), contain information about: isotope; radial grid; initial and final subshell radial wave function summary; eigenenergies; mixing coefficients; and ma-

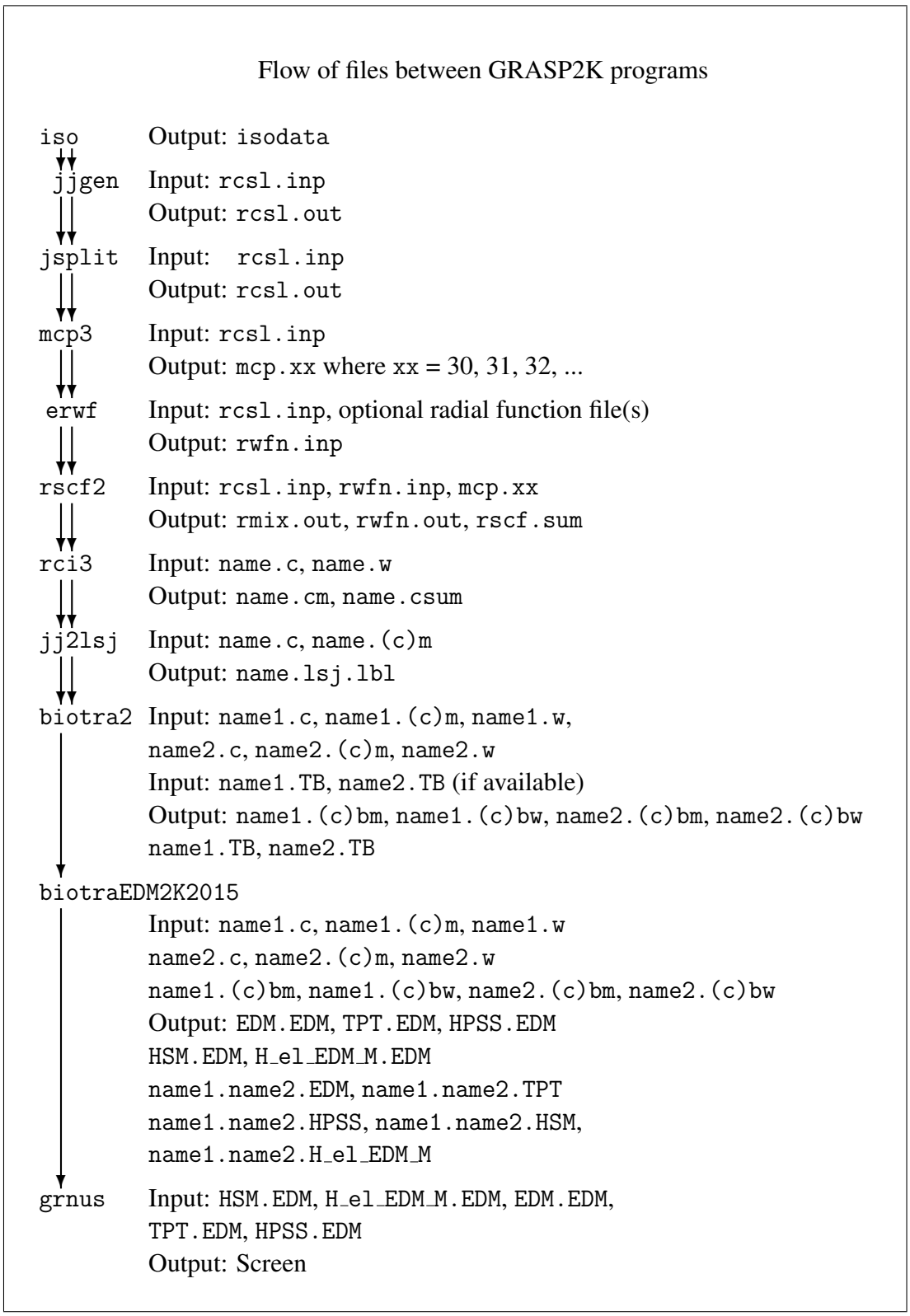

Figure 2.4.1: Flow of files for a normal sequence of program runs.

trix elements. For example, file called `name1.name2.TPT` contains information about TPT interaction matrix elements.

Files with suffix `.EDM` contain total energies of ground state and excited states, as well as matrix elements (in a.u.). The first section of the file name identifies the interaction for which the matrix elements were recorded. For example, the file `TPT.EDM` contains records about matrix element of the TPT interaction. These files contain also an empty column called "Exp. Energy", in which the experimental energy (in a.u.) may be manually written. In the column "A" matrix elements (in a.u.) are written. As an example, a part of the file `TPT.EDM` from a calculation for Hg (with 4 layers of virtual orbitals) is presented below:

```
E0 Levels  J Parity  Energy              A                   Exp. Energy
    1      0   +      -0.1964930249D+05
Ek Levels  J Parity  Energy              A                   Exp. Energy
    1      1   -      -0.1964909603D+05    0.3816654259D+02
    2      1   -      -0.1964902949D+05    0.1990148145D+02
    3      1   -      -0.1964867511D+05    0.1409045570D+02
    4      1   -      -0.1964866549D+05    0.2551936923D+02
```

In the last step program `grnus` performs computation of atomic EDM, according to the equation (2.3.8). The program `grnus` must be launched separately for each EDM inducing mechanism. Program requires two input files: one with D_z matrix elements and another with matrix elements of EDM interaction. The output from `grnus` program for Hg (with 4 layers of virtual orbitals) is presented below:

```
 The name of a input file
 The name of b input file
Tensor-pseudotensor in units (C_T <\sigma_N>|e|cm)
EDM4                file completed
TPT_new_2           file completed
   Theoretical value Experimental value  Theo cont        Exp cont   Theo cont%  Exp cont %
 1 -0.1539347712D-19                    -0.1539347712D-19              31.78824%
 2 -0.4650789420D-19                    -0.3111441709D-19              64.25270%
 3 -0.4719932672D-19                    -0.6914325187D-21               1.42784%
 4 -0.4405852722D-19                     0.3140799497D-20              -6.48590%
...
```

Chapter 3

Results of calculations of atomic properties for N- and Si-like isoelectronic sequences [A1, A2]

Spectroscopic data for the nitrogen isoelectronic sequence are of importance in astrophysics. N-like ions emit several lines that are used for diagnosing the physical conditions of the solar chromosphere, transition region, and corona in the Solar Ultraviolet Measurement of Emitted Radiation (SUMER) spectrograph on the SOHO spacecraft [57, 58]. Moreover, the X-ray telescopes on board the space observatories *Chandra* and *XMM-Newton* provide high-resolution spectra that are rich in emission and absorption lines from various iron ions, including Fe XX [59]-[61].

Data for nitrogen-like ions are also of importance in fusion science. The XEUS (X-ray and Extreme Ultraviolet Spectrometer) and LoWEUS (Long - Wavelength and Extreme Ultraviolet Spectrometer), which operate in the 5-400 Å region, were used to find impurities, both for intrinsic elements present in the plasma and for metal impurities resulting from damage of various components in NSTX (National Spherical Tokamak Experiment). The most commonly seen metal impurity is iron, followed by copper, and nickel. Iron, nickel and chromium are used in NSTX as the makeup of stainless steel, of which the outer wall, a number of hardware components, shielding of magnetic sensors, as well as cables are made. Identification of metal impurities provides information about components which are affected, and to what degree [62]. These spectrometers provide information about plasma conditions, but the identification of spectra lines is problematic without experimental or theoretical data. For reasons listed above large scale computation were done for Cr XVIII, Fe XX, Ni XXII, Zn XXIV ions.

Transition probabilities (A), wavelengths (λ), weighted oscillator strengths (gf) of electric dipole (E1), electric quadrupole (E2), and magnetic dipole (M1) transitions, as well as lifetimes of levels in length and velocity forms ($\tau_{l,v}$) were

computed for a large part of the energy spectrum (for 272 levels).

Nuclear parameters (hyperfine structure: magnetic dipole (A) and electric quadrupole constants (B), Landé g_J-factors; isotope shifts: the normal and specific mass shifts ($\widetilde{K}_{NMS}, \widetilde{K}_{SMS}$), and the field shifts ($\widetilde{\mathscr{F}}$) are also computed for these levels. All results are available at Strasbourg Astronomical Data Center (CDS) `http://cdsarc.u-strasbg.fr/viz-bin/qcat?J/A+A/582/A61`. Do to the sizes of the files, only Fe XX data are presented.

The emission spectrum of Si-like Fe (Fe XIII) in the extreme ultraviolet (EUV) range provides important lines for electron density diagnostics of the solar and stellar coronal plasma [63]. These lines have been observed using the EUV Imaging Spectrometer (EIS) on board the Hinode satellite, the Coronal Diagnostic Spectrometer (CDS) on board the SOHO satellite, and by the Solar EUV Rocket Telescope and Spectrograph (SERTS), see for example [64]. Much work has been devoted to benchmark and validate atomic data for Fe XIII against high-resolution spectroscopic observations of the solar corona [65], and against well defined laboratory plasmas [66, 67]. Also, lines from Ni XV can be used for electron density diagnostics in high-temperature (3 MK) plasmas, such as those of solar active region cores, as discussed in [68]. Authors of paper [69] provided a complete set of rates and a list of the strongest lines that are observable in astrophysical plasmas, and previous identifications were revised.

3.1 Atomic state function expansions for N- and Si-like isoelectronic sequences

The configuration expansions were obtained using the active set (AS) method [70]. Here CSFs of a specified parity and J symmetry are generated by substitutions from a number of reference configurations (a so called multireference set – MR) to a set of virtual relativistic orbitals. By applying restrictions on the allowed substitutions, different electron correlation effects can be targeted. For energies and transition rates, valence and core-valence correlation effects are by far the most important. To monitor the convergence of the calculated energies and transition parameters, the active sets were increased in a systematic way by adding layers of orbitals. Only CSFs interacting with the MR set were retained in CSF expansions. Separate self-consistent field calculations were performed for even and odd states in the EOL form (see section 2.2.1).

Table 3.1.1: Configuration expansions for N-like and Si-like ions.

	n and l	MR set
N-like	$n = 3 \ldots 8$	$\{2s^2 2p^3, 2p^5, 2s^2 2p^2 3p, 2s2p^3 3s. 2s2p^3 3d, 2p^4 3p\}$ for odd states
	$l = 0 \ldots 5$	$\{2s2p^4, 2s^2 2p^2 3s, 2s^2 2p^2 3d, 2s2p^3 3p, 2p^4 3s, 2p^4 3d\}$ for even states
	$n = 3 \ldots 9$	for Fe XX
the $1s^2$ core was closed for substitutions at the $n = 6$ stage for SCF calculations		
Si-like	$n = 3 \ldots 7$	$\{3s3p^3, 3s^2 3p3d, 3s3p3d^2, 3p^3 3d, 3p3d^3\}$ for odd states
	$l = 0 \ldots 6$	$\{3s^2 3p^2, 3s^2 3d^2, 3s3p^2 3d, 3p^2 3d^2, 3p^4\}$ for even states
the $1s^2$ core was closed for substitutions at the $n = 6$ stage for SCF and RCI calculations		

The configuration expansions were obtained by single and double (SD) substitutions from all shells of the MR set configurations to active sets (with principal (n) and orbital (l) quantum numbers listed in Table 3.1.1). For the nitrogen isoelectronic sequence the SD substitutions were forbidden from $1s$ shell at $n = 6$ for SCF calculations. For the $n = 8$ expansion this approach resulted in 1 076 078 (6 206 696) CSFs with odd parity and 916 973 (5 255 680) CSFs with even parity with the $1s^2$ core closed (open). For silicon-like ions the $1s^2$ core was closed for substitutions at the $n = 6$ stage for SCF and RCI calculations. Final expansions (N_{CSF}) for the states of even and odd configurations distributed over the J symmetry blocks for each isoelectronic sequence are provided in Table 3.1.2. The self-consistent field calculations for each layer of orbitals were followed by RCI calculations, including the Breit interaction and the leading QED effects (vacuum polarization and self-energy).

Table 3.1.2: Summary of the extended optimal level MCDHF calculations, listing the ranges of eigenvalues and the sizes of the interaction matrices for each configuration.

Configurations	J	P	Number of states	N_{CSF}
N-like				
$2s^2 2p^3, 2p^5, 2s^2 2p^2 3p, 2s2p^3 3s, 2s2p^3 3d, 2p^4 3p$	1/2-11/2	–	140	1 076 078
$2s2p^4, 2s^2 2p^2 3s, 2s^2 2p^2 3d, 2s2p^3 3p, 2p^4 3s, 2p^4 3d$	1/2-9/2	+	132	916 973
Si-like				
$3s3p^3, 3s^2 3p3d$	0-4	–	22	1 500 000
$3s^2 3p^2$	0-2	+	5	4 600 000

3.2 N-like ions

Due to their importance, N-like ions have been studied using a number of different theoretical methods. Vilkas & Ishikawa have made calculations of energy levels and transition probabilities for a number of ions in the sequence [71], in the framework of relativistic multireference Møller-Plesset perturbation theory (MRMP). Merkelis *et al.* used second-order many-body perturbation theory (MBPT) with relativistic corrections in the Breit-Pauli approximation to compute oscillator strengths between the levels of the $2s^2 2p^3$, $2s2p^4$, and $2p^5$ configurations [72], and between the levels of the $2s^2 2p^3$ configuration [73]. Ions in the range $Z = 10, \ldots, 30$ were covered. Kotochigova *et al.* evaluated the wavelengths and oscillator strengths for the $2s^2 2p^2 3s,\ 3d \rightarrow 2s^2 2p^3$, and $2s2p^3 3p \rightarrow 2s^2 2p^3$ transitions in Fe XX, using a configuration interaction Dirac-Fock-Sturm (MDFS) method combined with second-order Brillouin-Wigner perturbation theory [74]. Bhatia *et al.* determined transition parameters between $n = 2$ and $n = 3$ levels of Ar XII, Ti XVI, Fe XX, Zn XXIV, and Kr XXX, using the SUPERSTRUCTURE (SS) code [75]. Within the Iron Project, Nahar used the Breit-Pauli R-matrix (BPRM) method and the SUPERSTRUCTURE code to derive an extensive set of oscillator strengths, line strengths, and radiative decay rates for transitions in Fe XX [76]. Jonauskas *et al.* took a broad approach and performed multiconfiguration Dirac-Hartree-Fock (MCDHF) and configuration interaction calculations on the basis of transformed radial orbitals (CITRO) with variable parameters including relativistic effects in the Breit-Pauli approximation to derive energies of 700 lowest levels in Fe XX, and corresponding transition parameters [77]. A combined configuration interaction and relativistic many-body perturbation theory (RMBPT) approach was used by Gu to obtain energies in iron and nickel ions with high accuracy [78]. Rynkun *et al.* used relativistic configuration interaction (RCI) approach to compute energies, transition rates, and lifetimes of $n = 2$ levels for all N-like ions with Z = 9, ..., 36 [79].

The aim of the present work is to provide highly accurate spectroscopic data for four ions in the N-like isoelectronic sequence that are important for plasma diagnostics. Compared with the recent work [79] the calculations are extended to include additional 257 levels of the $2s^2 2p^2 3l$, $2s2p^3 3l$, and $2p^4 3l$ ($l = 0, 1, 2$) configurations. The calculations also extend the work [78] to include levels of the Cr XVIII and Zn XXIV ions.

3.2.1 Energy levels and transition data results for N-like ions

Table 3.2.1: Energy levels (cm^{-1}) for the 15 lowest states of Fe XX as a function of the highest principal quantum number n of the active set of orbitals. E_{NIST} are NIST recommended values.

No	*LSJ*	MR	$n=3$	$n=4$	$n=5$	$n=6$	$n=7$	$n=8$	$n=9$	E_{NIST}
					$2s^22p^3$					
1	$^4S^o_{3/2}$	0	0	0	0	0	0	0	0	0
2	$^2D^o_{3/2}$	142 564	142 464	140 512	139 411	138 985	138 854	138 814	138 787	138 620
3	$^2D^o_{5/2}$	180 433	180 363	177 886	176 901	176 496	176 367	176 332	176 308	176 130
4	$^2P^o_{1/2}$	263 718	263 044	263 293	261 487	260 828	260 630	260 573	260 533	260 270
5	$^2P^o_{3/2}$	326 426	326 053	325 739	324 303	323 759	323 592	323 549	323 520	323 340
					$2s2p^4$					
6	$^4P_{5/2}$	756 552	755 964	754 312	752 983	752 667	753 346	752 844	752 725	752 730
7	$^4P_{3/2}$	824 202	823 604	822 144	820 861	820 557	821 237	820 743	820 628	820 630
8	$^4P_{1/2}$	846 426	845 775	844 215	842 795	842 436	843 111	842 610	842 492	842 480
9	$^2D_{3/2}$	1 056 030	1 055 207	1 047 209	1 044 066	1 043 019	1 043 621	1 042 999	1 042 839	1 042 570
10	$^2D_{5/2}$	1 071 189	1 070 330	1 062 812	1 059 765	1 058 759	1 059 363	1 058 748	1 058 590	1 058 360
11	$^2S_{1/2}$	1 210 845	1 209 054	1 201 978	1 197 566	1 196 045	1 196 601	1 195 901	1 195 713	1 195 260
12	$^2P_{3/2}$	1 261 249	1 259 748	1 248 317	1 244 514	1 243 178	1 243 757	1 243 106	1 242 934	1 242 430
13	$^4P_{1/2}$	1 357 678	1 356 013	1 346 103	1 342 158	1 340 774	1 341 346	1 340 689	1 340 516	1 340 040
					$2p^5$					
14	$^2P^o_{3/2}$	1 983 635	1 981 308	1 963 292	1 956 866	1 954 974	1 954 738	1 954 735	1 954 623	1 954 310
15	$^2P^o_{1/2}$	2 090 757	2 088 025	2 070 782	2 064 485	2 062 626	2 062 396	2 062 402	2 062 298	2 061 990

Computed energies of a 15 lowest states are displayed in Table 3.2.1 as functions of the increasing size of active orbital set. The mean relative difference between theory and experimental data from the National Institute of Standards and Technology (NIST) [81] is 1.32%, 1.21%, 0.58%, 0.21%, 0.08%, 0.09%, 0.05%, 0.04% for calculations based on the MR expansion and expansions obtained from SD substitutions to orbital sets with the highest principal quantum numbers $n = 3-9$, respectively. The calculations are well converged with respect to the size orbital set. A general observation is that the quartet states are energetically lower compared to the doublet states. This is due to the fact that electron correlation effects are smaller and converge faster with respect to the orbital set for high spin states, compared with low spin states [82, 83]. The calculations did not quite manage to correctly balance the contributions from quartet and doubled states.

In Table 3.2.2 the current results ($_{Our}$) are compared with results from other calculations. The current results and the results from [79] and [78] stand out in the sense that the mean uncertainties are 0.04%, 0.05% and 0.04%, respectively, compared with NIST. With the exception of the calculation [71], the other calcu-

lations are associated with uncertainties, that are larger by a factor of 10 or more. Energies of all levels of configuration $2s^2 2p^2 3d$ were computed, while the NIST database lists about half of them.

Table 3.2.2: Energy levels (cm^{-1}) and the differences (Diff) between theoretical energies and those from NIST E_{NIST} for Fe XX in N-like isoelectronic sequence. See text for the explanation of the labels.

LSJ	*E*	Diff								
	NIST [81]	*Our*	*RCI* [79]	*MRMP* [71]	*SS* [75]	*BPRM* [76]	*CITRO* [77]	*MBPT* [72]	*CI+MBPT* [78]	*MDFS* [74]
					$2s^2 2p^3$					
$^4S^o_{3/2}$	0	0	0	0	0	0	0	0	0	0
$^2D^o_{3/2}$	138 620	167	198	5	1 978	2 283	236	432	53	262
$^2D^o_{5/2}$	176 130	178	212	5	2 859	5 485	−178	−213	6	258
$^2P^o_{1/2}$	260 270	263	307	1 052	−2 697	4 307	201	−1 323	366	627
$^2P^o_{3/2}$	323 340	180	226	2 703	−3 463	5 214	−972	−3 299	241	567
					$2s2p^4$					
$^4P_{5/2}$	752 730	−5	−60	−224	−5 629	4 677	−2 344	−2 767	420	
$^4P_{3/2}$	820 630	−2	−46	−222	−7 932	3 497	−2 927	−4 303	483	
$^4P_{1/2}$	842 480	12	−27	−164	−8 037	3 704	−3 057	−4 538	466	
$^2D_{3/2}$	1 042 570	269	267	−104	1 707	8 055	−3 326	−4 795	32	
$^2D_{5/2}$	1 058 360	230	227	−188	2 856	9 713	−2 893	−5 396	36	
$^2S_{1/2}$	1 195 260	453	476	3 191	24	9 985	−3 135	−7 329	314	
$^2P_{3/2}$	1 242 430	504	522	6 112	8 974	10 880	−3 222	−8 014	−9	
$^2P_{1/2}$	1 340 040	476	509	−133	5 272	11 265	−3 781	−10 430	2	
					$2p^5$					
$^2P^o_{3/2}$	1 954 310	313	611	1 419		12 380	−5 869	−10 477	−536	
$^2P^o_{1/2}$	2 061 990	308	619	1 476		14 086	−6 348	−13 195	−426	

Selected transition rates are compared with rates from other calculations in Table 3.2.3. There is a detailed agreement with rates from [79], which is expected since the calculations are very similar. There is a good overall agreement between all calculated values. The on-line material contains transition energies, wavelengths, transition rates, weighted oscillator strengths and uncertainty estimators δT for transitions between all 272 states and all four ions Cr XVIII, Fe XX, Ni XXII, and Zn XXIV [A1]. The uncertainty of the transition rates, as estimated by δT in equation (2.2.9), is around 1% for strong allowed transitions. For weak intercombination transitions the uncertainties are often larger. There are a number of weak two-electron one-photon transitions. These transitions are forbidden in the single configuration approximation and become allowed only through electron correlation effects. The two-electron one-photon transitions are known to be very difficult to compute and are associated with large uncertainties.

The lifetimes of the states have been computed from the transition rates.

Table 3.2.3: Comparison of transition rates: E1 transition rates between states of the upper (U) configuration $2s2p^4$ and the lower (L) configuration $2s^22p^3$, E2 transition rates between states of the upper (U) configuration $2p^5$ and the lower (L) configuration $2s^22p^3$, and M1 transition rates between states of $2s^22p^3$ in Fe XX in N-like isoelectronic sequence. Transition rates A are given in s^{-1}. Numbers in the brackets are powers of ten.

U	L	A					
		NIST [81]	*Our*	*RCI* [79]	*MCDF* [77]	*BPRM* [76]	*MBPT* [72, 73]
				E1			
$^2P_{3/2}$	$^2P^o_{3/2}$	9.40[9]^C	9.042[9]	9.038[9]	9.36[9]		9.187[9]
$^2P_{3/2}$	$^2P^o_{1/2}$	9.1[9]^C	8.380[9]	8.380[9]	8.64[9]		8.315[9]
$^2P_{3/2}$	$^2D^o_{5/2}$	1.0[11]^C	9.323[10]	9.321[10]	9.74[10]		9.247[10]
$^2P_{3/2}$	$^2D^o_{3/2}$	1.47[10]^C	1.362[10]	1.362[10]	1.47[10]		1.372[10]
$^2P_{1/2}$	$^2P^o_{3/2}$	9.6[10]^C	8.837[10]	8.835[10]	9.20[10]	8.26[10]	8.769[10]
$^2P_{1/2}$	$^2P^o_{1/2}$	4.4[9]^D	3.676[9]	3.677[9]	4.14[9]		3.720[9]
$^2P_{1/2}$	$^2D^o_{3/2}$	2.91[10]^C	2.648[10]	2.648[10]	2.85[10]		2.614[10]
$^2D_{3/2}$	$^2P^o_{1/2}$	2.98[9]^C	2.670[9]	2.668[9]	2.81[9]		2.661[9]
$^2D_{3/2}$	$^2D^o_{5/2}$	4.3[7]^E	3.056[7]	3.036[7]	4.95[7]		2.539[7]
$^2D_{3/2}$	$^2D^o_{3/2}$	4.3[10]^C	3.850[10]	3.849[10]	3.97[10]		3.825[10]
$^2D_{5/2}$	$^2P^o_{3/2}$	6.0[9]^C	5.419[9]	5.416[9]	5.61[9]		5.500[9]
$^2D_{5/2}$	$^2D^o_{3/2}$	2.7[7]^E	1.448[7]	1.446[7]	1.39[7]	1.09[7]	1.096[7]
$^2D_{5/2}$	$^2D^o_{5/2}$	3.3[10]^C	2.932[10]	2.930[10]	3.04[10]		2.916[10]
$^4P_{1/2}$	$^4S^o_{3/2}$	2.09[10]^C	1.877[10]	1.875[10]	1.92[10]	1.28[10]	1.852[10]
$^4P_{3/2}$	$^4S^o_{3/2}$	1.86[10]^C	1.677[10]	1.676[10]	1.72[10]	1.37[10]	1.667[10]
$^4P_{5/2}$	$^4S^o_{3/2}$	1.3[10]^C	1.187[10]	1.186[10]	1.22[10]	1.19[10]	1.194[10]
$^2D_{5/2}$	$^4S^o_{3/2}$		1.590[7]	1.583[7]	1.40[7]		1.602[7]
$^2D_{3/2}$	$^4S^o_{3/2}$	1.9[9]^E	1.554[9]	1.555[9]	1.52[9]	2.87[9]	1.428[9]
$^2S_{1/2}$	$^4S^o_{3/2}$	1.9[9]^E	1.662[9]	1.663[9]	1.69[9]	1.48[10]	1.539[9]
$^2P_{3/2}$	$^4S^o_{3/2}$	4.6[9]^E	4.079[9]	4.082[9]	4.16[9]	8.75[9]	3.811[9]
$^2P_{1/2}$	$^4S^o_{3/2}$		1.211[8]	1.212[8]	1.32[8]		1.226[8]
				E2			
$^2P^o_{1/2}$	$^2D^o_{3/2}$	5.2^E	5.212	5.297		5.40	4.99
$^2P^o_{3/2}$	$^2D^o_{5/2}$	1.5[1]^E	1.459[1]	1.497[1]		1.54[1]	1.39[1]
$^2P^o_{1/2}$	$^2P^o_{3/2}$	2.2^E	2.066	2.072		2.15	1.87
				M1			
$^2P^o_{1/2}$	$^4S^o_{3/2}$	3.3[4]^D	3.135[4]	3.136[4]	3.13[4]	2.97[4]	2.98[4]
$^2P^o_{3/2}$	$^4S^o_{3/2}$	2.91[4]^C	2.921[4]	2.921[4]	2.98[4]	2.91[4]	2.85[4]
$^2P^o_{1/2}$	$^2D^o_{3/2}$	6.100[3]^D	5.801[3]	5.801[3]	5.87[3]	6.06[3]	5.62[3]
$^2P^o_{3/2}$	$^2D^o_{3/2}$	4.49[4]^D	4.339[4]	4.341[4]	4.28[4]	4.34[4]	4.06[4]

C, D and E are estimated accuracies of NIST database [81] transition probabilities. C: $\leq$25%, D:$\leq$ 50%, E: $\geq$ 50%.

3.2.2 Conclusions

Self-consistent MCDHF and subsequent RCI calculations were performed for the nitrogen-like ions Cr XVIII, Fe XX, Ni XXII, and Zn XXIV, using GRASP2K. Energies, A and B hyperfine constants, Landé g_J-factors, mass- and field shift parameters and transition rates involving the $2s^22p^3$, $2s2p^4$, $2p^5$, $2s^22p^23l$, $2s2p^33l$, and $2p^43l$ ($l = 0, 1, 2$) configurations are provided. Compositions of atomic state functions in LSJ-coupling are also reported. Previous theoretical and experimental data for Fe XX were used to validate computational methods. Energies from the RCI calculations are in excellent agreement with observations. For the 15 lowest states the mean relative energy differences are around 0.04% (comparing with NIST) for the four ions. This translates to wavelengths that are accurate to within ± 10 mÅ and thus of spectroscopic accuracy. The high accuracy carries over also to the higher lying states.

Uncertainties in electric dipole transition rates between the lower states have been estimated from the expressions suggested in paper [80] giving an average of only 1.9%. We thus argue that the transition rates are highly accurate and may serve as benchmark for other calculations. To summarize, the present work has significantly increased the amount of accurate data for ions in the nitrogen-like sequence.

3.3 Si-like ions

The diagnostic value of the EUV lines in Si-like ions relies on accurate atomic data. A large number of theoretical studies have been done for the sequence, as well as for individual ions and here we can only discuss a few of the more recent ones. Froese Fischer *et al.* reported energies, lifetimes, and transition rates for low-lying states in ions up to Fe XIII from multiconfiguration Hartree-Fock calculations with Breit-Pauli relativistic corrections (MCHF-BP), as part of the large compilation of atomic data for ions in the sodium- to argon-like sequences [84]. For the Si-like ions only valence electron correlation was considered. Kohstall *et al.* performed fully relativistic multiconfiguration Dirac-Hartree-Fock (MCDHF) calculations for seven ions in the sequence, providing energies, lifetimes and transition rates [85]. Again, only valence correlation was accounted. Brage and co-workers [86, 87] used both the MCHF-BP and MCDHF methods to study energies and transition rates along the sequence. The effects

of valence- and core-valence electron correlation were analysed with the conclusion that core-valence correlation is important at the low-Z end, but that the effects decrease with Z. For higher Z it is important to use a fully relativistic approach. As part of the comparison of theoretical emission-line-intensity ratios with high-resolution spectra from the SERTS, Keenan *et al.* provided MCDHF energy and transition data involving 301 levels in Fe XIII [63], originally from paper [88]. Storey & Zeippen have performed R-matrix calculation of rate coefficients for electron collisional excitation and oscillator strengths for Fe XIII [89]. Turning to Ni XV, Landi & Bhatia [90] have made FAC (Flexible Atomic Code) calculations of electron impact collision strengths, energy levels, oscillator strengths, and transition rates, while Gupta & Msezane used the CIV3 code to compute excitation energies from the ground state, oscillator strengths, and radiative transition rates [91]. A lot of theoretical data have been provided by Ishikawa & Vilkas using the relativistic multireference many-body perturbation (MR-MP) method. Energies and transition probabilities were presented for various ions in the sequence in a number of publications [92] - [97]. The excitation energies were computed with spectroscopic accuracy and a number of experimental misidentifications could be detected. Also, the calculations allowed new lines to be identified (see for example [98]). On the experimental side Träbert and co-workers have reported lifetimes, as well as spectra for line identification from accelerator based work: [99] - [105].

When computational method and strategy have been validated against observations, computed excitation energies may be used for further line identifications. For transition parameters, such as oscillator strengths and transition rates, the situation is quite different. There are no experimental data for individual transitions; only lifetimes for a few states are available. In addition, lifetime measurements are in many cases associated with large uncertainties resulting in sizable error bars (see for example [102]). Also, transition parameters from calculations are problematic in that they often scatter substantially. Rates for diagnostically important transitions in Fe XIII from different calculations and tabulations are compared as in the paper by Watanabe *et al.* [64]. For some transitions the rates from the quoted studies differ by a factor of 3.

3.3.1 Energy results

In Table 3.3.1 we present the computed energies in Fe XIII for increasing active sets of orbitals labeled by the highest principal quantum number n. For comparison, observed energies from [65] are quoted as well. The relative difference between theory and observation is 1.51%, 0.48%, 0.20%, 0.09% and 0.03% for the calculations based, respectively, on the expansion from the MR, and the expansions from SD substitutions to orbital sets with the highest principal quantum numbers $n = 4-7$. Thus the calculations are well converged with respect to the increasing orbital set. It is obvious that the uncertainties would be further decreased by extending the orbital set. This, however, would result in very large expansions. A general observation is that energy for the $3s3p^3\ ^5S^o_2$ high spin state is too low compared with the $3s^23p^2\ ^3P_0$ ground state. This is due to the fact that electron correlation effects are smaller in states with high spin than in states with lower spin [83, 82], such as the ground state, and there is a slight inbalance in the amount of electron correlation that has been captured in the two states. The energies for the $3s^23p3d\ ^1F^o_3$ and $3s^23p3d\ ^1P^o_3$ states, on the contrary, are too high, but the energies are moving in the right direction when the orbital set is extended.

The computed energies, based on the largest orbital set $n = 7$, are presented in the Table 3.3.2, together with energies from MR-MP calculations [96], and with energies from the NIST database and, for some ions, also from other sources, as noted in the Table. For easy comparison the differences between the computed and observed energies are also given. The agreement between the computed transition energies and the observed ones is excellent. The present calculations and the MR-MP calculations by Ishikawa [96] provide energies of spectroscopic accuracy, i.e. the computed transition wavelengths are so accurate they can be used to identify unknown lines in spectra. In some ions there are levels for which the agreement between theory and observation is less satisfactory, with differences up to a few thousand cm^{-1}. In these cases we have reasons to believe that the observed levels are incorrectly identified and wrongly assigned. For some ions the energies listed in the NIST database are based on experimental extrapolations. In many cases these extrapolations give, as it seems, good values, in agreement with calculations. However, in some cases the extrapolations give energies that differ substantially from calculated energies. We note that the slight inbalance in energies for high- and low spin states for the present calculations

Table 3.3.1: Excitation energies (cm^{-1}) for Fe XIII as a function of the increasing size of the CSF expansion. Expansions are obtained from CSFs that can be generated whit SD substitutions from a MR to an active set labeled by the highest n value of the orbitals in the set. Observed energies are from [65].

Level	MR	$n=4$	$n=5$	$n=6$	$n=7$	E_{obs}
$3s^2\,3p^2\ ^3P_0$	0	0	0	0	0	0
$3s^2\,3p^2\ ^3P_1$	9076	9220	9255	9275	9281	9303
$3s^2\,3p^2\ ^3P_2$	18543	18557	18551	18554	18553	18561
$3s^2\,3p^2\ ^1D_2$	50531	48895	48483	48317	48236	48069
$3s^2\,3p^2\ ^1S_0$	95531	93155	92338	91985	91839	91511
$3s\,3p^3\ ^5S^o_2$	211494	213687	213982	214189	214152	214624
$3s\,3p^3\ ^3D^o_1$	288418	287841	287418	287287	287123	287205
$3s\,3p^3\ ^3D^o_2$	288577	287998	287570	287435	287270	287356
$3s\,3p^3\ ^3D^o_3$	291342	290791	290381	290255	290095	290180
$3s\,3p^3\ ^3P^o_0$	331811	330395	329556	329207	328974	328927
$3s\,3p^3\ ^3P^o_1$	332489	331085	330261	329919	329689	329637
$3s\,3p^3\ ^3P^o_2$	333031	331650	330870	330545	330323	330282
$3s\,3p^3\ ^1D^o_2$	365802	363349	362891	362665	362482	362407
$3s\,3p^3\ ^3S^o_1$	425440	417451	416444	415875	415577	415462
$3s^2\,3p\,3d\ ^3F^o_2$	436053	431815	430817	430476	430277	430124
$3s^2\,3p\,3d\ ^3F^o_3$	442770	438580	437594	437259	437064	436919
$3s\,3p^3\ ^1P^o_1$	449174	440987	439527	438735	438365	438086
$3s^2\,3p\,3d\ ^3F^o_4$	452714	448609	447648	447325	447134	447001
$3s^2\,3p\,3d\ ^3P^o_2$	496799	489144	487534	486848	486542	486358
$3s^2\,3p\,3d\ ^3P^o_1$	504973	497626	496033	495387	495102	494942
$3s^2\,3p\,3d\ ^1D^o_2$	509858	501725	500082	499375	499060	498870
$3s^2\,3p\,3d\ ^3P^o_0$	510705	504078	502558	501949	501676	501514
$3s^2\,3p\,3d\ ^3D^o_1$	517400	509237	507607	506950	506661	506505
$3s^2\,3p\,3d\ ^3D^o_3$	520350	511899	510255	509592	509303	509176
$3s^2\,3p\,3d\ ^3D^o_2$	520606	511974	510342	509684	509394	509250
$3s^2\,3p\,3d\ ^1F^o_3$	571745	562189	559131	557905	557432	556911
$3s^2\,3p\,3d\ ^1P^o_1$	586138	576606	573369	571925	571376	570743

persevere throughout the sequence. A method that better balances the MR, and thus the electron correlation, is thus desirable and would lead to even better energy predictions.

3.3.2 Lifetimes and transition rates

The lifetimes of the excited states were calculated from E1 transition rates in both the length and velocity forms as well as from M1 transition rates. The contributions to the lifetimes from E2 and higher multipoles are negligible. The average relative difference between the lifetimes in the length and velocity forms is less than 0.9%, which is highly satisfactory. All results are available at Strasbourg Astronomical Data Center (CDS)

Table 3.3.2: Comparison of calculated and observed excitation energies are presented as differences (cm^{-1}). E_{Our} are energies from the present calculations. Differences between: our and observed energies (NIST database [81]) - ΔE^a, our and energies from [96], [65], [69] - E^b, E^c and E^d respectively.

	Ti IX		V X		Cr XI			Mn XII			Fe XIII		
LSJ	E_{Our}	ΔE^a	E_{Our}	ΔE^a	E_{Our}	ΔE^b	ΔE^a	E_{Our}	ΔE^b	ΔE^a	E_{Our}	ΔE^b	ΔE^c
						$3s^2\,3p^2$							
$^3P_0$	0	0	0	0	0	0	0	0	0	0	0	0	0
$^3P_1$	3103	-16	4172	-8	5521	-15	-5	7204	4	19	9281	-22	-8
$^3P_2$	7268	-14	9411	-10	11976	-4	6	15008	-2	13	18553	-9	14
$^1D_2$	28741	186	32691	182	37178	184	-154	42317	177	-144	48236	166	-85
$^1S_0$	61442	342	68109	358	75319	339	-114	83188	358	-100	91839	328	-3
						$3s\,3p^3$							
$^5S^o_2$	144818	-462	161021		177922	-548	-37	195600	-300	201	214152	-472	-84
$^3D^o_1$	200145	-64	220911	-73	242280	-66	34	264323	5433	5520	287123	-82	-6
$^3D^o_2$	200228	-65	221004	-68	242383	-73	28	264442	-108	-21	287270	-86	-8
$^3D^o_3$	200925	-75	222023	-81	243843	-73	32	266493	-117	-23	290095	-85	-1
$^3P^o_0$	230604	80	254017	81	278139	80	74	303083			328974	47	53
$^3P^o_1$	230725	80	254220	73	278462	68	69	303572	-118	-142	329689	52	65
$^3P^o_2$	230830	76	254404	67	278757	59	62	304016	26	6	330323	41	52
$^1D^o_2$	254167	139	280079	110	306672	102	49	334085	115	55	362482	75	9
$^3S^o_1$	300019	75	327993	91	356512	88	107	385669	39	20	415577	115	57
$^1P^o_1$	311445	358	341696	361	372822	392	68	404986	236	-166	438365	279	-81
						$3s^2\,3p\,3d$							
$^3F^o_2$	308803		338884		369085			399512			430277	153	5
$^3F^o_3$	311421		342293		373442			404990			437064	145	-14
$^3F^o_4$	315144		347179		379747			413009			447134	133	-42
$^3P^o_2$	353012	380	386028	238	419210	230	492	452675	255	479	486542	184	45
$^3P^o_1$	357172	210	391382	42	425721	241	513	460265	265	554	495102	160	300
$^1D^o_2$	357986		392438		427337	247	234	462825	125	130	499060	190	55
$^3P^o_0$	358828	401	393750		429091			465011			501676	162	153
$^3D^o_1$	364792	378	399451	321	434505	265	576	470173	273	510	506661	156	176
$^3D^o_2$	365987	376	401003	263	436442	232	595	472504	244	559	509394	144	191
$^3D^o_3$	366458	384	401468	258	436831	281	703	472718	168	558	509303	127	303
$^1F^o_3$	402567	796	440750	660	479159	569	489	517989	629	544	557432	521	392
$^1P^o_1$	412714	894	451743		491065	735	525	530876	736	534	571376	633	444

Continued Table 3.3.2

	Co XIV			Ni XV			Cu XVI			Zn XVII		
LSJ	E_{Our}	ΔE^b	ΔE^a	E_{Our}	ΔE^b	ΔE^d	E_{Our}	ΔE^b	ΔE^a	E_{Our}	ΔE^b	ΔE^a
						$3s^2\,3p^2$						
$^3P_0$	0	0	0	0	0	0	0	0	0	0	0	0
$^3P_1$	11819	-25	2	14886	-31	5	18560	-37	7	22917	-39	16
$^3P_2$	22658	-3	18	27369	-7	18	32742	12	38	38829	-12	18
$^1D_2$	55077	156	-128	62993	141	-122	72146	130	-109	82705	111	-98
$^1S_0$	101404	324	-120	112033	314	-123	123873	323	-100	137087	332	-73

Continued Table 3.3.2

	Co XIV			Ni XV			Cu XVI			Zn XVII		
LSJ	E_{Our}	ΔE^b	ΔE^a	E_{Our}	ΔE^b	ΔE^d	E_{Our}	ΔE^b	ΔE^a	E_{Our}	ΔE^b	ΔE^a
						$3s\,3p^3$						
$^5S^o_2$	233663			254244	-456	59	275972	-458	77	298957	-363	183
$^3D^o_1$	310753			335306	-94	-2	360845	-399	-293	387465		0
$^3D^o_2$	310953	-97	-9	335603	-79	12	361312	68	173	388217		0
$^3D^o_3$	314771	-109	-8	340667	-127	-18	367909	-209	-81	396663	-453	-312
$^3P^o_0$	355936			384119			413652		0	444701		0
$^3P^o_1$	356950			385518	58	34	415537	36	28	447187		0
$^3P^o_2$	357813	53	32	386639	49	34	416924	-633	-629	448815	-1388	-1369
$^1D^o_2$	392023	13	-31	422905	50	16	455309	-8891	-8906	489461		0
$^3S^o_1$	446342	162	100	478103	62	-23	510977	151	54	545123	152	39
$^1P^o_1$	473132	382	7	509487	320	-42	547605	270	-70	587699	263	-60
						$3s^2\,3p\,3d$						
$^3F^o_2$	461484			493257			525698		0	558949		0
$^3F^o_3$	469780			503269			537635	3135	3140	573014		0
$^3F^o_4$	482285			518644			556370	3070	3068	595659		0
$^3P^o_2$	520911	111	297	555903	106	276	591616	-30	134	628182	12	168
$^3P^o_1$	530323	93	418	566046	246	565	602369	50	363	639423	-42	255
$^1D^o_2$	536193	153	205	574394	127	190	613806	116	194	654611	21	106
$^3P^o_0$	539240			577876			617732	-73	41	658989	-119	-3
$^3D^o_1$	544149	49	206	582820	60	195	622823	11	146	664346	-43	93
$^3D^o_2$	547305	75	-129	586447	68	279	627006	81	294	669200	41	242
$^3D^o_3$	546744	34	849	585218	33	372	624874	4	335	665894	-52	268
$^1F^o_3$	597664	414	339	638880	403	327	681247	314	245	724968	267	203
$^1P^o_1$	612749	579	404	655198			698904	380	222	744082	468	320

Continued Table 3.3.2

	Ga XVIII		Ge XIX		Sr XXV		Zr XXVII	Mo XXIX	
LSJ	E_{Our}	ΔE^a	E_{Our}	ΔE^a	E_{Our}	ΔE^a	E_{Our}	E_{Our}	ΔE^a
					$3s^2\,3p^2$				
$^3P_0$	0	0	0	0	0	0	0	0	0
$^3P_1$	28043	-47	34021	-56	92950	-125	123752	161571	-149
$^3P_2$	45697	-3	53413	1	122240	-20	156100	385223	-257
$^1D_2$	94844	114	108737	87	239120	-80	305128	196874	-36
$^1S_0$	151841	331	168307	337	313384	654	384130	468947	727
					$3s\,3p^3$				
$^5S^o_2$	323275		349019		537112	-856	613824	698220	
$^3D^o_1$	415232		444235	-455	648560	-1275	730166	819702	
$^3D^o_2$	416437		446132	-27	665804	1158	760367	869047	
$^3D^o_3$	427069	-491	459300		700704		803968	921304	
$^3P^o_0$	477410		511955		767747		876205	999158	
$^3P^o_1$	480622		516029	98	779904	28	891918	1018480	
$^3P^o_2$	482417	2443	517845	-3709	772281		1003297	979622	
$^1D^o_2$	525573		563884		845815		952487	1144648	
$^3S^o_1$	580681	171	617826	181	884118	274	994084	1116909	159
$^1P^o_1$	629950	180	674558	295	1007850	-423	1144829	1296465	

Continued Table 3.3.2

	Ga XVIII		Ge XIX		Sr XXV		Zr XXVII	Mo XXIX	
LSJ	E_{Our}	ΔE^a	E_{Our}	ΔE^a	E_{Our}	ΔE^a	E_{Our}	E_{Our}	ΔE^a
					$3s^2\,3p\,3d$				
$3F_2^o$	593137		628432		882783		872869	1068014	
$3F_3^o$	609509		647253		906676		1008781	1120615	
$3F_4^o$	636683		679642		989440		1117851	1262081	
$3P_2^o$	665710	-110	704337	-44	967289	-241	1071526	1190353	
$3D_1^o$	677315	-82	716185	-81	971435	-297	1070912	1179034	
$1D_2^o$	696963	67	741045	24	1052275	-196	1230113	1319351	-499
$3P_0^o$	701805	-165	746363		1060646	-319	1188087	1329792	
$3P_1^o$	707554	-56	752647	-120	1075683	173	1210927	1366114	
$3D_2^o$	713226	-34	759307	-123	1091772	-284	1178673	1386247	
$3D_3^o$	708435	-153	752681	-111	1064175	-335	1190295	1330469	-571
$1F_3^o$	770223	237	817220	184	1147847	-131	1282248	1432196	-434
$1P_1^o$	790924	447	839655	405	1184571	295	1325771	1484183	

Table 3.3.3: Comparison of lifetimes (s). τ_l are values from the present calculation in length form. $\tau_{MCHF-BP}$ are values from [84].

	Ti IX		V X		Cr XI	
Level	τ_l	$\tau_{MCHF-BP}$	τ_l	$\tau_{MCHF-BP}$	τ_l	$\tau_{MCHF-BP}$
$3s^2\,3p^2\ ^3P_1$	1.883	2.023	7.787[-1]	8.117[-1]	3.379[-1]	3.421[-1]
$3s^2\,3p^2\ ^3P_2$	1.052	1.194	5.346[-1]	5.925[-1]	2.901[-1]	3.147[-1]
$3s^2\,3p^2\ ^1D_2$	6.508[-2]	7.186[-2]	3.479[-2]	3.796[-2]	1.921[-2]	2.073[-2]
$3s^2\,3p^2\ ^1S_0$	7.445[-3]	7.934[-3]	4.212[-3]	4.436[-3]	2.463[-3]	2.564[-3]
$3s\,3p^3\ ^5S_2^o$	5.005[-7]	5.337[-7]	2.938[-7]	3.083[-7]	1.786[-7]	1.850[-7]
$3s\,3p^3\ ^3D_1^o$	1.203[-9]	1.196[-9]	9.824[-10]	9.752[-10]	8.155[-10]	8.090[-10]
$3s\,3p^3\ ^3D_2^o$	1.249[-9]	1.237[-9]	1.028[-9]	1.016[-9]	8.625[-10]	8.502[-10]
$3s\,3p^3\ ^3D_3^o$	1.334[-9]	1.317[-9]	1.113[-9]	1.097[-9]	9.482[-10]	9.326[-10]
$3s\,3p^3\ ^3P_0^o$	4.368[-10]	4.255[-10]	3.673[-10]	3.578[-10]	3.140[-10]	3.058[-10]
$3s\,3p^3\ ^3P_1^o$	4.425[-10]	4.373[-10]	3.717[-10]	3.695[-10]	3.170[-10]	3.176[-10]
$3s\,3p^3\ ^3P_2^o$	4.693[-10]	4.555[-10]	3.979[-10]	3.864[-10]	3.429[-10]	3.331[-10]
$3s\,3p^3\ ^1D_2^o$	3.179[-10]	3.173[-10]	2.647[-10]	2.626[-10]	2.264[-10]	2.234[-10]
$3s\,3p^3\ ^3S_1^o$	2.629[-11]	2.463[-11]	2.348[-11]	2.205[-11]	2.118[-11]	1.996[-11]
$3s^2\,3p\,3d\ ^3F_2^o$	9.485[-9]	1.088[-8]	5.825[-9]	6.511[-9]	3.729[-9]	4.071[-9]
$3s^2\,3p\,3d\ ^3F_3^o$	1.533[-8]	1.844[-8]	9.704[-9]	1.138[-8]	6.331[-9]	7.245[-9]
$3s\,3p^3\ ^1P_1^o$	4.268[-11]	4.454[-11]	3.676[-11]	3.912[-11]	3.199[-11]	3.474[-11]
$3s^2\,3p\,3d\ ^3F_4^o$	6.952[-2]		5.192[-2]		3.983[-2]	
$3s^2\,3p\,3d\ ^3P_2^o$	2.898[-11]	2.757[-11]	2.590[-11]	2.452[-11]	2.350[-11]	2.220[-11]
$3s^2\,3p\,3d\ ^3P_1^o$	3.147[-11]	2.964[-11]	2.760[-11]	2.614[-11]	2.421[-11]	2.304[-11]
$3s^2\,3p\,3d\ ^1D_2^o$	2.819[-11]	2.568[-11]	2.529[-11]		2.265[-11]	
$3s^2\,3p\,3d\ ^3P_0^o$	3.256[-11]	3.038[-11]	2.927[-11]	2.737[-11]	2.652[-11]	2.485[-11]
$3s^2\,3p\,3d\ ^3D_1^o$	2.135[-11]	1.987[-11]	1.966[-11]	1.827[-11]	1.836[-11]	1.705[-11]
$3s^2\,3p\,3d\ ^3D_2^o$	2.153[-11]	2.007[-11]	1.971[-11]	1.839[-11]	1.825[-11]	1.705[-11]
$3s^2\,3p\,3d\ ^3D_3^o$	2.144[-11]	2.003[-11]	1.950[-11]	1.824[-11]	1.788[-11]	1.675[-11]
$3s^2\,3p\,3d\ ^1F_3^o$	1.957[-11]	1.834[-11]	1.787[-11]	1.676[-11]	1.645[-11]	1.545[-11]
$3s^2\,3p\,3d\ ^1P_1^o$	2.547[-11]	2.360[-11]	2.312[-11]	2.147[-11]	2.116[-11]	1.970[-11]

http://cdsarc.u-strasbg.fr/viz-bin/qcat?J/A+A/585/A26. In Tables 3.3.3 and 3.3.4 we compare calculated lifetimes in length form with lifetimes obtained by Froese Fischer *et al.* with the MCHF Breit-Pauli method [84]. The latter only accounted for valence electron correlation, which affects the accuracy of the lifetimes and transition rates, mainly for the low Z ions [86, 87]. In some sense the differences between the current lifetimes and the lifetimes by Froese Fischer *et al.* [84] illustrates the effects of core-valence correlation.

Table 3.3.4: Comparison of lifetimes (s). τ_l are values from the present calculation in length form. $\tau_{MCHF-BP}$ are values from [84].

	Mn XII		Fe XIII	
Level	τ_l	$\tau_{MCHF-BP}$	τ_l	$\tau_{MCHF-BP}$
$3s^2\,3p^2\ ^3P_1$	1.531[-1]	1.507[-1]	7.218[-2]	6.904[-2]
$3s^2\,3p^2\ ^3P_2$	1.673[-1]	1.780[-1]	1.022[-1]	1.068[-1]
$3s^2\,3p^2\ ^1D_2$	1.089[-2]	1.164[-2]	6.311[-3]	6.679[-3]
$3s^2\,3p^2\ ^1S_0$	1.484[-3]	1.529[-3]	9.185[-4]	9.368[-4]
$3s\,3p^3\ ^5S^o_2$	1.118[-7]	1.140[-7]	7.183[-8]	7.223[-8]
$3s\,3p^3\ ^3D^o_1$	6.852[-10]	6.795[-10]	5.805[-10]	5.761[-10]
$3s\,3p^3\ ^3D^o_2$	7.341[-10]	7.213[-10]	6.321[-10]	6.187[-10]
$3s\,3p^3\ ^3D^o_3$	8.206[-10]	8.058[-10]	7.194[-10]	7.055[-10]
$3s\,3p^3\ ^3P^o_0$	2.718[-10]	2.646[-10]	2.376[-10]	2.312[-10]
$3s\,3p^3\ ^3P^o_1$	2.734[-10]	2.765[-10]	2.377[-10]	2.433[-10]
$3s\,3p^3\ ^3P^o_2$	2.990[-10]	2.908[-10]	2.630[-10]	2.561[-10]
$3s\,3p^3\ ^1D^o_2$	1.979[-10]	1.942[-10]	1.763[-10]	1.721[-10]
$3s\,3p^3\ ^3S^o_1$	1.926[-11]	1.819[-11]	1.762[-11]	1.669[-11]
$3s^2\,3p\,3d\ ^3F^o_2$	2.474[-9]	2.643[-9]	1.692[-9]	1.773[-9]
$3s^2\,3p\,3d\ ^3F^o_3$	4.242[-9]	4.746[-9]	2.910[-9]	3.188[-9]
$3s\,3p^3\ ^1P^o_1$	2.809[-11]	3.113[-11]	2.486[-11]	2.808[-11]
$3s^2\,3p\,3d\ ^3F^o_4$	3.121[-2]		2.487[-2]	
$3s^2\,3p\,3d\ ^3P^o_2$	2.155[-11]	2.034[-11]	1.989[-11]	1.879[-11]
$3s^2\,3p\,3d\ ^3P^o_1$	2.129[-11]	2.031[-11]	1.881[-11]	1.795[-11]
$3s^2\,3p\,3d\ ^1D^o_2$	2.030[-11]	1.894[-11]	1.822[-11]	1.708[-11]
$3s^2\,3p\,3d\ ^3P^o_0$	2.418[-11]	2.271[-11]	2.215[-11]	2.085[-11]
$3s^2\,3p\,3d\ ^3D^o_1$	1.734[-11]	1.611[-11]	1.648[-11]	1.535[-11]
$3s^2\,3p\,3d\ ^3D^o_2$	1.705[-11]	1.595[-11]	1.533[-11]	1.440[-11]
$3s^2\,3p\,3d\ ^3D^o_3$	1.651[-11]	1.549[-11]	1.605[-11]	1.505[-11]
$3s^2\,3p\,3d\ ^1F^o_3$	1.526[-11]	1.434[-11]	1.422[-11]	1.339[-11]
$3s^2\,3p\,3d\ ^1P^o_1$	1.950[-11]	1.819[-11]	1.805[-11]	1.688[-11]

In Table 3.3.5 we compare the lifetimes for the $3s^2 3p3d\ ^3F^o_2$ and $3s^2 3p3d\ ^3F^o_3$ states with values obtained from MCDHF calculations [85] and MR-MP calculations [96], and with experimental lifetime values from beam-foil measurements [103]. The current lifetimes are shorter than those of the other calculations, in better agreement with experiment.

In Table 3.3.6 transition rates for important lines in Fe XIII appearing in EUV

Table 3.3.5: Comparison of lifetimes (ns) for $3s^2 3p3d\ ^3F_2^o$ and $3s^2 3p3d\ ^3F_3^o$ in length (l) and velocity (v) forms, from calculations and from experiment. MCDHF is from [85], MR-MP is from [96] and "Our" is from the present calculations. The experimental lifetimes are from beam-foil measurements [103].

	MCDHF		MR-MP		Our		Exp.
				$3s^2 3p3d\ ^3F_2^o$			
	(l)	(v)	(l)	(v)	(l)	(v)	
$Z=26$	1.94	1.91	2.01	2.01	1.69	1.67	
$Z=27$	1.29	1.19	1.37	1.35	1.19	1.18	
$Z=28$	0.92	0.85	0.98	0.97	0.85	0.84	
$Z=29$	0.67	0.62	0.71	0.71	0.63	0.62	
				$3s^2 3p3d\ ^3F_3^o$			
$Z=26$	3.29	3.32	3.37	3.38	2.91	2.93	3.0 ±0.2
$Z=27$	2.18	1.87	2.34	2.30	2.04	2.05	1.8 ±0.2
$Z=28$	1.55	1.32	1.67	1.63	1.46	1.47	1.45 ±0.08
$Z=29$	1.13	0.96	1.21	1.18	1.06	1.07	1.01 ±0.05

Table 3.3.6: Transition rates for Fe XIII lines between states of $3s^2 3p3d$ and $3s^2 3p^2$ configurations (first and second columns, respectively) appearing in EIS, adapted from [64]. λ_{obs} wavelengths from EIS [107], λ_{Our} (Å) and A_{Our} are from present calculations, A_{CHI} from CHIANTI, A_{AK} [88], A_K [63], A_{NIST} [81]. The relative differences between the A values in the length and velocity forms for the present calculation are between 0.1 and 0.3 %.

Transition	λ_{obs} [107]	λ_{Our}	A_{Our}	A_{CHI} [106]	A_{AK} [88]	A_K [63]	A_{NIST} [81]
$^1F_3^o - {}^1D_2$	196.52	196.39	6.675[10]	6.862[10]	8.275[10]	7.3908[10]	6.80[10]
$^3D_2^o - {}^3P_1$	200.02	199.95	2.300[10]	2.368[10]	2.761[10]	2.9279[10]	
$^3P_1^o - {}^3P_0$	202.04	201.98	4.548[10]	4.643[10]	5.100[10]	4.5491[10]	
$^3P_0^o - {}^3P_1$	203.17	203.09	4.515[10]	4.712[10]	5.586[10]	1.6005[10]	
$^3D_3^o - {}^3P_2$	203.83	203.77	6.276[10]	6.475[10]	7.948[10]	6.9486[10]	6.50[10]
$^3D_2^o - {}^3P_2$	203.79	203.73	3.320[10]	3.361[10]	3.566[10]	3.5499[10]	
$^1D_2^o - {}^3P_1$	204.26	204.17	1.975[10]	2.015[10]	1.540[9]	4.9464[10]	
$^3D_1^o - {}^3P_2$	204.94	204.87	1.259[10]	1.276[10]	1.392[10]	1.1984[10]	
$^3P_2^o - {}^3P_1$	209.62	209.53	1.766[10]	1.852[10]	3.252[10]	2.1115[10]	
$^3P_1^o - {}^3P_2$	209.92	209.84	6.513[9]	7.227[9]	1.079[10]	9.3164[9]	

Imaging Spectrometer (EIS) are presented (see for example [64]). The rates of the different calculations scatter, but there is a reasonable agreement between the rates of the present calculations and the rates given by CHIANTI [106]. Our Table 3.3.6 is an adaptation of Table 1 from [64].

3.3.3 Conclusions

MCDHF and subsequent RCI calculations were performed for states of the $3s^2 3p^2$, $3s3p^3$, and $3s^2 3p3d$ configurations in the Si-like ions Ti IX - Ge XIX,

Sr XXV, Zr XXVII, and Mo XXIX. Excitation energies, lifetimes and transition rates are presented. Energies from the RCI calculations are in excellent agreement with observations and computed wavelength are almost of spectroscopic accuracy, aiding line identification in spectra. Uncertainties of the transition rates are estimated by δT, as suggested in [80]. For most of the strongest transitions δT is below 1%. For weaker transitions the uncertainty δT is somewhat larger, from a few percent up to 10%. We thus argue that the transition rates are highly accurate and may serve as benchmark for other calculations.

Chapter 4

Energy spectrum of Er^{3+} [A3, A4]

Experimental searches of permanent EDM are often performed on heavy elements, because EDM enhancement factor increase rapidly with atomic number Z. Calculations of enhancement factors require knowledge of correlation effects for energy levels in the region of heavy elements. Another reason to explore Er^{3+} ion properties is, that Er_2O_3 coating will be used in fusion reactor blanket systems for electric insulation and tritium permeation barriers [108], because of its chemical stability in corrosive liquid coolant and tritium breeders, e.g. liquid Li or FLiBe. However, neutron damage of the coating is a concern, and luminescence measurements were proposed as a method for characterizing radiation-induced defects [109]. It is, therefore, required to elucidate relations between optical emission spectra of the ground configuration of Er^{3+} in Er_2O_3, as observed in the luminescence measurements, and defect structures and degree of crystallinity. However, even for isolated (free) ions of Er^{3+}, as well as for other Lanthanoids and Actinoids and their ions, spectroscopic data are not available. This work addresses the lack of data.

There are several theoretical methods for obtaining the energy spectrum and transition rates in many-electron atoms and ions, such as: different versions of the many-body perturbation theory [110] - [112] the configuration interaction method [113], the random phase approximation with exchange [113], the incomplete variable separation method [114], the multiconfiguration approximation, etc. Lately, the majority of theoretical *ab initio* calculations of energy spectra and transition rates of atoms and ions with open shells have been carried out using configuration interaction, multiconfiguration Hartree-Fock [82, 115] or multiconfiguration Dirac-Hartree-Fock (MCDHF) [35] methods.

The energy levels of free Er^{3+} were obtained by Carter from emission spectra of a high-current spark [116]. However, most authors [117] - [120] used semi-empirical methods to obtain spectroscopic data for Er^{3+}. These methods rely on measurements of Stark components in erbium doped crystals (LaF_3, $LiYF_3$ and

$ZnGa_2O_4$) that determine centers of gravity. Then, by using different approximations such as the Wybourne theory [121] and superposition models [122], the energy spectrum is derived for the free ion. There are no experimental data for transition rates.

The basic and novel idea of this work is to study the energy spectrum and the transition parameters for the [Xe]$4f^{11}$ ground configuration of Er^{3+} using an *ab initio* approach. The calculations are based on MCDHF and RCI [123] methods. Principles of these methods for energy level and transition rate calculations are presented in sections 2.2.1 and 2.2.2. Methodologies and strategies used to include electron correlation effects are described in section 4.1. This is followed by an evaluation of energy levels and comparison with results of other authors in section 4.2. The E2 and M1 transition rates, line strengths, and weighted oscillator strengths for transitions between states of the ground configuration are presented in section 4.3 . All results are summarized in section 4.4.

4.1 Configuration state function basis

In this work calculations were done by configuration, i.e. wave functions for all states belonging to a specific configuration were determined simultaneously in an EOL calculation [38]. The expansions in expression (2.2.1), defining the ASFs, were obtained using the active set method [70, 124]. Here CSFs of a specified parity and J symmetry are generated by substituting orbitals from one or more reference configurations to orbitals in an active set. By applying restrictions on the allowed substitutions, different electron correlation effects can be targeted. To monitor the convergence of the calculated energies and transition parameters, the active sets are increased in a systematic way by adding layers of correlation orbitals.

A careful analysis showed that the states of the [Xe]$4f^{11}$ ground configuration in Er^{3+} are well described in a single reference configuration Dirac-Hartree-Fock (DHF) model. Below different strategies for generating the expansions based on the single reference [Xe]$4f^{11}$ active set method are described.

In the description of the method $4f$ orbital will be considered the only valence shell. $1s$, $2s$, $2p$, $3s$, $3p$, $3d$, $4s$, $4p$, $4d$, $5s$, $5p$ (or [Xe]) will be considered core shells, even though $5s$ and $5p$ have similar binding energies as $4f$. In all calculations the radial orbitals of the reference configuration were taken from the initial DHF calculation. The energy functional, on which the orbitals were

optimised, was the weighted energy average of the two lowest states of [Xe]$4f^{11}$ with J=1/2, the six lowest states with J=3/2, the seven lowest states with, respectively, J=5/2, 7/2, 9/2, the five lowest states with J=11/2, the three lowest states with J=13/2, three lowest with J=15/2, and finally the lowest state with J=17/2.

1. **S V strategy** – the CSFs were generated by single (S) substitutions from the valence (V) shell ($4f$ shell) to orbitals in active sets characterized by principal quantum numbers $n = 5-9$, and angular symmetries p, f, h, k (the orbitals s, d, g, i lead to configurations with opposite symmetry in the case of S substitutions). In this strategy the inactive core is [Xe]. The RSCF calculations for each layer of orbitals were followed by RCI calculations, including the Breit interaction and QED corrections. At all steps only new orbitals were optimised.

2. **SD VV strategy** – the CSFs were generated by single and double (SD) substitutions from the valence (VV) shell to orbitals in active sets characterized by principal quantum numbers $n = 5-7$, and angular symmetries s, p, d, f. In this strategy the inactive core is again [Xe]. The RSCF calculations for each layer of orbitals were followed by RCI calculations, including the Breit interaction and QED corrections. At all steps only new orbitals were optimised.

3. **S V+C strategy** – the CSFs were generated by S substitutions from the core (C) shells ($5s$, $5p$ shells) and the valence (V) shell to orbitals in active sets characterized by principal quantum numbers $n = 5-9$, and angular symmetries $s-i$. In this strategy the inactive core is $1s^2 2s^2 2p^6 3s^2 3p^6 3d^{10}$ $4s^2 4p^6 4d^{10}$. The RSCF calculations for each layer of orbitals were followed by RCI calculations, including the Breit interaction and QED corrections. At all steps only new orbitals were optimised.

4. **SD VV+CC+CV strategy** – the CSFs were generated by SD substitutions from the core (CC) shells ($5s$ and $5p$) and the valence (VV) shell to orbitals in active sets characterized by principal quantum numbers $n = 5, 6$, and angular symmetries $s-h$. In this strategy the inactive core is as in **S V+C strategy**. The radial orbitals were taken from the S V+C strategy and only RCI calculations, including the Breit interaction and QED corrections, were done.

5. **SD V+C+CV strategy** – the CSFs were generated by S substitutions from the core (C) shells ($5s$, $5p$ or other closed core shells that were opened step by step as presented in the tables) and the valence (V) shell to orbitals in active sets characterized by principal quantum numbers $n = 5,6$, and angular symmetries $s-h$. Double (D) substitutions were restricted in such a way, that one substitution would be from the core and another from the valence shell (CV). The radial orbitals were taken from the S V+C strategy and only RCI calculations, including the Breit interaction and QED corrections, were done.

In the Table 4.1.1 of the expansion size N_{CSF} (number of CSFs) is displayed for each strategy.

Table 4.1.1: Summary the expansion size N_{CSF} in different strategies for Er^{3+}.

Strategy	open core	DHF	$n=5$	$n=6$	$n=7$	$n=8$	$n=9$
SV		41	1229	4 443	7 657	12 200	16 743
SD VV		41	21 153	120 888	302 868		
S V+C	5*	41	5 853	18 438	32 120	45 802	59 484
SD VV+CC+CV	5*	41	634 453	4 311 822			
	5*4d	41	2 230 820				
SD V+C+CV	5*	41	10 882	32 155	56 275		
	5*4d	41	40 517	106 047	187 856	269 665	
	5*4d4p	41	66 407	174 558	308 987		
	5*4*	41	77 272	202 141	357 885		
	5*4*3d	41	134 340	354 974			
	5*4*3d3p	41	181 369	474 742			
	5*4*3*	41	198 197	519 450			
	5*4*3*2p	41	252 756				
	5*4*3*2*	41	273 079				

4.2 Energy level structure

The Er^{3+} ion has previously not been thoroughly investigated. To the knowledge of the authors there have been practically no publications with *ab initio* theoretical calculations for isolated Er^{3+}. Thus, results based on the different strategies, including various types of correlations and substitutions to large active sets, need to be internally compared and benchmarked.

The energy levels from calculations using the S V and SD VV strategies, the S V+C and SD VV+CC+CV strategies, the SD V+C+CV strategies are shown in tables 4.2.1–4.2.3. Energies of levels are given in the tables in the form of

Table 4.2.1: Energy levels and differences from initial approximation (cm^{-1}) for the [Xe]$4f^{11}$ ground configuration from RCI calculations that include S V and SD VV correlation: *LSJ* denotes the leading *LS* term and *J* value of the level. In the second row the *n* of the active set is given.

LSJ	DHF	**S V**					**SD VV**			NIST
		5	6	7	8	9	5	6	7	[81]
$^4I^1_{15/2}$	0	0	0	0	0	0	0	0	0	0
$^4I^1_{13/2}$	6207	6204	13	18	1	1	6255	17	24	6480
$^4I^1_{11/2}$	10155	10168	-6	17	4	3	10168	8	13	10110
$^4I^1_{9/2}$	12965	12998	-42	2	-31	-34	12928	-7	-6	12350
$^4F^1_{9/2}$	19084	18693	-753	-1140	-749	-756	18451	-319	-369	15180
$^4S^1_{3/2}$	23696	23279	-503	-915	-498	-502	22996	-338	-386	18290
$^2H^2_{11/2}$	22402	22484	-371	-281	-363	-375	21975	-171	-211	
$^4F^1_{7/2}$	25030	24459	-888	-1451	-880	-880	24347	-377	-429	20400
$^4F^1_{5/2}$	27091	26512	-916	-1486	-907	-910	26376	-390	-444	22070
$^4F^1_{3/2}$	27351	26950	-823	-1214	-813	-820	26741	-372	-425	22410
$^2G^1_{9/2}$	27460	27356	-423	-514	-410	-424	26929	-163	-192	
$^4G^1_{11/2}$	31711	31553	-1093	-1243	-1085	-1100	31151	-286	-378	

Table 4.2.2: Energy levels and differences from initial approximation (cm^{-1}) for the [Xe]$4f^{11}$ ground configuration from RCI calculations that include S V+C and SD VV+CC+CV correlation: 5^* means, that all shells from the core with $n = 5$ are open for SD substitutions, $4d$ means, that the $4d$ shell is open for SD substitutions. In the third row the *n* of the active set is given. *LSJ* denotes the leading *LS* term and *J* value of the level.

LSJ	**S V+C**					**SD VV+CC+CV**			NIST
	5^*					5^*		5^*4d	
	5	6	7	8	9	5	6	5	[81]
$^4I^1_{15/2}$	0	0	0	0	0	0	0	0	0
$^4I^1_{13/2}$	6215	-1	5	6	6	6379	12	6502	6480
$^4I^1_{11/2}$	10133	-2	7	10	9	10268	-35	10332	10110
$^4I^1_{9/2}$	12913	-22	-11	-9	-9	12957	-130	12889	12350
$^4F^1_{9/2}$	17809	-816	-808	-808	-808	17335	-845	16764	15180
$^4S^1_{3/2}$	21904	-564	-554	-553	-553	21459	-836	20650	18290
$^2H^2_{11/2}$	21845	-361	-342	-341	-341	21305	-589	20747	
$^4F^1_{7/2}$	23421	-1018	-1007	-1005	-1006	23074	-1026	22511	20400
$^4F^1_{5/2}$	25383	-1038	-1024	-1022	-1022	25013	-1076	24406	22070
$^4F^1_{3/2}$	25780	-914	-901	-900	-900	25364	-1009	24695	22410
$^2G^1_{9/2}$	26768	-314	-297	-294	-294	26376	-593	25891	
$^4G^1_{11/2}$	30142	-1156	-1142	-1141	-1141	29604	-1125	28964	

Table 4.2.3: Energy levels and differences from initial approximation (cm^{-1}) for the $[Xe]4f^{11}$ ground configuration from RCI calculations that include SD V+C+CV correlations: 5^* means, that all shells from the core with $n = 5$ are open for SD substitutions (5^*4^* - core with $n = 5,4$ are is open). In the second row the n of the active set is given. *LSJ* denotes the leading *LS* term and *J* value of the level.

LSJ	5^*			5^*4d				5^*4d4p			5^*4^*		
	5	6	7	5	6	7	8	5	6	7	5	6	7
$^4I^1_{15/2}$	0	0	0	0	0	0	0	0	0	0	0	0	0
$^4I^1_{13/2}$	6195	5	12	6305	-47	-27	-45	6322	-31	-10	6323	-32	-10
$^4I^1_{11/2}$	10102	4	14	10165	-2	27	18	10118	35	69	10110	34	69
$^4I^1_{9/2}$	12876	-16	-5	12844	47	78	87	12738	100	139	12724	101	142
$^4F^1_{9/2}$	17773	-820	-814	17100	-416	-413	-329	16796	-306	-294	16768	-311	-295
$^4S^1_{3/2}$	21915	-577	-569	21018	-26	-18	107	20007	219	243	19960	198	227
$^2H^2_{11/2}$	21778	-367	-349	21148	45	70	158	20696	160	203	20632	147	195
$^4F^1_{7/2}$	23368	-1018	-1007	22730	-658	-646	-574	22426	-526	-507	22398	-538	-514
$^4F^1_{5/2}$	25322	-1038	-1025	24642	-654	-637	-556	24244	-500	-474	24200	-520	-490
$^4F^1_{3/2}$	25732	-917	-905	24984	-470	-453	-361	24444	-277	-248	24401	-291	-256
$^2G^1_{9/2}$	26703	-314	-296	26137	118	155	226	25797	220	280	25760	231	296
$^4G^1_{11/2}$	30053	-1151	-1138	29341	-793	-776	-719	29012	-655	-629	28974	-664	-632

Continued ...

LSJ	5^*4^*3d		5^*4^*3d3p		$5^*4^*3^*$		$5^*4^*3^*2p$	$5^*4^*3^*2^*$	NIST
	5	6	5	6	5	6	5	5	[81]
$^4I^1_{15/2}$	0	0	0	0	0	0	0	0	0
$^4I^1_{13/2}$	6326	-25	6329	-17	6328	-17	6328	6328	6480
$^4I^1_{11/2}$	10106	50	10105	61	10104	61	10104	10104	10110
$^4I^1_{9/2}$	12707	128	12704	138	12703	138	12703	12703	12350
$^4F^1_{9/2}$	16698	-252	16679	-252	16678	-253	16678	16678	15180
$^4S^1_{3/2}$	19856	283	19809	284	19807	282	19807	19807	18290
$^2H^2_{11/2}$	20575	199	20553	200	20549	199	20549	20549	
$^4F^1_{7/2}$	22320	-465	22301	-463	22300	-465	22300	22300	20400
$^4F^1_{5/2}$	24116	-443	24091	-439	24089	-442	24089	24089	22070
$^4F^1_{3/2}$	24311	-209	24282	-204	24280	-206	24280	24280	22410
$^2G^1_{9/2}$	25699	295	25685	304	25682	305	25682	25682	
$^4G^1_{11/2}$	28901	-589	28878	-583	28876	-585	28876	28876	

the difference with respect to the $n = 5$ column. For example, for strategy SD V+C+CV 5* in $n = 7$ approximation, the energy of level $^4I^1_{11/2}$ can be obtained by taking the energy in column $n = 5$ (10102 cm^{-1}) and adding the entry displayed in column $n = 7$ (14 cm^{-1}). The tables display the convergence of the energy levels with respect to the increasing n quantum number of the active sets of orbitals, and the increasing number of included configurations. In the last

column of the tables the energies from NIST [81] are given.

As can be seen from the tables the energy levels obtained from different strategies differ considerably from the energies given in the NIST database [81]. The energies obtained in the S substitutions valence (the S V strategy) and SD substitutions valence-valence (the SD VV strategy) approximations agree poorly with experiment and the NIST reference data. The energies are converged at $n = 6$, and further extension of the active set has little impact. Adding valence-valence (the SD VV strategy) correlation to the valence correlation leads to an insignificant change for the energy levels (approx. 0.5%). However, if core correlation is included (the S V+C strategy), the positions of the energy levels approach the experimental values (approx. 5%). The exceptions are levels 2 and 3, where even valence and valence-valence correlations (the S V and SD VV strategies) provide precise predictions. Core-core and core-valence correlations (the SD VV+CC+CV strategy) for the higher levels change energies by less than 2% (see Tables 4.2.1-4.2.3).

It should be noted that the order of the $^4S^1_{3/2}$ and $^2H^2_{11/2}$ levels depends on the strategy. It is obvious that in the cases of the S V and SD VV strategies, independently of the size of the active set, the positions of these levels do not agree with experiment (see Table 4.2.1). However, after adding core correlation with an active set $n = 6$, the positions become correct (see Table 4.2.2). Valence, core and core-valence correlations, when at least the $4d$ shell is opened, lead to the correct positions for these levels already at $n = 5$ (see Table 4.2.3).

The convergence of the positions of levels 5 and 6 (when increasing the active sets and opening deeper closed shells) is demonstrated in Fig. 4.2.1 and Tables 4.2.1-4.2.3. It is seen that calculations with the active set $n = 6$ that include SD substitutions from the valence, core and core-valence shells, when only $4d$ and $4p$ substitutions are taken from the core (the SD V+C+CV $4d$ $4p$ strategy), lead to energy level positions close to the experimental ones. In addition, in this approximation, the order of the $^4S^1_{3/2}$ and $^2H^2_{11/2}$ levels agree with the results of the experiment (see Table 4.2.4). Further increase of the active set or opening of deeper core shells does not significantly change the results (see Fig. 4.2.1). As a matter of fact, similar results for the above mentioned levels are obtained in the SD VV+CC+CV approximation with $n = 6$ (SD substitutions from the valence, valence-valence, core, core-core and core-valence shells to orbitals in the active set $n = 6$). But in the above mentioned case, the ASFs consist of 4 311 822 CSFs whereas in the case of SD V+C+CV $4d$ $4p$ only of 174 558 CSFs. Hence, core-

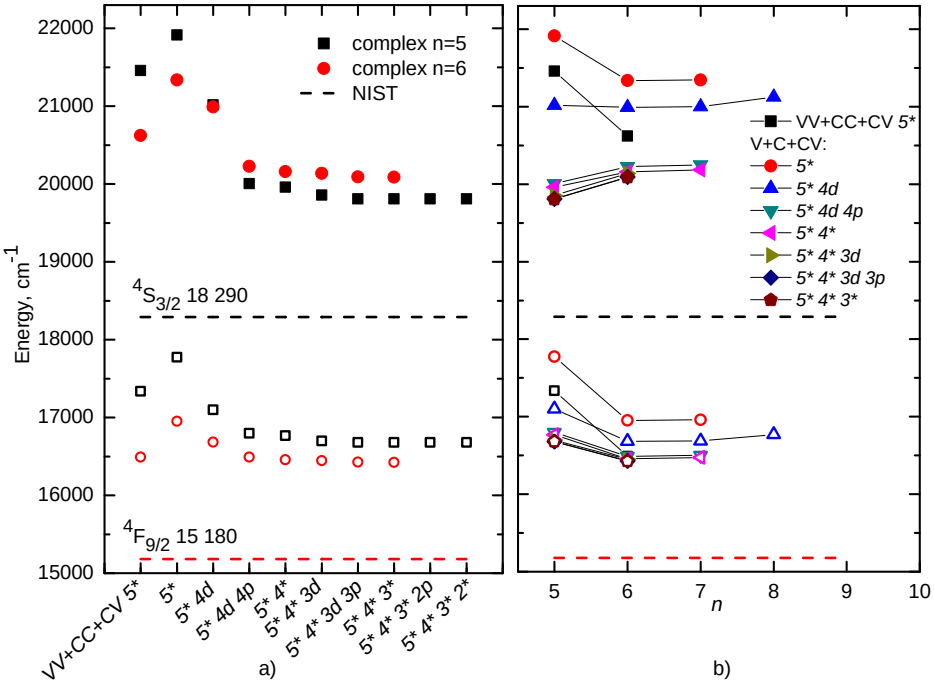

Figure 4.2.1: Convergence of the energy levels $4f^{11}\ {}^4S^1_{3/2}$ (filled symbols) and ${}^4F^1_{9/2}$ (empty symbols) in Er^{3+}: a) opening core shells and b) increasing principal quantum number of the active set in different strategies. In the VV+CC+CV strategy, SD substitutions were made without restrictions. In the other strategies D substitutions were restricted in such a way, that one substitution would be from the core and another from the valence shell.

core, and valence-valence correlations are less important than valence, core and core-valence.

Table 4.2.4 compares computed energy levels with results from other theories and experiment. Levels are notated in the form ${}^{(2S+1)}L^{Nr}_J$ where, instead of the group labels vWU, single character "numbers" Nr are used [125]. In Table 4.2.4 the level we identified as ${}^2G^1_{9/2}$ was originally identified as ${}^2H_{9/2}$ in [117] - [119]. The level identifications in Table 4.2.4 are based on an LS composition analysis (see Table 4.2.5).

SD V+C+CV strategy calculations (see column 'Our' in Table 4.2.4) with $n = 6$ and the core opened for $5^*4^*3^*$ substitutions give the positions of the first three levels in agreement with experiment. For the higher levels the agreement is less satisfactory. Total calculated energy levels are compared with NIST recommended values presented in the last column of the Table.

Experimental data [117] for centers of gravity of Stark manifolds were obtained by measuring Stark levels of the Er^{3+} absorption spectrum in LaF_3 at 77

Table 4.2.4: Comparison of calculated (Our) energy levels (cm^{-1}) of the ground configuration in Er^{3+} with values from semi-empirical (SE) methods and experiment (Exp). Theoretical energies are compared with NIST database recommended values and the errors (Err) are reported. All energies are relative to the ground state.

LSJ	Our	SE				Exp	NIST	Err
		[117]	[118]	[120]	[119]	[116]	[81]	(%)
$^4I^1_{15/2}$	0	0	0	0	0	0	0	
$^4I^1_{13/2}$	6311	6540	6502	6405	6511	6485	6480	2.6
$^4I^1_{11/2}$	10165	10123	10125	10022	10043	10123	10110	0.5
$^4I^1_{9/2}$	12841	12328	12340	12241	12003	12345	12350	4.0
$^4F^1_{9/2}$	16425	15266	15181	15076	14913	15182	15180	8.2
$^4S^1_{3/2}$	20089	18433	18427	18320	18018	18299	18290	9.8
$^2H^2_{11/2}$	20748	19166	19284	19175	18851	19010		
$^4F^1_{7/2}$	21835	20524	20327	20123	20034	20494	20400	7.0
$^4F^1_{5/2}$	23647	22065	21990	21870	21713	22181	22070	7.1
$^4F^1_{3/2}$	24074	22477	22344	22227	21978	22453	22410	7.4
$^2G^1_{9/2}$	25987	24539	24537	24322	23874	24475		
$^4G^1_{11/2}$	28291	26615	26447	26327	25929	26376		
$^4G^1_{9/2}$	29369	27663	27431	27305				
$^2K^1_{15/2}$	29713	27041	27293	27176				
$^2G^1_{7/2}$	30255		27994	27877				
$^2P^1_{3/2}$	33797		31605	31477				
$^2K^1_{13/2}$	34993		32521	32392				
$^4G^1_{5/2}$	35584		33315	33178				
$^2P^1_{1/2}$	35829			33336				
$^4G^1_{7/2}$	35959	28110	33918	33783				
$^2D^1_{5/2}$	37550		34794	34641				
$^2H^2_{9/2}$	37974		36408	36268				
$^4D^1_{5/2}$	42247		38649	38526				
$^4D^1_{7/2}$	43125		39205	39067				
$^2I^1_{11/2}$	44363		40309	40164				
$^2L^1_{17/2}$	44686		40664	40508				
$^2D^1_{3/2}$	44985		42199	42802				
$^4D^1_{3/2}$	46361		42946	42044				
$^2I^1_{13/2}$	46509		42947	42797				
$^4D^1_{1/2}$	50552			46808				
$^2L^1_{15/2}$	50695		46836	46667				
$^2H^1_{9/2}$	51680			46989				
$^2D^2_{5/2}$	52987			48873				
$^2H^1_{11/2}$	54438			50061				
$^2D^2_{3/2}$	58851			54910				
$^2F^2_{7/2}$	60100			55055				
$^2F^2_{5/2}$	68234			62909				
$^2G^2_{7/2}$	72071			64688				
$^2G^2_{9/2}$	75942			68765				
$^2F^1_{5/2}$	103064			93134				
$^2F^1_{7/2}$	107321			96726				

K. Only those lines which persist at 4.2 K were retained. The Stark levels of $^4I_{13/2}$ were obtained in another way. In this case the center was determined from fluorescence lines. Most transitions in the spectrum are from the $^4I_{15/2}$ ground state Stark components to the Stark components of the excited states. The authors of the paper [118] have extended the measured absorption spectrum in the same crystal into the ultraviolet region up to 2000 Å. Thus, more excited levels were obtained. Similar experiments were done on other systems. With the help of small variations of parameters (F_2, F_4, F_6 and ζ), originally described by Wybourne [126], the free ion spectrum [117, 118] was determined from the experimental centers of gravity data. The eigenstates and the corresponding energy levels [120] were found (in *LSJ* coupling) by diagonalizing the interaction matrix defined by the spin-orbit and electrostatic energies. The spin-orbit parameter ζ and the Racah parameters E^1, E^2, E^3 were determined in a fitting procedure in which centers of gravity were taken from [117] and [118]. Semi-empirical data for the spectrum in [119] were evaluated by measuring the Er^{3+} center of gravity in $ZnGa_2O_4$. Energy levels given at NIST [81] were derived from the spectrum of Er^{3+} in LaF_3 crystal. Experimental data of the free ion Er^{3+} were obtained by Carter [116] from emission spectra of a high-current spark. When comparing theory and experiment it is necessary to consider the fact that for free ions the *ab initio* calculations have been performed for the first time in this work.

Table 4.2.5 presents compositions of the ASFs in jj- and *LS*- coupling schemes from the SD V+C+CV strategy. The contributions of CSFs to the compositions are squares of the mixing coefficients expressed in percentages. Quantum "number" Nr is also used in the Table. Numbers in parentheses show the J values of the shell in jj-coupling. For example, the J values of the $4f_-^4$ shell can be 4 (see the string $4f_-^4(4)4f^7$ in the third row) or 2 (see the string $4f_-^4(2)4f^7$ in the seventh row). Other J values of the shells in jj-coupling can be found in [125].

For a given set of ASFs with the same J and parity, the CSFs with the largest contribution were selected. The quantum numbers of these CSFs were used as the labels for the corresponding ASFs. The corresponding CSFs were removed from consideration and the procedure was repeated until all ASFs were labeled. The label for the last ASF may be based on a CSF contribution that is exceedingly small. For example, the level given in the penultimate row of the Table 4.2.5 is designated in *LS*-coupling as $^2G^1_{9/2}$, although this CSF contributes only 18% to this level. For each level 99% of the composition was computed, but in the Table 4.2.5 includes only CSFs with contributions greater than or equal to

Table 4.2.5: The atomic state functions compositions of some levels in the ground configuration [Xe]$4f^{11}$ in Er^{3+} in jj- and LS- coupling.

Level	jj-coupling	LS-coupling
$^4I^1_{15/2}$	**74** $4f^6_-4f^5(15/2)$+**23** $4f^5_-4f^6(6)$	**96**
$^4I^1_{13/2}$	**75** $4f^5_-4f^6(6)$+ **15** $4f^5_-4f^6(4)$	**98**
$^4I^1_{11/2}$	**42** $4f^4_-(4)4f^7$+**23** $4f^5_-4f^6(6)$+**18** $4f^6_-4f^5(11/2)$	**87**+**10** $^2H^2$
$^4I^1_{9/2}$	**29** $4f^4_-(4)4f^7$ + **28** $4f^6_-4f^5(9/2)$+**15** $4f^5_-4f^6(2)$+ +**13** $4f^3_-(9/2)4f^8$+**12** $4f^5_-4f^6(4)$	**71**+**15** $^2H^2$
$^4F^1_{9/2}$	**55** $4f^6_-4f^5(9/2)$+**22** $4f^5_-4f^6(4)$+**12** $4f^5_-4f^6(6)$	**69**+**12** $^4I^1$+**11** $^2G^1$
$^4S^1_{3/2}$	**53** $4f^6_-4f^5(3/2)$+**31** $4f^5_-4f^6(4)$+**12** $4f^4_-(2)4f^7$	**74**+**15** $^2P^1$
$^2H^2_{11/2}$	**57** $4f^6_-4f^5(11/2)$+**24** $4f^4_-(4)4f^7$+**12** $4f^5_-4f^6(4)$	**53**+**31** $^4G^1$+**10** $^4I^1$
$^4F^1_{7/2}$	**62** $4f^5_-4f^6(4)$+**16** $4f^5_-4f^6(6)$+**10** $4f^4_-(2)4f^7$	**92**
$^4F^1_{5/2}$	**3** $4f^5_-4f^6(2)$+**44** $4f^5_-4f^6(4)$+**21** $4f^4_-(2)4f^7$+ + **19** $4f^6_-4f^5(5/2)$+ **9** $4f^4_-(4)4f^7$	**86**+**10** $^2D^1$
$^4F^1_{3/2}$	**36** $4f^5_-4f^6(4)$+**30** $4f^5_-4f^6(2)$+**14** $4f^6_-4f^5(3/2)$ +**12** $4f^4_-(4)4f^7$	**68**+**18** $^2D^1$+**12** $^4S^1$
$^2G^1_{9/2}$	**13** $4f^5_-4f^6(4)$+**31** $4f^5_-4f^6(6)$+**18** $4f^4_-(4)4f^7$+ +**13** $4f^3_-(9/2)4f^8$+**11** $4f^6_-4f^5(9/2)$	**18**+**23** $^2H^2$+**21** $^4F^1$ +**15** $^2G^2$+**11** $^4I^1$
$^4G^1_{11/2}$	**62** $4f^5_-4f^6(6)$+**17** $4f^4_-(2)4f^7$+**10** $4f^4_-(4)4f^7$	**64**+**23** $^2H^2$

10%. An exception is the $^4F^1_{5/2}$ level in jj-coupling. Here we see CSFs with a 3% contribution because levels with larger coefficients were already assigned.

The evaluation of the suitability of the couplings for the classification of energy spectra is performed using the method described in [127]. The square of the largest mixing coefficient (in %), averaged over the states of the configurations considered, serves as a numerical parameter P_s describing the suitability of the coupling scheme. A value of P_s close to **100%** indicates that the coupling scheme is suitable for labeling purposes. The value of P_s is **82%** in LS-coupling and **67%** in jj-coupling for the SD V+C+CV strategy with the $n = 6$ active set and core shells opened up to $n = 3$. The values of P_s show that LS-coupling is more preferable for labeling than jj-coupling.

4.3 Transition parameters

The states of the [Xe]$4f^{11}$ ground configuration undergo M1 and E2 transitions. The line strengths S, weighted oscillator strengths gf, and transition rates A_{ki} (s^{-1}), displayed in Table 4.3.1, are computed based on wave functions from the S V + C strategy with $n = 9$. The transition rates are all very small (for this reason, we provided only five of each type of transitions), of the order of

Table 4.3.1: Transition data for E2 and M1 transitions (S V+C strategy $n = 9$) between states in the [Xe]$4f^{11}$ ground configuration: Leading *LS* term and *J* for lower level *i*, upper level *k*, wavelength λ (Å), line strength *S* (length form), weighted oscillator strength gf (length form), transition rate A_{ki} (length form) (s^{-1}), δT accuracy indicator. The numbers in brackets indicate the powers of ten.

Levels		*J*		λ	*S*	gf	A_{ki}	δT
i	*k*	*i*	*k*					
E2								
$^2H^1$	$^2F^1$	9/2	5/2	1857.66	0.4678	1.225[-8]	3.947	0.22323
$^2H^1$	$^2F^1$	11/2	7/2	1803.91	0.3983	1.139[-8]	2.919	0.14592
$^2G^1$	$^2F^1$	7/2	5/2	1310.09	0.0490	3.658[-9]	2.370	0.62902
$^2G^1$	$^2F^1$	9/2	7/2	1175.28	0.0298	3.083[-9]	1.861	0.65372
$^4G^1$	$^2F^1$	7/2	5/2	1413.64	0.0489	2.904[-9]	1.615	0.61265
M1								
$^4G^1$	$^2F^2$	9/2	7/2	3092.11	0.3182	4.161[-7]	36.29	
$^4D^1$	$^2F^1$	7/2	7/2	1496.03	0.0337	9.101[-8]	33.90	
$^2F^2$	$^2F^1$	7/2	5/2	2227.84	0.0749	1.360[-7]	30.45	
$^4F^1$	$^2D^1$	7/2	5/2	5934.26	1.1740	8.001[-7]	25.26	
$^4G^1$	$^2F^2$	7/2	5/2	2952.02	0.1193	1.634[-7]	20.85	

10 s^{-1} for the M1 transitions, and an order of magnitude smaller for E2. The parameters for the E2 transitions are given in the length gauge. The quantity δT was used as an indication of the accuracy (equation 2.2.8). It has been argued that δT can be used as a rough estimate of the uncertainties of the computed line strengths, which in this case would translate to uncertainties up to 40%. No other theoretical/experimental transition data were previously available for Er^{3+}.

4.4 Conclusions

The MCDHF and RCI methods were used to compute the energy spectrum, line strengths, weighted oscillator strengths, and transitions rates for E2 and M1 transitions between the states of the [Xe]$4f^{11}$ configuration of Er^{3+}. Influence of different types of correlation effects on energy levels are presented in Tables 4.2.1 - 4.2.3 and in Fig. 4.2.1. An analysis of these data shows that values of Er^{3+} energy levels converge when the core is opened up to 5* 4* 3*, and important correlations such as SD V+C+CV are included. Compared with NIST recommended values we see that our *ab initio* calculations for the energy spectrum agree within 9.8% for free ion in SD V+C+CV strategy. By an analysis of the ASFs compositions of the levels in Er^{3+}, we found that *LS*-coupling is preferable to *jj*-coupling.

Chapter 5

Parity nonconservation in He-like sequence [A5]

Gorshkov and Labzovskiĭ [32] and Labzowsky *et al.* [33] have proposed that the mixed hyperfine and weak-quenching can be used to test parity violation effects. The one-photon transition $1s2s\ ^1S_0 \rightarrow 1s^2\ ^1S_0$ of He-like ions is considered a good candidate for these tests and experiments [128] will be carried out at GSI (Gesellschaft für Schwerionenforschung). Level $1s2s\ ^1S_0$ can decay due to several transitions (see left hand side of the Figure 5.0.1):

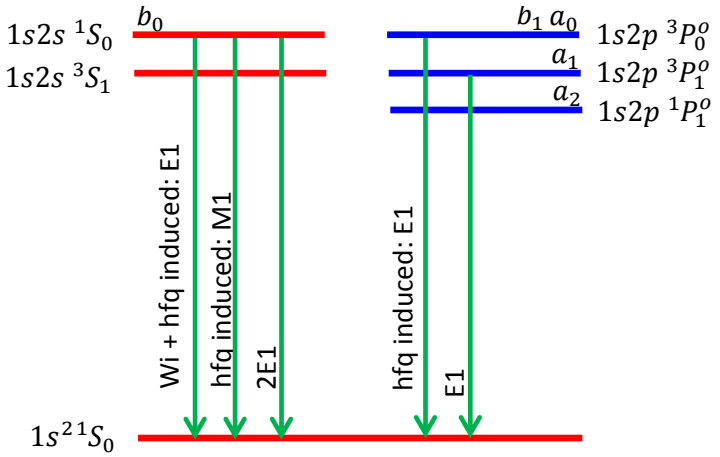

Figure 5.0.1: Schematic diagram of energy levels and transitions for a He-like ion.

- In the first process the $1s2s\ ^1S_0$ state is mixed with $1s2p\ ^3P_0^o$ due to weak interaction between the electrons and the nucleus.

$$\Psi\left(1s2s\ ^1S_0\right) = b_0\Psi\left(1s2s\ ^1S_0\right) + b_1\Psi\left(1s2p\ ^3P_0^o\right). \tag{5.0.1}$$

  The $1s2p\ ^3P_0^o$ state, in turn, is mixed with $1s2p\ ^3P_1^o$ and $1s2p\ ^1P_1^o$ due to the off-diagonal hyperfine interaction, opening the $1s2s\ ^1S_0 \rightarrow 1s^2\ ^1S_0$ E1

transition.

$$\Psi\left(1s2p\ ^3P_0^o\right) = a_0\Psi\left(1s2p\ ^3P_0^o\right) + a_1\Psi\left(1s2p\ ^3P_1^o\right) + a_2\Psi\left(1s2p\ ^1P_1^o\right); \quad (5.0.2)$$

- In the second process the $1s2s\ ^1S_0$ and $1s2s\ ^3S_1$ states are mixed due to the off-diagonal hyperfine interaction opening the $1s2s\ ^1S_0 \rightarrow 1s^2\ ^1S_0$ M1 transition. The latter transition has recently been studied by Li *et al.* [129];
- The third and the dominant $1s2s\ ^1S_0 \rightarrow 1s^2\ ^1S_0$ decay channel is the two-photon 2E1 transition. Properties of this transition are computed in [130].

The right hand side of the Figure 5.0.1 presents the allowed E1 transitions from $1s2p\ ^3P_1^o$ and $1s2p\ ^3P_1^o$:

- E1 transition due to the off-diagonal hyperfine interaction is not analysed.
- The line strengths of the last process E1 was computed to analyse the accuracy of the wave functions.

Relevant data for the combined weak and hyperfine interaction induced transition E1 $1s2s\ ^1S_0 \rightarrow 1s^2\ ^1S_0$ are however still insufficient and in response to this we have performed systematic calculations along the He-like isoelectronic sequence using the relativistic atomic structure package GRASP2K.

5.1 Atomic state expansions

For the generation of the MCDHF expansions (2.2.1) we used the active stets approach. The energy functional on which the orbitals were optimised is defined according to an EOL scheme, where a linear combination of 7 lowest atomic states was used. The combination included two even states with $J = 0$, one odd state with $J = 0$, two odd states with $J = 1$, one even state with $J = 1$ and one odd state with $J = 2$. CSFs were generated using active sets (AS) of orbitals. CSFs of the multiconfiguration calculations included single and double substitutions from the $1s$ shell. The ASs were labeled by a principal quantum number n and included s, p, d, f and g orbitals up to $n-1$. The active sets were extended to $n = 6$ for Z =6-61 and to $n = 5$ for Z =62-92 ions. At all steps only new orbitals are optimised.

Table 5.2.1: Transition energies (cm^{-1}) for ^{13}C and ^{149}Sm from calculations with increasing active sets, including Breit interaction. $\Delta E_1 = E\left(1s^2\ ^1S_0\right) - E\left(1s2s\ ^1S_0\right)$, $\Delta E_2 = E\left(1s2s\ ^1S_0\right) - E\left(1s2p\ ^3P_0^o\right)$ and $\Delta E_3 = E\left(1s2p\ ^3P_1^o\right) - E\left(1s2p\ ^3P_0^o\right)$. QED corrections were calculated using active spaces of CSFs formed by the AS_4.

As	CSFs	ΔE_1	ΔE_2	ΔE_3	ΔE_1	ΔE_2	ΔE_3
		^{13}C			^{149}Sm		
AS_2	7	−2439452	4300.3	−12.707	−326570125	−70225.5	−125804
AS_3	67	−2453255	1073.2	−12.422	−326591828	−77716.2	−125123
AS_4	187	−2454485	194.3	−12.312	−326596149	−79759.3	−124974
AS_5	397	−2454842	−3.0	−12.730	−326597470	−80513.8	−124930
AS_6	697	−2455131	−107.8	−12.620	−326599124	−81059.4	−124898
QED	187	184	19.2	0.200	471383	83651.8	−105
Total		−2454947	−88.6	−12.420	−326127741	2592.4	−125003
Ref.[131]		−2455167	−140.2	−12.488	−326137507	4973.3	−124809
Ref.[132]					−326136354	3645.0	−124910
Ex.[81]		−2455026	−144.4	−12.6			

5.2 Convergence of energy levels and transition data

Table 5.2.1 illustrates the convergence of the transition energies for $^{13}_{6}$C and $^{149}_{62}$Sm ions (transverse Breit interaction is included). As can be seen from the table, correlation effects have a huge impact on the results for $^{13}_{6}$C, but the QED contribution to the total value is very small (22% for ΔE_2) compared with the much heavier $^{149}_{62}$Sm (3 226% for ΔE_2). QED affects mostly the ΔE_2 transition. As can be seen from the table, results for $^{13}_{6}$C are in good agreement with NIST database recommended values [81].

Also, it should be mentioned, that for ions with Z =14, 26, 31, 37, 42, 45, 50, 54, 61-63, 91, and 92, Coulomb and Breit interactions give incorrect positions of excited levels (comparing with data from [131, 132]) and the order is restored only when QED effects are introduced. For ions $Z = 6$, 64, 65, 71, 77, and 90, correct order of excited levels was obtained when Breit interaction was included. Specific cases are ions with $Z = 9$ and $Z = 22$. In the first case the energy levels are in the correct order at Coulomb level, but order is incorrect at Breit level. The order is restored when QED effects are included. In the second case ($Z = 22$) the order is correct at Coloumb plus Breit level, and QED effects do not influence the order.

We also calculated the line strengths of the $1s2p\ ^3P_1^o \rightarrow 1s^2\ ^1S_0$ E1 transitions

Table 5.2.2: The wavelengths λ (Å) for the $1s2s\ ^1S_0 \rightarrow 1s^2\ ^1S_0$ E1 transition and line strengths S_{E1} (5.2.1) (a.u.) for the $1s2p\ ^3P_1^o \rightarrow 1s^2\ ^1S_0$ E1 transition of He-like ions.

	λ(Å)		S_{E1}	
^A_ZX	Our	Ref.[131, 132]	Our	Ref. [113]
$^{13}_{6}$C	40.728	40.730†	2.8909[-6]	2.8309[-6]
$^{19}_{9}$F	16.942	16.940†	1.3343[-5]	1.3219[-5]
$^{29}_{14}$Si	6.6851	6.6850	6.9859[-5]	6.9556[-5]
$^{47}_{22}$Ti	2.6226	2.6225	2.9941[-4]	2.9855[-4]
$^{57}_{26}$Fe	1.8594	1.8584	4.2208[-4]	4.2092[-4]
$^{71}_{31}$Ga	1.2950	1.2949	5.0259[-4]	5.0116[-4]
$^{85}_{37}$Rb	0.8995	0.8995	4.9500[-4]	4.9352[-4]
$^{97}_{42}$Mo	0.6923	0.6923	4.4597[-4]	4.4446[-4]
$^{103}_{45}$Rh	0.6001	0.6001	4.1101[-4]	4.0950[-4]
$^{117}_{50}$Sn	0.4820	0.4820	3.5342[-4]	3.5177[-4]
$^{131}_{54}$Xe	0.4104	0.4104	3.1152[-4]	3.0961[-4]
$^{145}_{61}$Pm	0.3174	0.3174	2.4924[-4]	2.4696[-4]
$^{149}_{62}$Sm	0.3066	0.3066	2.4187[-4]	2.3915[-4]
$^{151}_{63}$Eu	0.2964	0.2964	2.3441[-4]	2.3160[-4]
$^{155}_{64}$Gd	0.2866	0.2866	2.2689[-4]	2.2431[-4]
$^{159}_{65}$Tb	0.2773	0.2773	2.2037[-4]	2.1727[-4]
$^{175}_{71}$Lu	0.2294	0.2293	1.8383[-4]	1.7984[-4]
$^{193}_{77}$Ir	0.1922	0.1922	1.5345[-4]	1.4942[-4]
$^{229}_{90}$Th	0.1355	0.1355	1.0620[-4]	1.0088[-4]
$^{231}_{91}$Pa	0.1321	0.1321	1.0333[-4]	9.7885[-5]
$^{235}_{92}$U	0.1288	0.1288	1.0016[-4]	9.4994[-5]

† For calculations of the wavelengths the energy values of $\left(1s2s\ ^1S_0\right)$ and $\left(1s^2\ ^1S_0\right)$ states were used from [131].

in the Coulomb gauge (Table 5.2.2):

$$S_{E1} \;=\; \left|\left\langle \Psi\left(1s^2\ ^1S_0\right)||\hat{Q}^1||\Psi\left(1s2p\ ^3P_1^o\right)\right\rangle\right|^2. \tag{5.2.1}$$

Line strengths are compared with data from [113] and the difference is at most 5.5%. This shows that wave functions are appropriate for weak and hyperfine interaction calculations.

For the E1 transition $1s2s\ ^1S_0 \rightarrow 1s^2\ ^1S_0$, as mentioned above, the important mixing of $1s2p\ ^3P_0^o$ with $1s2p\ ^3P_1^o$ is due to off-diagonal hyperfine interaction and the mixing of $1s2s\ ^1S_0$ with $1s2p\ ^3P_0^o$ is due to weak interaction. Mixing coefficients a_1 and b_1 of these interactions are given by:

$$a_1 \;=\; \frac{\left\langle \Psi\left(1s2p\ ^3P_1^oF\right)|\hat{H}_{hfs}|\Psi\left(1s2p\ ^3P_0^oF\right)\right\rangle}{E\left(1s2p\ ^3P_0^o\right) \;-\; E\left(1s2p\ ^3P_1^o\right)}, \tag{5.2.2}$$

Table 5.2.3: Off-diagonal hyperfine interaction matrix elements $\left\langle|\hat{h}_{hfs}|\right\rangle_1$ (a.u.) and mixing coefficients (a_1 and a_1') (5.2.2) due to hyperfine interactions for He-like ions. For the calculations of a_1' the energy values of $\left(1s2p\ ^3P_0^o\right)$ and $\left(1s2p\ ^3P_1^o\right)$ states were used from [131, 132]. The values in brackets were calculated by direct diagonalization of the atomic Hamiltonian matrix.

				Mixing coefficients		
^A_ZX	I	μ_I	$\left\langle|\hat{h}_{hfs}|\right\rangle_1$	a_1	a_1'	Ref.[33]
$^{13}_{6}$C	1/2	0.7024	3.9931[-6]	0.68257[-1]	0.70176[-1]†	
					(0.69661[-1])	
$^{19}_{9}$F	1/2	2.6289	5.0943[-5]	-0.73246[-1]	-0.73905[-1]†	
					(-0.73308[-1])	
$^{29}_{14}$Si	1/2	-0.5553	-4.2065[-5]	0.51889[-2]	0.51959[-2]	
					(0.51957[-2])	
$^{47}_{22}$Ti	5/2	-0.7885	-1.7482[-4]	0.36554[-2]	0.36607[-2]	
					(0.36606[-2])	
$^{57}_{26}$Fe	1/2	0.0906	5.0963[-5]	-0.68638[-3]	-0.68734[-3]	
$^{71}_{31}$Ga	3/2	2.5623	1.9132[-3]	-0.19709[-1]	-0.19735[-1]	
$^{85}_{37}$Rb	5/2	1.3534	1.6521[-3]	-0.17996[-1]	-0.18021[-1]	
$^{97}_{42}$Mo	5/2	-0.9335	-1.7306[-3]	0.34071[-1]	0.34128[-1]	
$^{103}_{45}$Rh	1/2	-0.8840	-3.0208[-3]	0.39394	0.39577	
$^{117}_{50}$Sn	1/2	-1.0010	-4.8927[-3]	-0.49441[-1]	-0.49477[-1]	
$^{131}_{54}$Xe	3/2	0.6918	3.2932[-3]	0.15025[-1]	0.15037[-1]	
$^{145}_{61}$Pm	5/2	3.8000	2.5713[-2]	0.49751[-1]	0.49792[-1]	
$^{149}_{62}$Sm	7/2	-0.6677	-4.5978[-3]	-0.80723[-2]	-0.80787[-2]	
$^{151}_{63}$Eu	5/2	3.4717	2.6481[-2]	0.42363[-1]	0.42438[-1]	-0.424[-1]
$^{155}_{64}$Gd	3/2	-0.2572	-2.2708[-3]	-0.33223[-2]	-0.33247[-2]	0.335[-2]
					(-0.33246[-2])	
$^{159}_{65}$Tb	3/2	2.0140	1.8855[-2]	0.25311[-1]	0.25328[-1]	
$^{175}_{71}$Lu	7/2	2.2323	2.5881[-2]	0.21896[-1]	0.21913[-1]	
$^{193}_{77}$Ir	3/2	0.1637	3.0154[-3]	0.17182[-2]	0.17189[-2]	
$^{229}_{90}$Th	5/2	0.4600	1.5746[-2]	0.43361[-2]	0.43334[-2]	
$^{231}_{91}$Pa	3/2	2.0100	7.9272[-2]	0.20739[-1]	0.20721[-1]	
$^{235}_{92}$U	7/2	-0.3800	-1.3896[-2]	-0.34557[-2]	-0.34524[-2]	

† For calculations of the mixing coefficients the energy values of the $\left(1s2p\ ^3P_0^o\right)$ and $\left(1s2p\ ^3P_1^o\right)$ states were used from [131].

$$b_1 \;=\; \frac{\left\langle \Psi\left(1s2p\ ^3P_0^o\right)|\hat{H}_W|\Psi\left(1s2s\ ^1S_0\right)\right\rangle}{E\left(1s2s\ ^1S_0\right) \;-\; E\left(1s2p\ ^3P_0^o\right)}, \tag{5.2.3}$$

where $F = I$. The calculated off-diagonal hyperfine interaction matrix elements and corresponding mixing coefficients, with calculated energy values (a_1), and with energy values from [131, 132] (a_1').

Transition energies in the expressions above are calculated including Breit interaction and QED effects. For elements $^{13}_{6}$C, $^{19}_{9}$F, $^{29}_{14}$Si, $^{47}_{22}$Ti, and $^{155}_{64}$Gd the a_1 values were calculated by direct diagonalization of the full atomic Hamiltonian and are given in brackets. The differences between these hyperfine mixing

Table 5.2.4: The matrix element of the weak interaction operator $\left\langle|\hat{H}_W|\right\rangle$ ($i\frac{G_F}{2\sqrt{2}}Q_W$ a.u.), mixing coefficients (b_1 and b'_1) (5.2.3) due to weak interactions and transition rates A_1 (5.2.5) (s^{-1}) of the weak and hyperfine induced $1s2s\ ^1S_0 \rightarrow 1s^2\ ^1S_0$ E1 transitions for He-like ions. For calculation of b'_1 and the energy values of $\left(1s2s\ ^1S_0\right)$ and $\left(1s2p\ ^3P^o_0\right)$ states were used from [131, 132].

		Mixing coefficients			
^A_ZX	$\left\langle|\hat{H}_W|\right\rangle$	b_1/i	b'_1/i [131]	b'_1/i [132]	A_1
$^{13}_{6}$C	-1.0652[-1]	-0.79193[-11]	-0.72709[-11]		0.73669[-17]†
$^{19}_{9}$F	-6.4268[-1]	0.28717[-11]	0.31168[-11]		0.97443[-16]†
$^{29}_{14}$Si	-4.3718	0.10812[-10]	0.10838[-10]	0.10840[-10]	0.49881[-15]
$^{47}_{22}$Ti	-3.1642[1]	0.75766[-10]	0.75711[-10]	0.75772[-10]	0.86010[-12]
$^{57}_{26}$Fe	-6.7191[1]	0.16964[-9]	0.16915[-9]	0.16944[-9]	0.59978[-12]
$^{71}_{31}$Ga	-1.5201[2]	0.42552[-9]		0.42404[-9]	0.10916[-7]
$^{85}_{37}$Rb	-3.5815[2]	0.11571[-8]		0.11497[-8]	0.19659[-6]
$^{97}_{42}$Mo	-6.8249[2]	0.25753[-8]	0.25154[-8]	0.25463[-8]	0.68307[-5]
$^{103}_{45}$Rh	-9.8340[2]	0.41033[-8]		0.40403[-8]	0.32719[-2]
$^{117}_{50}$Sn	-1.7559[3]	0.99788[-8]	0.94384[-8]	0.97361[-8]	0.49228[-3]
$^{131}_{54}$Xe	-2.7352[3]	0.22861[-7]	0.20836[-7]	0.22047[-7]	0.33255[-3]
$^{145}_{61}$Pm	-5.7936[3]	0.18088[-6]		0.15324[-6]	0.30374
$^{149}_{62}$Sm	-6.4288[3]	0.35220[-6]	0.18356[-6]	0.25042[-6]	0.22931[-1]
$^{151}_{63}$Eu	-7.1369[3]	0.15427[-5]	0.31767[-6]	0.56727[-6]	0.34753[1]
$^{151}_{63}$Eu Ref. [33]			0.33[-6]		(0.11071[1])
$^{155}_{64}$Gd	-7.9123[3]	-0.93326[-6]	0.85603[-6]	-0.36479[-4]	0.94663[2]
$^{155}_{64}$Gd Ref.[33]			0.91[-6]		(0.52931[-1])
$^{159}_{65}$Tb	-8.7684[3]	-0.41622[-6]		-0.52707[-6]	0.12444[1]
$^{175}_{71}$Lu	-1.6195[4]	-0.17641[-6]		-0.19130[-6]	0.17694
$^{193}_{77}$Ir	-2.9673[4]	-0.20660[-6]		-0.20689[-6]	0.17985[-2]
$^{229}_{90}$Th	-1.1064[5]	-0.70008[-5]	0.32846[-4]	-0.51283[-5]	0.13538[2]
$^{231}_{91}$Pa	-1.2262[5]	0.52550[-5]		0.11262[-4]	0.15633[4]
$^{235}_{92}$U	-1.3575[5]	0.18517[-5]	0.14965[-5]	0.15020[-5]	0.80784

† For calculations of the mixing coefficients the energy values of the $\left(1s2s\ ^1S_0\right)$ and $\left(1s2p\ ^3P_0\right)$ stattes were used from [131].

coefficients and coefficients calculated with equation (5.2.2) are less than 1% and support the applicability of the perturbative expression. It should be mentioned that QED does not affect the ΔE_3 transition energy (up to 0.9%) and the a_1 mixing coefficient. The magnitude of the mixing coefficients for the $^{151}_{63}$Eu and $^{155}_{64}$Gd ions are in agreement with values from [33] (-4.24[-2] and 3.35[-3], respectively). The differences in sign are due to different definitions of the phase factor in the hyperfine interaction matrix element.

The calculated values of the weak interaction matrix element and corresponding mixing coefficients (b_1/i) are presented in the Table 5.2.4. Due to importance of QED effects for heavy ions [133], transition energies are taken from accurate calculations by Plante *et al.* [131], and Artemyev *et al.* [132]. The first author

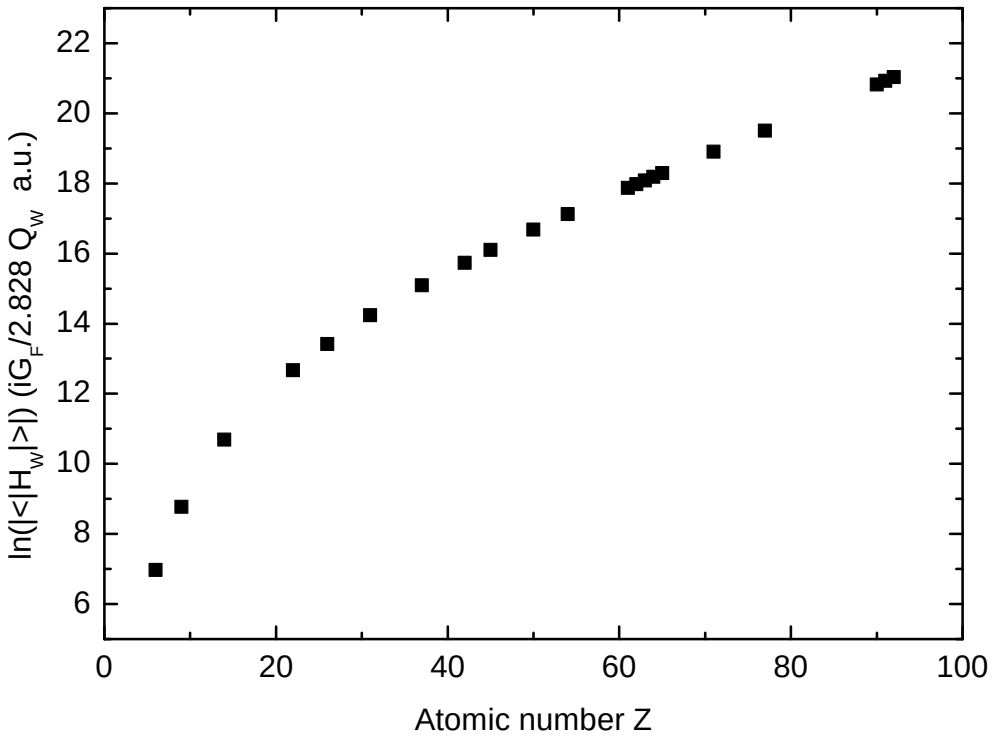

Figure 5.2.1: Z-dependence of weak interaction matrix element.

included QED effects of order $(Z\alpha)^3$ and some terms of $(Z\alpha)^4$, and the second author evaluated all terms through order $(Z\alpha)^4$.

Figure 5.2.1 displays dependence of weak interaction matrix element (Table 5.2.4, second column) on atomic number Z. The regression analysis yields the following relation:

$$\left\langle |\hat{H}_W| \right\rangle = [-1.2313(1) \cdot e^{0.1011(1)\cdot Z} + 1.02(2)] \cdot 10^6. \tag{5.2.4}$$

Compared with Plante *et al.* [131] and Artemyev *et al.* [132], our calculated QED contributions to the ΔE_2 transition energies are too large. For example, QED contribution for $^{117}_{50}$Sn in our calculation is 0.2059 a.u., as compared to 0.1818 a.u. [131] and 0.1845 a.u [132] (235%, 197% and 206% of the total transition energy, respectively). Another example is $^{229}_{90}$Th. For the ΔE_2 transition energy the contribution from QED in our calculation is 1.8573 a.u., as compared to 1.4259 a.u. [131] and 1.4651 a.u [132]. For $^{151}_{63}$Eu the QED contribution is 15528% of the total ΔE_2 transition energy. This means that QED effects not only change relative positions of levels, but also decrease transition energies and increase mixing coefficients of weak interaction (without QED b_1/i = -0.99347[-8]).

The values of b'_1/i for the $^{151}_{63}$Eu and $^{155}_{64}$Gd ions (0.31767[-6] and 0.85603[-6], respectively), have been calculated with the same energies as in [33, 131]. Using these energies there is a good agreement with the values (0.33[-6] and 0.91[-6]) given by Labzowsky [33]. This means that the calculated matrix element of weak interaction is very close to the one computed by us. However, results obtained with more accurate energy values [132] differ from the ones in [33].

Table 5.2.5: The matrix elements of off-diagonal hyperfine interaction $\left\langle|\hat{h}_{hfs}|\right\rangle_2$ (a.u.) and mixing coefficients (a_2 and a'_2) between the $1s2p\ ^3P^o_0$ and $1s2p\ ^1P^o_1$ states. For the calculations of a'_2 the energy values of the $\left(1s2p\ ^3P^o_0\right)$ and $\left(1s2p\ ^1P^o_1\right)$ states were used from [131, 132]. A_2 is the $1s2s\ ^1S_0 \rightarrow 1s^2\ ^1S_0$ transition rate (s^{-1}) calculated including the $1s2p\ ^3P^o_1$ and $1s2p\ ^1P^o_1$ states.

		Mixing coefficients		
^A_ZX	$\left\langle|\hat{h}_{hfs}|\right\rangle_2$	a_2	a'_2	A_2
$^{13}_{6}$C	2.8434[-6]	0.22113[-4]		0.74038[-17]
$^{19}_{9}$F	3.5348[-5]	0.15284[-3]	0.15341[-3]†	0.98688[-16]†
$^{29}_{14}$Si	-2.6400[-5]	-0.62824[-4]	-0.62788[-4]	0.51594[-15]
$^{47}_{22}$Ti	-7.6697[-5]	-0.87001[-4]	-0.86937[-4]	0.87039[-12]
$^{57}_{26}$Fe	1.7173[-5]	0.13411[-4]	0.13400[-4]	0.60210[-12]
$^{71}_{31}$Ga	4.4483[-4]	0.21480[-3]	0.21462[-3]	0.10923[-7]
$^{85}_{37}$Rb	2.4357[-4]	0.66409[-4]	-0.66357[-4]	0.19659[-6]
$^{97}_{42}$Mo	-1.7726[-4]	-0.30703[-4]	-0.30680[-4]	0.68307[-5]

† For calculations of the mixing coefficients the energy values of the $\left(1s2p\ ^3P^o_0\right)$ and $\left(1s2p\ ^1P^o_1\right)$ states were used from [131].

In Table 5.2.4 we display also the values of the weak and hyperfine interaction induced $1s2s\ ^1S_0 \rightarrow 1s^2\ ^1S_0$ E1 transitions rates:

$$A_{(Wi+hfq)E1}(1s2s\ ^1S_0 \rightarrow 1s^2\ ^1S_0)_{1,2} = \frac{2.02613\times10^{18}}{\lambda^3}(2F+1)\left\{\begin{array}{ccc} 0 & F & I \\ F & 1 & 1 \end{array}\right\}^2 a^2_{1,2}|b_1|^2 S_{E1}. \quad (5.2.5)$$

The agreement between our values (in parentheses) for the $^{151}_{63}$Eu and $^{155}_{64}$Gd ions and other theories [33] (1.1979 and 6.21075[-2], respectively) is very good, when the same energies as in reference [33] were used (see Table 5.2.4).

Due to strong hyperfine induced mixing between the $1s2p\ ^3P^o_0$ and $1s2p\ ^1P^o_1$ states for the low-Z ions [52], we also included the $1s2p\ ^1P^o_1$ state in the calcu-

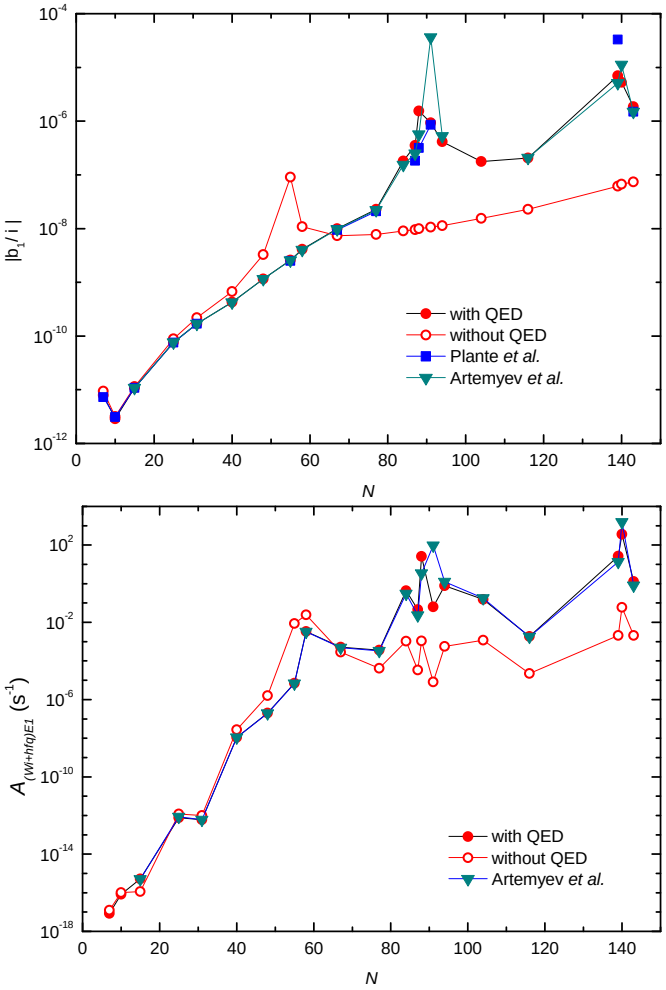

Figure 5.2.2: Dependence of mixing coefficient b_1/i (absolute value) and transition rates $A_{(Wi+hfq)E1}$ on number of neutrons (N). The results calculated using energies from references Plante *et al.* [131] (squares) and Artemyev *et al* [132] (triangles) are also presented.

lations. The mixing coefficient a_2 can be expressed as follow:

$$a_2 = \frac{\left\langle \Psi\left(1s2p\ ^1P_1^o F\right) |\hat{H}_{hfs}| \Psi\left(1s2p\ ^3P_0^o F\right)\right\rangle}{E\left(1s2p\ ^3P_0^o\right) - E\left(1s2p\ ^1P_1^o\right)}. \tag{5.2.6}$$

Off-diagonal hyperfine interaction matrix elements $\left\langle |h_{hfs}| \right\rangle_2$ (a. u.) and mixing coefficients (a_2) between the $1s2p\ ^3P_0^o$ and $1s2p\ ^1P_1^o$ states are given in Table 5.2.5. QED effects are insignificant for the $E\left(1s2p\ ^3P_0^o\right) - E\left(1s2p\ ^1P_1^o\right)$ transition energy and their influence on the mixing coefficients a_2 is less than 0.9%. Comparing transition rate A_1 (Table 5.2.4) with A_2 (Table 5.2.5), is clear that contribution of $1s2p\ ^1P_1^o$ state is quite small (up to 3%).

Table 5.2.6: Comparison of hyperfine induced M1 ($A_{(hfq)M1}$), weak and hyperfine induced E1 ($A_{(Wi+hfq)E1}$) and 2E1 (A_{2E1}) $1s2s\ ^1S_0 \to 1s^2\ ^1S_0$ transition rates (s^{-1}). For calculations of the transition rates of weak and hyperfine induced E1 transitions we used transition energies from [131, 132].

^A_ZX	$A_{(hfq)M1}$ [129]	$A_{(Wi+hfq)E1}$	A_{2E1} [130]
$^{13}_{6}$C	2.6534[-8]	0.74038[-17]	3.300[5]
$^{19}_{9}$F	1.0863[-4]	0.98688[-16]	5.029[6]
$^{29}_{14}$Si	2.4493[-4]	0.51594[-15]	8.685[7]
$^{47}_{22}$Ti	1.3010	0.87039[-12]	
$^{57}_{26}$Fe	3.8221[-1]	0.60210[-12]	
$^{71}_{31}$Ga	1.9926[3]	0.10923[-7]	
$^{85}_{37}$Rb	5.5705[3]	0.19659[-6]	
$^{97}_{42}$Mo	1.5643[4]	0.68307[-5]	
$^{103}_{45}$Rh	7.9312[4]	0.32719[-2]	1.154[11]
$^{117}_{50}$Sn	4.4904[5]	0.49228[-3]	2.164[11]
$^{131}_{54}$Xe	3.5483[5]	0.33255[-3]	3.415[11]
$^{145}_{61}$Pm	5.1405[7]†	0.30374	
$^{149}_{62}$Sm	1.8321[6]†	0.22931[-1]	
$^{151}_{63}$Eu	6.7643[7]	0.34753[1]	
$^{155}_{64}$Gd	5.5892[5]†	0.94664[2]	
$^{159}_{65}$Tb	1.4199[7]†	0.12444[1]	1.1013[12]
$^{175}_{71}$Lu	1.4508[8]	0.17694	
$^{193}_{77}$Ir	3.3463[6]	0.17985[-2]	
$^{229}_{90}$Th	1.7894[8]†	0.13538[2]	6.439[12]
$^{231}_{91}$Pa	4.7512[9]†	0.15633[4]	
$^{235}_{92}$U	1.5277[8]†	0.80784	7.265[12]

† These transition rates were deduced via scaling in Z [129].

Figure 5.2.2 reflects the importance of the QED effects to the b/i mixing coefficients and transition rates $A_1 = A_{(Wi+hfq)E1}$. Filled circles show results computed with QED, and empty circles — without QED. Also there are results calculated using energies from references [131] (squares) and [132] (triangles). QED effects of order $(Z\alpha)^4$ for elements $^{151}_{63}$Eu, $^{155}_{64}$Gd, and $^{231}_{91}$Pa are important for the mixing coefficients of weak interaction and transition rates A_1. Mixing coefficients b_1/i of weak interaction calculated without QED agree only at beginning of the isoelectronic sequence ($Z = 6$, 9, 14, 22, and 26).

Table 5.2.6 lists E1 $1s2s\ ^1S_0 \to 1s^2\ ^1S_0$ transition rates ($A_{(Wi+hfq)E1}$) arising from weak and off-diagonal hyperfine interactions. $A_{(Wi+hfq)E1}$ are compared with transition rates of other $1s2s\ ^1S_0 \to 1s^2\ ^1S_0$ decay channels: hyperfine induced magnetic dipole transition rates M1 ($A_{(hfq)M1}$) and rates of two-photon electric dipole decay 2E1 (A_{2E1}).

5.3 Conclusions

To sum up, we have calculated weak and hyperfine interaction induced $1s2s\ ^1S_0 \rightarrow 1s^2\ ^1S_0$ E1 transition rates for the isoelectronic sequence of He-like ions using the multiconfiguration Dirac-Hartree-Fock and relativistic configuration interaction methods. The comparison of the A_1 transition rates with the rates from other decay channels is presented in Table 5.2.6. The calculated values differ with respect to previous calculations [33] for the $^{151}_{63}$Eu and $^{155}_{64}$Gd ions due to importance of higher-order QED effects. Results demonstrated that $^{151}_{63}$Eu, $^{155}_{64}$Gd, $^{229}_{90}$Th and $^{231}_{91}$Pa He-like ions are the most promising species for future experiments due to very large values of the transition rates.

Chapter 6

Theoretical investigations of electric dipole moments [A6]

In the present work we computed the EDMs in the ground states of three diamagnetic atoms, ^{225}Ra, ^{199}Hg, and ^{171}Yb. The purpose of the present work is fourfold. Firstly, we tested the newly developed programs to evaluate matrix elements of P,T-odd e-N tensor-pseudotensor (TPT) and pseudoscalar-scalar (PSS) interactions, the atomic electric dipole moment, the nuclear Schiff moment (NSM), and the interaction of the electron electric dipole moment (eEDM) with nuclear magnetic moments. Secondly, we generated the atomic wave functions in several different approaches, in order to test the dependence of the calculated atomic EDMs on options available in the GRASP2K implementation of the MCDHF method. The approaches depended on the choice of variational energy functional see section 2.2.1 (Average Level versus Optimal Level, with different numbers of optimised levels), the choice of wave functions built on a common orbital set or several separately optimised orbital sets, (in the latter case biorthogonal transformations of wave functions had to be applied (section 2.2.5)), as well as on specific methods of one-electron orbital generation. All results of these approaches are discussed in more detail in sections 6.1, 6.2, and 6.3 and presented in Tables 6.2.1, 6.4.1, and 6.5.1. Thirdly, we sequentially generated several layers of virtual (correlation) orbitals for each of the three elements and observed the effects of electron correlation on atomic EDMs. All valence and core-valence electron correlation effects were included through single and restricted double electron substitutions from core and valence shells to virtual orbitals. And finally, we provide independently calculated atomic EDMs in the $J=0$ ground states of ^{225}Ra, ^{199}Hg, and ^{171}Yb, and compare our results with those of other authors. Our results, presented in the Tables 6.7.1, 6.7.2, 6.7.3, and 6.7.4, were obtained within the MCDHF method, using the relativistic atomic structure package GRASP2K [43], which, to the best of our knowledge,

and with the exception of one paper [134] on the Schiff moment in radium, has been employed for the first time in the calculations of matrix elements of P,T-odd e-N tensor-pseudotensor and pseudoscalar-scalar interactions, nuclear Schiff moment, and interaction of electron electric dipole moment with nuclear magnetic moments. (Preliminary results of these calculations were presented in [A8].)

The three atoms ^{225}Ra, ^{199}Hg, and ^{171}Yb, have been chosen on the grounds that they have similar valence shell structure. All these elements are diamagnetic, with closed outer s shell (^{225}Ra $6p^6 7s^2$, ^{199}Hg $5d^{10}6s^2$, and ^{171}Yb $4f^{14}6s^2$). In the future we will be able to extend these calculations to closed-p-valence-shell atoms, as well as to any other, closed- or open-shell system.

6.1 Virtual orbital sets

The numerical wave functions were obtained independently for the two parities. The calculations proceeded in two phases. Spectroscopic (occupied) orbitals were obtained in the Dirac-Hartree-Fock approximation. They were kept frozen in all subsequent calculations. Then virtual (correlation) orbitals were generated in several consecutive steps. At each step the virtual set has been extended by one layer of virtual orbitals. A *layer* is defined as a subset of virtual orbitals, usually with different angular symmetries, optimised simultaneously in one step, and usually frozen in all subsequent steps. In the present work up to five layers of virtual orbitals of each of the s,p,d,f,g symmetries were generated. At each stage only the outermost layer is optimised and the remaining orbitals (spectroscopic as well as other virtual layers) are kept frozen. Virtual orbitals were generated in an approximation in which all single and restricted double substitutions from valence orbitals and a subset of core orbitals to subsequent layers of virtual orbitals were included. The restriction was applied to double substitutions in the same manner as in SD V+C+CV strategy of Er^{3+} ground state computation (see section 4.1). The valence shells is $7s$ for even parity ground state, $7s$ and $7p$ for odd parity excited states of radium, $6s$ and $6p$ in the cases of mercury and ytterbium. Five layers of virtual orbitals were generated for Hg, and four layers for Ra and Yb. The combined contribution of the $n = 3$ shells to the hyperfine constants of the $7s7p\ ^1P$ state was evaluated in paper [135] and found to be negligible, while the combined contribution of the $n = 4$ shells was below 1 percent level. Therefore in the present calculations the innermost core

orbitals $1s$, $2s$, $2p$, $3s$, $3p$, $3d$ of the radium atom were kept closed for electron substitutions. All other core orbitals, as well as valence orbitals, were subject to electron substitutions. By similar argument, the innermost core orbitals $1s$, $2s$, $2p$ of Hg and Yb were kept closed for electron substitutions.

6.2 Non-orthogonal orbital sets

The matrix elements of all interactions were calculated between the ground state ns^2 ($J = 0$) and excited states with total angular momentum $J = 1$ and opposite parity for ^{225}Ra, ^{199}Hg, and ^{171}Yb. The optimal wave functions for calculations of EDM matrix elements were obtained in the Extended Optimal Level form (see section 2.2.1 above), separately for each parity. The wave functions optimised separately for the ground and excited states are built from independent sets of one-electron orbitals. The two sets are mutually non-orthogonal and they automatically account for relaxation effects involved in calculations of matrix elements between different atomic states [134, 137]. On the other hand, the transition energies obtained from wave functions based on separately optimised orbital sets may be less accurate than transition energies obtained from calculations based on a common set of mutually orthogonal one-electron orbitals. The above situation often arises when multiconfiguration expansions are tailored specifically to include only those electron correlation effects that are important for one-electron expectation values. For one-electron matrix elements involved in the present calculations the dominant contributions arise from single and restricted double substitutions. We have not included the unrestricted double substitutions, i.e. the electron correlation effects with dominant contributions to the total energy, as well as higher order substitutions, since their impact on EDMs is indirect and usually small [138].

We evaluated the effect of the relaxation of the wave functions by performing two parallel sets of calculations based on a common orbital set (orthogonal) and on two separately optimised orbital sets (non-orthogonal), respectively. Table 6.2.1 lists the atomic EDM for ^{225}Ra, calculated in several approximations. The first line (denoted DF in the first column) lists the results obtained with uncorrelated Dirac-Fock wave functions. The following lines provide the results obtained with different numbers (1-4) of virtual orbital layers included in the Virtual Orbital Set (VOS). The number of virtual orbital layers in a given VOS is quoted in the first column. We skipped the 'orthogonal' calculation with four

Table 6.2.1: Contributions to the atomic EDM from TPT, PSS, NSM, and eEDM interactions, calculated for ^{225}Ra, using orthogonal (Orth) and non-orthogonal (Non-O) orbital sets. The number VOS in the first column is the number of virtual orbital layers. Transition energies are experimental.

	TPT		PSS		NSM		eEDM	
VOS	Orth	Non-O	Orth	Non-O	Orth	Non-O	Orth	Non-O
DF	−16.3	−15.81	−59.7	−57.87	−6.53	−6.32	−55.6	−46.67
1	−14.5	−15.51	−53.3	−57.09	−6.28	−7.01	−48.1	−43.69
2	−18.8	−19.90	−69.0	−72.95	−7.79	−8.16	−63.5	−58.07
3	−19.9	−20.68	−70.3	−75.83	−8.27	−8.59	−66.9	−60.13
4		−20.28		−74.42		−8.63		−58.45

virtual orbital layers, since the preceding lines show clearly that the effects of non-orthogonality (i.e. the relaxation of wave functions) are of the order of a few percent, up to 11% for the interaction of the electron electric dipole moment with the nuclear magnetic field (eEDM entry in Table 6.2.1).

The calculation of matrix elements in the non-orthogonal case requires a bi-orthogonal transformation of one-electron orbitals, described in the section 2.2.5.

6.3 Extended Optimal Level calculations

The final values of atomic EDMs, presented in the Tables 6.7.1, 6.7.2, 6.7.3, and 6.7.4, were obtained with the Extended Optimal Level optimisation procedure described in section 2.2.1 above. At each stage of generation of virtual orbital sets, a decision had to be made with respect to the number of atomic levels included in the variational energy functional. Table 6.4.1 presents the contributions d_{at}^{TPT} to the atomic EDM of ^{225}Ra from the tensor-pseudotensor interaction (2.1.17). The contributions from particular atomic states are listed in subsequent lines. The radial wave functions were optimised within the EOL procedure, with different numbers of EOL levels: 4, 6, 8, 10, or 12 levels, as indicated in the first line of the Table 6.4.1. These data were obtained with experimental transition energies quoted from the NIST database [81].

An inspection of the Table 6.4.1 (the last line, denoted 'Sum All') indicates that the d_{at}^{TPT} expectation value becomes stable when eight or more levels are included in the Extended Optimal Level energy functional. Analogous decisions were made for all virtual orbital sets, as well as for the other two elements. The final calculations were made with varying numbers of EOL levels, between

2 levels for uncorrelated Dirac-Fock wave functions, with 6-8 levels in most correlated calculations, and up to 13 levels in one case.

6.4 Orbital contributions

Another interesting conclusion arises from the analysis of contributions of particular one-electron orbitals generated in the EOL optimisation procedure. The analysis presented in the Table 6.4.1 was made with only one virtual orbital layer, because the Extended Optimal Level optimisation procedure described in section 2.2.1 above becomes unstable with the increasing numbers of virtual layers and of EOL levels. However, already at this level of approximation the dominant contributions come from the singlet $7s7p\ ^1P_1$ and triplet $7s7p\ ^3P_1$ excited states. The states $7s8p\ ^1P_1$ and $7s8p\ ^3P_1$, involving $8p$ orbital, contribute 9% and 3%, respectively (and their contributions partially cancel due to different signs). All other states contribute less than one percent each. The following lines present contributions of singlet and triplet states generated by single or double electron substitutions from the reference configuration $7s7p$ to the lowest available orbitals $8s$, $8p$, and $6d$. The line denoted 'Sum s-p' shows the contributions of the four dominant states generated by single electron substitutions from the reference configuration. The line denoted 'Sum s-d' shows the sum of entries from the preceding two lines of the $6d7p$ configuration; the line 's-p+s-d' shows the sum of all preceding contributions. The next six lines present the contributions of higher lying levels, and the line 'Sum D' shows the sum of the contributions from these six preceding lines. The last line 'Sum All' shows the total sum of all contributions of all states listed in the preceding lines. We present the partial sums ('s-p', 's-d', 's-p+s-d', and 'Sum D') to show their dependence on the number of EOL levels. The contributions of individual levels are not very stable, and in particular the small contributions may vary significantly, but the partial sums are more stable, and the total sum ('Sum All') is strongly stabilized by the contributions from the dominant states.

It is interesting to make a comparison of Table 6.4.1 with Table VI from reference [139]. In the reference [139] the contributions from $7s_{1/2} - 7p_{1/2}$ and $7s_{1/2} - 8p_{1/2}$ single-particle matrix elements (pairings in their language) are of comparable sizes, -324.468 and -306.133, respectively, while in our calculations the relative sizes of the contributions from $7s_{1/2} - 8p_{1/2}$, with respect to the contribution from $7s_{1/2} - 7p_{1/2}$ pairing, are 9% and 3% for singlet and triplet

Table 6.4.1: d_{at}^{TPT} contribution to atomic EDM, calculated with the EOL method for the 1st VOS, using different numbers of optimised levels and experimental transition energies, in units $\left(10^{-20} C_T \langle \boldsymbol{\sigma}_A \rangle |e| \,\mathrm{cm}\right)$, for ^{225}Ra. Numbers in brackets represent powers of ten.

Levels	4	6	8	10	12
$7s7p\ ^3P$	−5.00	−4.46	−4.63	−4.59	−4.63
$7s7p\ ^1P$	−1.03[1]	−8.80	−8.70	−8.69	−8.57
$7s8p\ ^3P$		0.39	0.30	0.33	0.44
$7s8p\ ^1P$		−1.12	−0.96	−1.01	−1.24
Sum s-p	−1.53[1]	−1.40[1]	−1.40[1]	−1.40[1]	−1.40[1]
$6d7p\ ^3D$	2.53[−3]	−7.72[−4]	2.96[−2]	−9.30[−2]	−6.91[−2]
$6d7p\ ^3P$	1.98[−1]	−3.08[−2]	−1.13[−1]	3.55[−2]	7.34[−2]
Sum s-d	2.00[−1]	−3.16[−2]	−8.33[−2]	−5.75[−2]	4.25[−3]
s-p+s-d	−1.51[1]	−1.40[1]	−1.41[1]	−1.41[1]	−1.40[1]
$6d8p\ ^3D$			−4.79[−2]	−9.44[−3]	−3.63[−3]
$6d8p\ ^3P$			−1.15[−1]	−4.90[−2]	−8.36[−2]
$7p8s\ ^3P$				−1.96[−2]	−2.20[−2]
$7p8s\ ^1P$				−6.02[−3]	−6.31[−3]
$6d7p\ ^1P$					−5.12[−3]
$8s8p\ ^3P$					1.50[−3]
Sum D			−1.63[-1]	−8.41[−2]	−1.19[−1]
Sum All	−1.51[1]	-1.40[1]	−1.42[1]	−1.41[1]	−1.41[1]

states, respectively. Also, there are differences with respect to the contributions of higher symmetry orbitals. For instance, the contribution from $d_{5/2}$ orbitals is of the order of 4% (see TABLE VII in reference [139]), while in our calculations the contributions from $d_{5/2}$ orbitals are below 1%.

It is difficult to explain these differences, but one possible explanation is due to differences in optimisation procedures and radial shapes of one-electron orbitals which resulted from these procedures, as discussed in the section 2.2.1. Different compositions of particular atomic states are likely consequences of differences in radial bases. The authors of the reference [139] used Gaussian basis sets, while in our calculations we use numerical orbitals defined on a grid. We do not have insight into the details of the calculations presented in the reference [139], but their Gaussians are likely to be evenly distributed over the entire configurational space.

Different theories use different methods of construction for atomic states. A consequence of these differences is the fact, that comparisons of contributions from particular atomic states or from individual one-electron orbitals are not meaningful. All excited and virtual orbitals generated in our calculations were optimised with multiconfiguration expansions designed for valence and core-

valence electron correlation effects, resulting in virtual orbital shapes with maximal overlaps with valence and outer core spectroscopic orbitals. Consequently, the correlation corrections to the wave function are likely to be larger for the lower states included in the Extended Optimal Level procedure. We performed comparison calculations with virtual orbitals generated with three different methods: the Extended Average Level procedure, as described in the section 2.2.1; with virtual orbitals generated within the screened hydrogenic approximation; and virtual orbitals from Thomas-Fermi potential. As described in the section 2.2.1, one-electron virtual orbitals generated with the EAL functional are optimised to minimise the sum of energies of all states. Hydrogenic and Thomas-Fermi virtual orbitals are not variationally optimised, they just form orthogonal bases. Our comparison calculations indicate, that calculations based on Extended Average Level, hydrogenic, and Thomas-Fermi virtual orbitals converge slower than Extended Optimal Level calculations, and the contributions of higher lying levels are larger, compared to EOL results.

6.5 Transition energies

The summation in equation (2.3.8) runs over all excited states of appropriate parity and symmetry. The contributions of higher lying levels are gradually decreasing, since they are suppressed both by the energy denominators, by decreasing values of electric dipole matrix elements, as well as by decreasing overlaps of one-electron radial orbitals, entering integrals in the equations: (2.1.19), (2.1.25), (2.3.15), and (2.3.13). In numerical calculations they have to be cut off at certain level of accuracy. Except where indicated otherwise, the results presented in the present work were computed with experimental transition energies in the denominators of the matrix elements in equation (2.3.8). The transition energies were calculated from the NIST database [81] and we included levels up to $6d7p\ ^3P$ for ^{225}Ra, $6s8p\ ^1P$ for ^{171}Yb, and $6s9p\ ^1P$ for ^{199}Hg. However, several levels are missing in [81], so we employed an approach, where those transition energies which were not available, were replaced by the energies calculated with one of the three different methods: (1) using theoretical energies obtained from MCDHF approach; (2) with the energy of the upper level replaced by the energy of the lowest excited state; (3) with the energy of the upper level replaced by the experimental ionization limit. The choice was made between the above three options in case of each missing level, based on availability of a reliable theoretical

energy, or alternatively on the proximity of the lowest excited state or the experimental ionization limit. To verify this approach we performed test calculations, where all three choices were used together. Table 6.5.1 presents the contributions from the tensor-pseudotensor interaction to the atomic EDM of radium isotope ^{225}Ra. Transition energies in Table 6.5.1 were taken from: MCDHF RSCF calculation (RSCF), MCDHF RCI calculation (RCI), experimental data (Expt.), experimental ionization limit (Expt. IL), experimental energy of the lowest excited level (Expt. 1). The MCDHF RSCF case was a self-consistent-field Extended Optimal Level calculation, with 2, 6, 8 and 6 EOL levels for DF, 1, 2, 3 and 4 VOS, respectively. The MCDHF RCI case was a configuration-interaction calculation with 100 levels included. Their differences indicate the deviation incurred when the number of EOL levels is varied. It should be noted that available experimental values of the energies of the $7s7p$ levels were used in all cases in columns 'Expt.', 'Expt. IL', and 'Expt. 1'. The lowest $nsnp$ levels yield the largest contributions to all EDM matrix elements in the present calculations, and their energies are available for all elements in question, therefore replacements were made only for higher lying levels. The number VOS in the first column of Table 6.5.1 represents the number of virtual orbital layers. These data indicate the sizes of errors, which may arise from replacing experimental transition energies with experimental ionization limit (Expt. IL) or experimental energy of the lowest excited level (Expt. 1). As can be seen, the deviation is less than 10% in case of radium. The deviations of the data obtained with calculated transition energies are larger, due to the nature of the wave functions built from non-orthogonal orbital sets, as explained in the section 6.2 above.

6.6 Summation over excited states

As mentioned in the section 6.5 above, the summation in equation (2.3.8) runs over all excited states of appropriate parity and symmetry. In numerical calculations the summation had to be truncated at finite number of terms, and in the present up to five terms of each symmetry were explicitly evaluated. The contribution of the remaining part of the sum may be estimated by extrapolation. Let us consider, as an example, the contributions from the Rydberg series of the triplet states $6snp\ ^3P_1$ of ^{199}Hg. After explicit, numerical calculation of large contributions arising from low values of principal quantum number n, the contributions of higher lying states entering the sum in equation (2.3.8) may be

Table 6.5.1: Tensor-pseudotensor interaction contributions to EDM, for ^{225}Ra, in units $\left(10^{-20} C_T \langle \boldsymbol{\sigma}_A \rangle |e| \,\mathrm{cm}\right)$, calculated with the EOL method and compared with data from other methods. Transition energies taken from: MCDHF-RSCF calculation (RSCF), experimental data (Expt.), MCDHF-RCI calculation (RCI), experimental ionization limit (Expt. IL), experimental value of lowest excited level (Exp. 1). (see text for explanation). The number VOS in the first column is the number of virtual orbital layers.

	^{225}Ra				
VOS	RSCF	RCI	Expt.	Expt. IL	Expt. 1
DF	−18.31	−18.31	−15.81	−15.81	−15.81
1	−10.37	−11.81	−15.51	−14.70	−13.92
2	−12.04	−12.58	−19.90	−20.08	−20.45
3			−20.68	−21.22	−22.52
4			−20.28	−21.16	−22.32
Ref. [37](DHF)					−3.5
Ref. [37](CI+MBPT)					−17.6
Ref. [37](RPA)					−16.7
Ref. [139](CPHF)					−16.585

evaluated from the asymptotic behaviour of the matrix elements in the numerator and of the transition energy in the denominator. The electric dipole matrix element scales with principal quantum number n as [51, 140]:

$$(E_0 - E_n) \left| \left\langle 0 | \hat{D}_z | 6snp\, ^3P_1 \right\rangle \right|^2 \sim (n^*)^{-3}, \tag{6.6.1}$$

where n^* is the effective quantum number of the running np electron in the series $6snp\, ^3P_1$, i.e. $n^* = (n - \delta)$, δ being the quantum defect (for the series $6snp\, ^3P_1$ of ^{199}Hg the quantum defect $\delta = 4.293$). The calculations of the matrix elements of the P,T-odd interactions involve radial integrals of atomic one-electron orbitals, and all these integrals include factors in the integrands, which effectively cut off the integrals outside the nucleus (see equations (2.1.19), (2.1.25), (2.3.15), and (2.3.13)). Therefore the dominant contribution to each integral comes from within or in the vicinity of the nucleus. Dirac equation near the origin has power series solution, and the n-dependence near the origin is as follows [1, 29, 35]:

$$P(r) \sim (n^*)^{-3/2}, \tag{6.6.2}$$

$$Q(r) \sim (n^*)^{-3/2}, \tag{6.6.3}$$

where $P(r)$ and $Q(r)$ are large and small components of radial wave functions, respectively. The Figure 6.6.1 shows the numerical large components $P(r)$ of the one-electron np radial orbitals, in the vicinity of the nucleus, for $n = 6, 7, 8, 9$, ex-

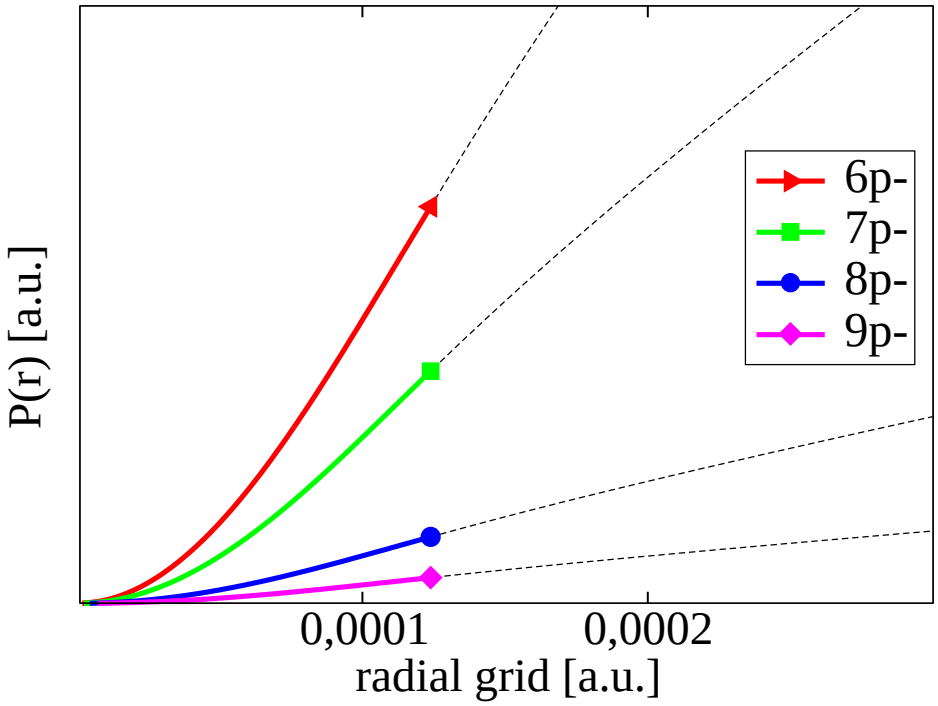

Figure 6.6.1: Large components $P(r)$ of the one-electron np radial orbitals of the triplet states $6snp\ ^3P_1$ ($n = 6,7,8,9$) of ^{199}Hg. The solid line sections represent the radial shapes of the orbitals inside the ^{199}Hg nucleus. $P(r)$ in arbitrary units, radial grid in atomic units. See text for further details.

tracted from the triplet states $6snp\ ^3P_1$ in ^{199}Hg. The solid line sections represent the radial shapes of the orbitals inside the ^{199}Hg nucleus. The solid line sections of these components are monotonic and they scale with n^* approximately as in the equation (6.6.2). The small components $Q(r)$ scale similarly. (In the vicinity of the nucleus the amplitudes of the 'small' components are large compared to the amplitudes of the 'large' components). Therefore the integrands in the matrix elements of the P,T-odd interactions considered in this work also scale with n^* of the running np electron as

$$\left\langle 6snp\,^3P_1 \middle| \hat{H}_{int} \middle| 0 \right\rangle \sim (n^*)^{-3/2}. \tag{6.6.4}$$

The energy denominator in the equation (2.3.8) saturates at the ionisation energy for large n values along the Rydberg series, therefore the overall n-dependence of subsequent terms in the sum in equation (2.3.8) involves a product of right-hand sides of the equations (6.6.1) and (6.6.4), which together yield the

contribution from a particular $6snp\ ^3P_1$ state $d_{at}^{int}(6snp\,^3P_1) \sim (n^*)^{-3}$. Eventually, the infinite sum in the equation (2.3.8) may be evaluated in the following way. The first four terms were explicitly calculated from the numerical wave functions. The upper bound on the remaining terms was approximately evaluated by Riemann zeta function. The relative correction i.e. the contribution from the trailing terms (called Riemann zeta tail) divided by the contribution from the four leading terms, is of the order of 1.5 percent, again with the assumption that the energy denominators saturated at the ionisation energy. With the above assumption lifted, the relative correction would be smaller than 1.5%, since the presence of the energy denominators increases the relative weights of the leading terms. The matrix elements in equations (6.6.1) and (6.6.4) can be either positive or negative and not infrequently change sign partway up a series. Sign changes would of course decrease the relative correction mentioned above.

In order to validate the above reasoning we performed a separate calculation for ^{199}Hg, where singlet $6snp\ ^1P_1$ and triplet $6snp\ ^3P_1$ states of ^{199}Hg were separately generated for $n = 6,7,8,9,10$. Let us consider the contribution $d_{at}^{TPT}(6snp\,^3P_1)$ to the total atomic EDM from the individual $6snp\ ^3P_1$ triplet state, i.e. from one term of the sum on the right hand side of the equation (2.3.8). When both sides of this equation are multiplied by the energy denominator, what remains on the right hand side scales with $(n^*)^{-3}$ of the running np electron:

$$d_{at}^{TPT}(6snp\,^3P_1)(E_0-E_n)^{3/2} \quad = \\ 2\left\langle 0|\hat{D}_z|6snp\,^3P_1\right\rangle \left\langle 6snp\,^3P_1|\hat{H}_{TPT}|0\right\rangle \sim (n^*)^{-3} \qquad (6.6.5)$$

The Figure 6.6.2 shows the relation (6.6.5) in log-log coordinates obtained for the triplet $6snp\ ^3P_1$ and the singlet $6snp\ ^1P_1$ ($n = 6,7,8,9,10$) states of ^{199}Hg. The straight line linear fits yield the slope -4.6 for the triplet $6snp\ ^3P_1$ state (solid line, circles, blue color), and -7.3 for the singlet $6snp\ ^1P_1$ state (dashed line, squares, red color). Both slope values should be compared to -3.0 obtained from the considerations presented in the previous paragraphs. Analogous linear fits for other Rydberg series of all three elements, ^{225}Ra, ^{199}Hg, and ^{171}Yb, and for all four P,T-odd interactions, yield the slopes in the range -3.9 -:- -9.1. The singlet series exhibit larger slope values, compared to triplet series. The large values of slope values, the large range of slope values, as well as noticeable deviations from linear fits, reflect the fact that the slopes are fitted to the

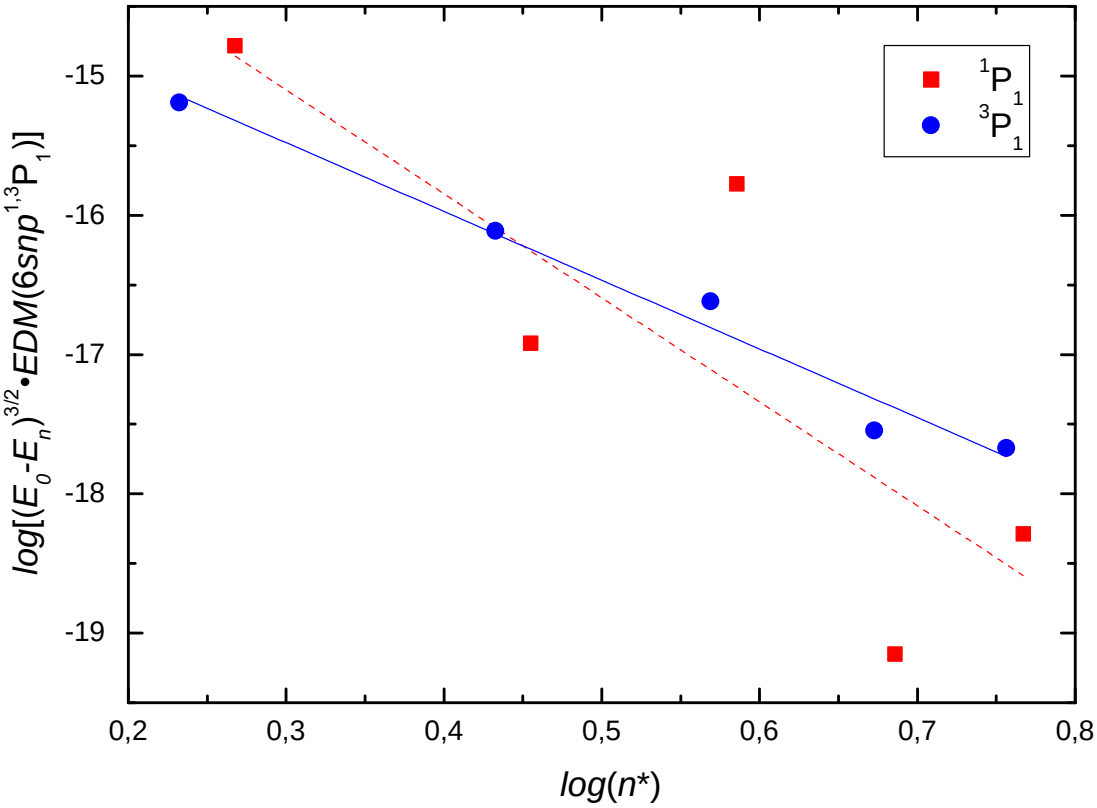

Figure 6.6.2: Tensor-pseudotensor interaction contributions to EDM in ^{199}Hg, multiplied by the energy denominators, as a function of the effective quantum number n^* of the np orbitals ($n = 6, 7, 8, 9, 10$) from the triplet $6snp\ ^3P_1$ (solid line, circles, blue color) and the singlet $6snp\ ^1P_1$ (dashed line, squares, red color) individual states of ^{199}Hg. See text for further details.

calculated data obtained from the leading terms in the equation (2.3.8), corresponding to the lowest atomic levels of a particular Rydberg series. The lowest levels of a Rydberg series are not truly 'Rydberg', in the sense that the valence electrons are not yet completely screened by the electronic core, and they exhibit strong deviations from Rydberg regularities, due to interelectronic interactions.

Eventually, the upper bounds on the trailing terms in all cases were evaluated by partial summation of Riemann zeta function. Based on these analyses, we concluded that the first four terms of each Rydberg series in the equation (2.3.8) yield 98 percent or more of the series' contribution to the total atomic EDMs of all three elements, ^{225}Ra, ^{199}Hg, and ^{171}Yb, and for all four P,T-odd interactions.

6.7 Uncertainty estimates

Estimates of uncertainty in *ab initio* calculations are far more difficult and uncertain than the calculations themselves, particularly in situations, where an atomic property is evaluated, which has not been calculated before within the same approach for any other element. We can indicate possible sources of uncertainties, but their sizes are difficult to estimate. The possible sources of uncertainties are the following.

Table 6.7.1: Tensor-pseudotensor interaction contributions to EDM, calculated with the EOL method in different virtual sets, in units $\left(10^{-20} C_T \langle \boldsymbol{\sigma}_A \rangle |e| \,\mathrm{cm}\right)$, for ^{225}Ra, ^{199}Hg, and ^{171}Yb, compared with data from other methods.

	^{225}Ra			^{199}Hg	^{171}Yb
VOS	Expt.	Expt. IL	Expt. 1	Expt.	Expt.
DF	−15.81	−15.81	−15.81	−6.15	−3.31
1	−15.51	−14.70	−13.92	−4.86	−1.94
2	−19.90	−20.08	−20.45	−5.70	−3.71
3	−20.68	−21.22	−22.52	−6.10	−4.03
4	−20.28	−21.16	−22.32	−5.53	−4.24
Ref. [37](DHF)	−3.5			−2.4	−0.70
Ref. [141](DHF)				−2.0	
Ref. [37](CI+MBPT)	−17.6			−5.12	−3.70
Ref. [37](RPA)	−16.7			−5.89	−3.37
Ref. [141](RPA)				−6.0	
Ref. [142](RPA)				−6.75	
Ref. [139](CPHF)	−16.585				−3.377
Ref. [143](CCSD)				−4.3	

6.7.1 Electron correlation effects

In extensive, large-scale calculations the relative accuracy can reach 1-5 percent, depending on the expectation value in question (see eg. [135, 136]). An estimate of uncertainty associated with the electron correlation effects can be obtained in several ways. In the limit of very large number of virtual orbital layers an estimate of uncertainty may be related to oscillations of the calculated expectation value plotted as a function of the size of the multiconfiguration expansion [136]. In the present work an estimate of the uncertainty was based on the differences between the data obtained with the largest two multiconfiguration expansions, represented by 3 and 4 layers of virtual orbitals in Tables 6.7.1, 6.7.2, 6.7.3, and 6.7.4. We abstained from extending the virtual sets beyond fourth layer, because there are several other possible sources of uncertainty in the present calculations.

An inspection of the Tables indicates that the differences between the last two lines range between 0.47% for the Schiff moment of Ra, and 15.77% for the Schiff moment of Hg (Table 6.7.3). We may assume the latter as an estimate of uncertainty associated with the neglected electron correlation effects.

Table 6.7.2: Pseudoscalar-scalar interaction contributions to EDM, calculated with the EOL method in different virtual sets in units $\left(10^{-23} C_P \langle \boldsymbol{\sigma}_A \rangle |e| \,\mathrm{cm}\right)$ for ^{225}Ra, ^{199}Hg, and ^{171}Yb, compared with data from other methods.

VOS	^{225}Ra	^{199}Hg	^{171}Yb
DF	−57.87	−21.49	−10.84
1	−57.09	−17.16	−6.31
2	−72.95	−19.94	−12.20
3	−75.83	−21.53	−13.26
4	−74.42	−19.45	−13.94
Ref. [37](DHF)	−13.0	−8.7	−2.4
Ref. [37](CI+MBPT)	−64.2	−18.4	−12.4
Ref. [37](RPA)	−61.0	−20.7	−10.9

6.7.2 Wave function relaxation

As explained in the section 6.2 the effects of wave function relaxation were partially accounted for in the present calculations, by using non-orthogonal orbital sets for the opposite parities. An inspection of Table 6.2.1 indicates that the uncertainty which may arise from wave function relaxation effects is of the order of 10%, although this estimate is based on relaxing only the ASF wave function of the ground state on one hand, and the ASF wave functions of all excited states taken together, on the other hand. A more general, albeit far more expensive approach would be to generate separate atomic state functions for the ground state, as well as for each excited state, implying non-orthogonality between all ASFs of both parities.

6.7.3 Energy denominators

As discussed in the section 6.5, the summation in equation (2.3.8) runs over all excited states of appropriate parity and symmetry. The NIST database [81] is of course finite, therefore several levels with unknown energies had to be included in the present calculations. The uncertainty which may arise due to replacements described in the section 6.5, should not exceed 10% in case of radium atom, and we expect the same order of magnitude in case of ytterbium and mercury.

Table 6.7.3: Schiff moment contributions to atomic EDM, calculated with the EOL method in different virtual sets, in units $\left\{10^{-17}[S/(|e|\,\mathrm{fm}^3)]\,|e|\,\mathrm{cm}\right\}$, for ^{225}Ra, ^{199}Hg, and ^{171}Yb, compared with data from other methods.

VOS	^{225}Ra	^{199}Hg	^{171}Yb
DF	−6.32	−2.46	−1.54
1	−7.01	−2.45	−0.88
2	−8.16	−2.23	−1.83
3	−8.59	−2.98	−2.05
4	−8.63	−2.51	−2.15
Ref. [37](DHF)	−1.8	−1.2	−0.42
Ref. [37](CI+MBPT)	−8.84	−2.63	−2.12
Ref. [37](RPA)	−8.27	−2.99	−1.95
Ref. [144](CI+MBPT)	−8.5	−2.8	
Ref. [145](TDHF)		−2.97	−1.91
Ref. [143](CCSD)		−5.07	

Table 6.7.4: Contributions of electron EDM interaction with magnetic field of nucleus, to atomic EDM, calculated with the EOL method in different virtual sets, in units ($d_e \times 10^{-4}$), for ^{225}Ra, ^{199}Hg, and ^{171}Yb, compared with data from other methods.

VOS	^{225}Ra	^{199}Hg	^{171}Yb
DF	−46.67	13.41	5.37
1	−43.69	9.58	3.17
2	−58.07	12.22	5.72
3	−60.13	12.80	6.09
4	−58.45	11.45	6.44
Ref. [37](DHF)	−11	4.9	1.0
Ref. [146](DHF)		5.1	
Ref. [37](CI+MBPT)	−55.7	10.7	5.45
Ref. [37](RPA)	−53.3	12.3	5.05
Ref. [146](RPA)		13	

6.7.4 Systematic errors

The possible sources of systematic errors include: neglecting the contribution of the core excitations to the sum over states, truncation of the summation, contribution of the continuum in equation (2.3.8), omission of double, triple, and higher order substitutions; the effects of Breit interaction; and QED effects. Because of the singular nature of the P-odd and P,T-odd operators, the contribution of the core excitations to the sum (2.3.8) can be quite large and tends to decrease the final result. Table VII in the reference [37] shows the core contributions, of the order of 10%–20%, and for each of the three elements of interest (Yb, Hg, Ra) with opposite sign with respect to the final result. The upper bound on the sum of the trailing terms in the equation (2.3.8) was evaluated in the section 6.6 above, and it is less than 2 percent. The contribution of the continuum is difficult to estimate, since it is partially accounted for by the virtual set. In the present work we neglected the explicit summation over continuum, we assumed that the continuum spectrum contribution may be included into the error budget, and we computed only the contribution of the bound states. The calculations of EDMs involve radial integrals of atomic one-electron orbitals, and all these integrals include factors in the integrands, which effectively cut off the integrals outside the nucleus, so the contribution to the integral comes from within or in the vicinity of the nucleus. Therefore an estimate of systematic errors due to multiple electron substitutions can be made by comparing the EDM calculations with hyperfine structure calculations, where integrand in the form r^{-2} appears in one-electron integrals, which in turn renders the dominant contribution from the first half of the radial orbital oscillation, i.e. near the nucleus. In certain cases in the hyperfine structure calculations the effects of double and triple substitutions can be quite sizeable, of the order of 10-20%, but they often partly cancel and the net deviation is often smaller than 10% [147, 148]. The effects of quadruple and higher order substitutions are negligible. The effects of Breit and QED are usually of the order of 1-2 percent or less for neutral systems.

Based on the above estimates, the relative root-mean-square deviation of the present calculations yields $\sigma = 25\%$.

6.8 Summary and conclusions

Atomic EDMs arising from P,T-odd tensor-pseudotensor and pseudoscalar-scalar electron-nucleon interactions, nuclear Schiff moment, and interaction of electron electric dipole moment with nuclear magnetic field, are presented in Tables 6.7.1, 6.7.2, 6.7.3, and 6.7.4, for the $J=0$ ground states of ^{225}Ra, ^{199}Hg, and ^{171}Yb. The matrix elements and atomic EDMs were calculated using recently developed programs in the framework of the GRASP2K code [43]. One of the objectives of the present calculations was to test these programs. Therefore the results are compared with the data obtained by other methods: random phase approximation (RPA), configuration interaction and many-body perturbation theory approach (CI+MBPT), coupled-cluster single-double (CCSD), and coupled-perturbed Hartree-Fock (CPHF) theory. These methods are usually more accurate in calculations of properties of closed-shell atoms. We should mention that in Tables 6.7.1, 6.7.2, 6.7.3, and 6.7.4, we quoted the final results from the reference [37], corresponding to the CI+MBPT method, as well as their intermediate results, corresponding to the DHF and RPA methods. Similar distinction applies to the RPA and DHF methods in the references [141, 146].

An inspection of the Tables indicates that the differences between our results and the data obtained with the above mentioned methods [37, 141, 142, 144, 145, 146] range between 1.5% for the Schiff moment of Ra (Table 6.7.3), and 22.1% for the tensor-pseudotensor of Hg (Table 6.7.1), all of them within the error bounds.

Despite the reasonable agreement at the level of the correlated calculations, very large differences should be noted at the uncorrelated levels, DF (Dirac-Fock) in our calculations, and DHF (Dirac-Hartree-Fock) in references [37] and [146]. We used the different symbols to visually differentiate the results obtained with different numerical codes, but the DF and DHF approximations are formally identical within the Dirac-Fock theory, and they should yield similar values, within numerical accuracies of the Dirac-Fock codes. A possible explanation of these large differences may be the fact that in our (DF) calculations the summation in equation (2.3.8) runs over only the two lowest excited states, singlet $nsnp\ ^1P$ and triplet $nsnp\ ^3P$, which are generated at the Dirac-Fock level of the GRASP2K code [43]. On the other hand, in references [37] and [146] the summation was probably carried over all excited states, which can be constructed from a suitable set of virtual orbitals. Otherwise we do not have

an explanation.

Large differences at the level of the correlated calculations should be noted between our results and the data obtained with the CPHF theory [139]. The differences are: 18% for TPT of Ra and 39% for TPT of Hg (see Table 6.7.1). The largest disagreement appears to be between the result of the present calculations and the value obtained with the CCSD theory [143] for the Schiff moment of Hg (see Table 6.7.3). The difference amounts to 102%. It is difficult to explain some of the above mentioned differences. They may be due to different orbital shapes, orbital contributions, and relaxation effects, discussed in the sections 6.4 and 6.2, respectively.

Another objective of the present calculations was to test the methods of wave function generation, as described in more detail in the section 2.2.1, and of multiconfiguration expansions designed to account for valence and core-valence electron correlation effects. A reasonably good agreement of our results with the data obtained within the RPA and CI+MBPT methods [37, 141, 142, 144, 145, 146] seems to indicate that the multiconfigurational model employed in the present calculations accounts for the bulk of the electron correlation effects. With adequate computer resources, these calculations may be extended in the future and include also core-core electron correlation effects, as well as the contribution of the core excitations to the sum over states in equation (2.3.8). Based on the experiences with other atomic properties, as well as on the present EDM calculations, we expect that the accuracy of the EDM calculations may be improved by a factor of ten, with respect to the current relative root-mean-square deviation of the order of 25%. Several refinements are possible with respect to the methods used in the present work. To account more accurately for the electron relaxation, separate wave functions for the leading contributors to EDM may be generated. A more general, albeit far more expensive approach would be to generate separate ASFs for the ground state, as well as for each excited state, relaxing orthogonality of the orbital sets between all ASFs of both parities. The upper bound on the tail of the sum over bound states in the equation (2.3.8) can be lowered by generating one or more virtual orbital layers. The evaluation of the sum in equation (2.3.8) over the continuum part of the spectrum can in principle be carried out fully numerically.

The expectation values d_{at}^{int} were calculated with theoretical (if reliable), and experimental (if available) transition energies, as explained in the section 6.5. In fully correlated calculations theoretical transition energies would have to be

evaluated with all single and unrestricted double substitutions. They would be computationally much more expensive than those presented her, but possible with the currently available massively-parallel computers. Electron correlation effects can also be accounted for using the partitioned correlation function interaction (PCFI) method [149], that allows contributions from single and unrestricted double substitutions deep down in the atomic core to be summed up in a very efficient way. In the near future we will be able to perform fully *ab initio* calculations for atoms with arbitrary shell structures. We are currently testing the latest version of the GRASP package [43], with angular programs providing full support for arbitrary numbers of electrons in open *spdf* shells.

Chapter 7

Z-dependence of electric dipole moment in homologous sequence [A7]

The primary objective of the present Chapter is the calculation of EDM for the superheavy element copernicium [150, 151]. We evaluated the contributions to the atomic EDM induced by four mechanisms [19]: tensor-pseudotensor and pseudoscalar-scalar interactions, nuclear Schiff moment, and electron electric dipole moment interaction with the nuclear magnetic field. In each case we show that there is an order of magnitude increase of atomic EDM between mercury and copernicium. The second objective of the Chapter is to derive the Z-dependence of atomic EDM. We show that numerical EDM results are consistent with an exponential Z-dependence along the group 12 elements.

7.1 MCDHF wave functions

We calculated the wave functions of five diamagnetic atoms of group 12, and subsequently the EDMs in the ground states of the entire homologous series, $^{69}_{30}$Zn, $^{111}_{48}$Cd, $^{199}_{80}$Hg, $^{285}_{112}$Cn, and $^{482}_{162}$Uhb. The numerical representations of the wave functions were generated with the relativistic atomic structure package GRASP2K, based on the MCDHF method. Electron correlation effects were evaluated with methods described in our previous papers [A6, A8]. Core-valence and valence-valence correlations were included by allowing single and restricted double substitutions to five sets of virtual orbitals.

The full description of numerical methods, virtual orbital sets, electron substitutions, and other details of the computations can be found in previous Chapter 6 or in [A6]. However, compared with [A6], the double electron substitutions were extended from the $nsnp$ to the $(n-1)dnsnp$ shells in the present work (see section 7.3 below for details).

7.2 EDM calculations

A calculation of an atomic EDM requires evaluation of the matrix elements of the static dipole $\hat{D}_z$, and the matrix elements of the $\hat{H}_{int}$ interactions, which induce an EDM in an atom [36]. Here $\hat{H}_{int}$ represents one of the four interactions mentioned in the Chapter 2, E_0 and E_i are energies of ground and excited states, respectively. The full description of the EDM theory underlying the presents calculations can be found in Chapter 2, and in references therein.

The summation in equation (2.3.8) involves an infinite number of bound states, as well as contributions from the continuum spectrum. The sum over the bound spectrum was evaluated by explicitly calculating contributions from the lowest five odd states of each symmetry using numerical wave functions. Then the method of 'Riemann zeta tail', described in section 6.6, was applied to sum up the contribution from the remaining bound states. To this end we showed that a summation over a Rydberg series, when extrapolated to large values of the principal quantum number n of the running electron (and where the energy denominator saturates at the ionisation energy) converges to the Riemann zeta function. The explicit numerical summation accounts for 98 percent of the whole sum,

Table 7.2.1: TPT interaction contributions to EDM in different virtual sets, in units $\left(10^{-20} C_T \langle \boldsymbol{\sigma}_A \rangle |e| \,\mathrm{cm}\right)$, for ^{69}Zn, ^{111}Cd, ^{199}Hg, and ^{285}Cn, compared with data from other methods. See text for explanations and details.

	^{69}Zn		^{111}Cd		^{199}Hg		^{285}Cn		
VOS	Th	SE	Th	SE	Th	SE	Th	Th2	Th3
DF	−0.07	−0.07	−0.35	−0.36	−7.29	−6.15	−59.86	−61.50	−66.66
1	−0.08	−0.09	−0.39	−0.45	−4.13	−4.86	−48.53	−50.95	−53.95
2	−0.09	−0.11	−0.45	−0.54	−4.66	−5.23	−58.38	−58.92	−62.96
3	−0.10	−0.12	−0.47	−0.57	−4.84	−5.53	−59.31	−64.53	−68.76
4	−0.10	−0.12	−0.48	−0.59	−4.79	−5.64	−57.67	−61.04	−65.26
5	−0.11	−0.12	−0.49	−0.60	−4.84	−5.64	−57.51	−60.75	−64.98
Ref. [37](DHF)						−2.4			
Ref. [141](DHF)						−2.0			
Ref. [37](CI+MBPT)						−5.12			
Ref. [37](RPA)						−5.89			
Ref. [141](RPA)						−6.0			
Ref. [142](CPHF)						−6.75			
Ref. [143](CCSD)						−4.3			

and we evaluated the upper bound on the rest (the infinite tail) of the sum by exploiting regularities of the Rydberg series. The relative correction, i.e. the total contribution from the trailing terms (called Riemann zeta tail) divided by the

total contribution from the five leading terms, is of the order of 1.5 percent for mercury ^{199}Hg, and below 2 percent for copernicium ^{285}Cn. We neglected the Riemann zeta tail correction for the other three elements (^{69}Zn, ^{111}Cd, ^{482}Uhb). The contribution from the continuum is difficult to estimate, since it is partially

Table 7.2.2: PSS interaction contributions to EDM in different virtual sets, in units $\left(10^{-23} C_P \langle \sigma_A \rangle |e|\,\mathrm{cm}\right)$, for ^{69}Zn, ^{111}Cd, ^{199}Hg, and ^{285}Cn, compared with data from other methods. See text for explanations and details.

	^{69}Zn		^{111}Cd		^{199}Hg		^{285}Cn		
VOS	Th	SE	Th	SE	Th	SE	Th	Th2	Th3
DF	−0.13	−0.14	−0.94	−0.96	−25.47	−21.49	−199.52	−252.66	−274.11
1	−0.15	−0.17	−1.05	−1.21	−14.54	−17.16	−199.52	−209.13	−221.73
2	−0.19	−0.23	−1.19	−1.46	−16.38	−18.39	−240.22	−242.15	−259.07
3	−0.20	−0.24	−1.25	−1.53	−17.01	−19.47	−244.96	−266.95	−284.65
4	−0.20	−0.24	−1.28	−1.58	−16.84	−19.84	−237.56	−251.33	−268.95
5	−0.22	−0.24	−1.30	−1.60	−17.02	−19.85	−236.88	−250.07	−267.78
Ref. [37](DHF)						−8.7			
Ref. [37](CI+MBPT)						−18.4			
Ref. [37](RPA)						−20.7			

Table 7.2.3: Schiff moment contributions to atomic EDM in different virtual sets, in units $\left\{10^{-17}[S/(|e|\,\mathrm{fm}^3)]\,|e|\,\mathrm{cm}\right\}$, for ^{69}Zn, ^{111}Cd, ^{199}Hg, and ^{285}Cn, compared with data from other methods. See text for explanations and details.

	^{69}Zn		^{111}Cd		^{199}Hg		^{285}Cn		
VOS	Th	SE	Th	SE	Th	SE	Th	Th2	Th3
DF	−0.04	−0.04	−0.18	−0.19	−2.86	−2.46	−17.73	−17.26	−19.53
1	−0.05	−0.06	−0.21	−0.26	−1.95	−2.45	−13.64	−12.96	−14.53
2	−0.06	−0.07	−0.25	−0.32	−2.11	−2.42	−17.05	−15.96	−17.78
3	−0.06	−0.08	−0.27	−0.34	−2.21	−2.58	−20.09	−22.66	−24.58
4	−0.06	−0.08	−0.28	−0.35	−2.19	−2.62	−17.75	−18.02	−19.95
5	−0.07	−0.08	−0.28	−0.35	−2.22	−2.63	−17.62	−17.77	−19.71
Ref. [37](DHF)						−1.2			
Ref. [37](CI+MBPT)						−2.63			
Ref. [37](RPA)						−2.99			
Ref. [144](CI+MBPT)						−2.8			
Ref. [145](TDHF)						−2.97			
Ref. [143](CCSD)						−5.07			

accounted for by the virtual set [152]. In the present work we computed only the contribution of the bound states. We neglected the explicit summation over continuum, and assumed that the continuum spectrum contribution were included into the error budget. The evaluation of the sum over the continuum part of the spectrum could in principle be carried by an extrapolation, based on the fact, that the oscillator strength density is continuous across the ionization threshold [153],

Table 7.2.4: Contributions of electron EDM interaction with magnetic field of nucleus, to atomic EDM in different virtual sets, in units ($d_e \times 10^{-4}$), for ^{69}Zn, ^{111}Cd, ^{199}Hg, and ^{285}Cn, compared with data from other methods. See text for explanations and details.

	^{69}Zn		^{111}Cd		^{199}Hg		^{285}Cn		
VOS	Th	SE	Th	SE	Th	SE	Th	Th2	Th3
DF	0.13	0.14	−0.62	−0.63	16.04	13.41	314.03	324.40	350.09
1	0.11	0.09	−0.64	−0.71	8.47	9.58	254.78	269.22	283.51
2	0.13	0.13	−0.69	−0.81	9.63	10.64	305.55	309.48	328.86
3	0.14	0.14	−0.72	−0.85	9.99	11.30	305.13	329.18	349.47
4	0.14	0.14	−0.73	−0.87	9.90	11.53	300.39	318.41	338.60
5	0.13	0.11	−0.75	−0.88	10.00	11.50	299.67	317.11	337.40
Ref. [37](DHF)						4.9			
Ref. [146](DHF)						5.1			
Ref. [37](CI+MBPT)						10.7			
Ref. [37](RPA)						12.3			
Ref. [146](RPA)						13			

and above mentioned regularities carry over to the continuum spectrum.

The electronic matrix elements in equation (2.3.8) are not isotope-specific. However, the atomic wave functions do exhibit a (rather weak) dependence on the atomic mass of the element of interest, through the nuclear electrostatic potential, which depends on the nuclear charge density distribution, which in turn depends on the nuclear mass number, through the equation (2.2.3). Therefore, all numerical results in Tables 7.2.1, 7.2.2, 7.2.3, and 7.2.4 were obtained for specific isotopes, such as ^{199}Hg and ^{285}Cn, and they do exhibit a (negligibly weak) dependence on atomic masses.

7.3 Mercury

The calculations for ^{199}Hg were performed in a similar manner as those presented in the previous Chapter 6. The results from DF and from calculations with the first two layers of virtual orbitals (i.e. the first three lines in Tables 7.2.1, 7.2.2, 7.2.3, and 7.2.4) are in fact identical with the results in Chapter 6. Further calculations differ in the scope of the double electron substitutions, which were extended from $6s6p$ to $5d6s6p$ shells.

The results of the calculations are presented in Tables 7.2.1, 7.2.2, 7.2.3, and 7.2.4. The number of virtual orbital sets (VOS) is listed in the first column of each table (see subsection 6.1 definitions and for the details of the calculations). The line marked 'DF' (Dirac-Fock) in the VOS column represents the

lowest-order approximation, with zero sets of virtual orbitals. It should be noted that the values in the Tables marked 'DF' and 'DHF' are not equivalent. Those marked 'DF' were obtained in the present calculations with only the two lowest excited states included in the summation in equation (2.3.8). The results marked 'DHF', obtained with MBPT methods, involved summation over the entire spectrum of virtual orbitals, using various methods to construct the virtual orbital set [37, 141, 146]. Neither 'DF' nor 'DHF' include electron correlation effects and therefore they are relevant only for the purpose of evaluating the contributions of electron correlation for the expectation values of interest.

A larger number of VOS represents in principle a better approximations of the wave function. The line marked '5' in the VOS column represents the final approximation, with five sets of virtual orbitals (MCDHF-VOS.5, represented by red circles in Figure 7.5.2). The difference between VOS.4 and VOS.5 may (cautiously) be taken as an indication of accuracy. For each element the calculated values of the energy denominators in equation (2.3.8) were used to evaluate the atomic EDMs. These fully theoretical EDM values are marked 'Th' in Tables 7.2.1, 7.2.2, 7.2.3, and 7.2.4. Semiempirical EDM values (marked 'SE' in the Tables) were also evaluated for ^{69}Zn, ^{111}Cd, and ^{199}Hg, with the energy denominators taken from the NIST database [81]. Level identifications were made with the atomic state functions transformed from jj-coupling to *LSJ* coupling scheme, using the methods developed in [154, 155].

7.4 Copernicium

Three different sets of energy denominators for ^{285}Cn were used. Those from the present calculations are marked 'Th'. For comparison purposes we computed also the EDMs with the energy denominators taken from two other theoretical papers [156, 157]. The results in column marked 'Th2' were obtained with the energy denominators taken from [156], who used a large-scale MCDHF method. The authors of [156] evaluated also the ionization limit of copernicium and their calculated ionization energy was used in our evaluation of EDMs for those levels which were not reported in [156]. The energy denominators in the columns marked 'Th3' were taken from reference [157], where the energy spectrum was computed with two methods: CI+MBPT and CI. We gave priority to the CI+MBPT results; the CI results were used when CI+MBPT data were not available; for the remaining levels the energy denominators were replaced by the

calculated ground state ionization energy. The accuracy of our calculated energy values, as well as those from the references [156] and [157], is better than 20% for the lowest excited levels of mercury.

The mass number 285 for the element Cn was chosen due to predictions that heavier isotopes are more stable than the lighter ones [158, 27]. The lifetimes of several known isotopes of Cn are counted in minutes [159], which make them amenable to atom traps, and subsequent spectroscopy. It is predicted that still heavier isotopes of Cn, with mass numbers in the range 290–294, may have half-lives counted in years [27].

We observed a similar pattern of contributions from individual electronic states, as described in section 6.4. The triplet $6snp\ ^3P_1$ and the singlet $6snp\ ^1P_1$ states are the dominant contributors to atomic EDM in the ^{199}Hg spectrum. For the ^{285}Cn case the dominant contributions arise from the lowest states of $^{1,3}P_1$ symmetries, i.e. $7snp\ ^1P_1$, $7snp\ ^3P_1$. Altogether they contribute in excess of 98% of the total EDM. The remaining Rydberg states contribute less than 2 percent. Instead of an explicit error analysis for the calculations of EDM for ^{285}Cn we applied a comparison with mercury. Estimates of the magnitudes of EDMs induced by the TPT, PSS, NSM, and eEDM mechanisms in mercury, have been performed with several theoretical methods [37, 142, 143, 145]. With one or two exceptions [143, 160], they all agree within reasonable error bounds — of the order of 10–20 percent (see Section 6.7). The results of the MCDHF calculations for mercury, both in present Chapter as well as in Chapter 6, are well within these bounds. We expect that the present calculations for ^{285}Cn, performed with the same MCDHF model as those for ^{199}Hg, would also fit within error bounds of similar size.

7.4.1 Unhexbium

In addition to the calculations described above we have done uncorrelated DF calculations for $^{482}_{162}$Uhb and for $^{9}_{4}$Be. There are several theoretical predictions [161] - [163] which suggest that the heaviest homologue in the Zn-Cd-Hg-Cn-Uhb group would not be element E162 (Unhexbium), but E164 (Unhexquadium). Due to a very large spin-orbit splitting of the $8p$ shell, the relativistic $8p_{1/2}$ shell becomes occupied before the $7d$ shell is filled [163]. Therefore, at the end of transition metals in the row eight of the periodic table appears the element E164, with the ground configuration [Cn]$5g^{18}6f^{14}7d^{10}7p^{6}8s^{2}8p^{2}$, with

all inner shells closed, and with two electrons in the $8p_{1/2}$ shell (the $8p_{1/2}$ shell is, in fact, also closed). However, the presence of the $8p$ shell would complicate the calculations of EDMs, and, more importantly, it would complicate comparisons along the homologous series. Therefore we have deliberately chosen a (doubly artificial) isotope $^{482}_{162}$Uhb, of element E162, with electron configuration [Cn]$5g^{18}6f^{14}7d^{10}7p^{6}8s^{2}$.

7.5 Z-dependence

Atomic properties depend in various ways on the atomic number Z, both in isoelectronic sequences [82, 164, 165, 166], as well as along homologous sequences [51, 167]. In many cases approximate analytic relations were derived [51, 82, 166, 167], and several atomic observables exhibit a polynomial or power dependencies on the atomic number Z.

Atomic enhancement factors of the PT-odd interactions in neutral atoms scale with nuclear charge as $d_{at} \sim \alpha^2 Z^3$. The factor Z^3 arises from an estimate of the strength of the electric field in the vicinity of an atomic nucleus (see chapter 6.2 of the reference [1]), but it has been pointed out that on top of the Z^3 enhancement of the PT-odd interaction there is another enhancement factor, arising from relativistic contraction of the electronic wave function [1, 29, 54, 56, 168, 169, 170]:

$$K_r \approx \left(\frac{\Gamma(3)}{\Gamma(2\gamma+1)}\right)^2 \left(\frac{2Zr_N}{a_0}\right)^{2\gamma-2}. \tag{7.5.1}$$

Z-dependence of atomic EDMs induced by the P,T-odd $\hat{H}_{int}$ interactions is governed by the Z-dependence of three factors in equation (2.3.8): matrix element of the P,T-odd $\hat{H}_{int}$ operator, matrix element of the electric dipole $\hat{D}_z$ operator, and the energy denominator $(E_0 - E_i)$. The matrix elements of the electric dipole $\hat{D}_z$ operator are constrained by the Thomas-Reiche-Kuhn rule. In case of the elements of group 12 they are further constrained by the Wigner-Kirkwood sum rule (see chapter 14 of the reference [51]). The two lines, $ns^2\,{}^1S_0$ — $nsnp\,{}^3P_1$ and $ns^2\,{}^1S_0$ — $nsnp\,{}^1P_1$, dominate the Wigner-Kirkwood sum in all five elements, making the matrix element of $\hat{D}_z$ approximately constant along the homologous series. Transition energy denominators in the equation (2.3.8) do not depend on Z along the homologous series [167], except for small variations due to shell contractions, shell rearrangements, etc (excluding the Uhb element, with its large spin-orbit splitting mentioned in the section 7.4 above).

Therefore, the dominant role in establishing the Z-dependence of atomic EDMs along the homologous sequence is taken by the $\hat{H}_{int}$ operators. Following the analysis in chapter 8 of the reference [1], it can be shown that in the vicinity of a point-like atomic nucleus the large $P_{n\kappa}$ and small $Q_{n\kappa}$ radial components of a one-electron wave function may be expressed as

$$P_{n\kappa}(r) = \frac{\kappa}{|\kappa|}(\kappa-\gamma)\left(\frac{Z}{a_0^3\nu^3}\right)^{1/2}\frac{2}{\Gamma(2\gamma+1)}\left(\frac{a_0}{2Zr}\right)^{1-\gamma} \tag{7.5.2}$$

$$Q_{n\kappa}(r) = \frac{\kappa}{|\kappa|}(Z\alpha)\left(\frac{Z}{a_0^3\nu^3}\right)^{1/2}\frac{2}{\Gamma(2\gamma+1)}\left(\frac{a_0}{2Zr}\right)^{1-\gamma}, \tag{7.5.3}$$

where κ is the angular momentum quantum number, $\gamma^2 = \kappa^2 - \alpha^2 Z^2$, α is the fine structure constant, ν is the effective principal quantum number, and a_0 is the Bohr radius. The radial integrals involved in the calculations of matrix elements of $\hat{H}_{int}$ include the integrands of the combinations of the large $P_{n\kappa}$ and small $Q_{n\kappa}$ radial components, of the type $(P_aP_b \pm Q_aQ_b)$ or $(P_aQ_b \pm P_bQ_a)$. All these integrals include factors in the integrands which effectively cut off the integrals outside the nucleus (see Chapter 2), and eventually Z-dependence of the atomic EDM in the form

$$d_{at} \sim \left(\frac{Z^k}{a_0^3\nu^3}\right)\left(\frac{2}{\Gamma(2\gamma+1)}\right)^2\left(\frac{2Zr_N}{a_0}\right)^{2\gamma-2} \tag{7.5.4}$$

is obtained, where k depends on a particular form of the integrand and where r_N is the effective cut off radius. The right hand side of the equation (7.5.4) is displayed in Fig. 7.5.1. All four combinations (P_aP_b, Q_aQ_b, P_aQ_b, and P_bQ_a) of the one-electron wave function factors from equations (7.5.2) and (7.5.3) are represented as functions of atomic number Z. The index a represents $ns_{1/2}$ orbitals, the index b represents $np_{3/2}$ orbitals. The nuclear radius r_N has been computed using $r_N = r_0 \cdot A^{1/3}$, where $r_0 = 1.25$ fm. The relation of atomic mass A to atomic number Z has been evaluated from the neutrons to protons ratio $N/Z = 1 + A^{2/3}a_C/2a_A$, derived from the Bethe-Weizsäcker formula [171], with $a_C = 0.711$ and $a_A = 23.7$. The empty circles in the Fig. 7.5.1 show positions of the four elements (Zn, Cd, Hg, Cn). Neglecting a weak Z-dependence through the gamma function $2/\Gamma(2\gamma+1)$, for small values of Z the polynomial factor Z^k determines the functional form of the dependence on Z while for large values of Z the exponential factor $(2Zr_N)^{2\gamma-2}$ takes over. It can be shown numeri-

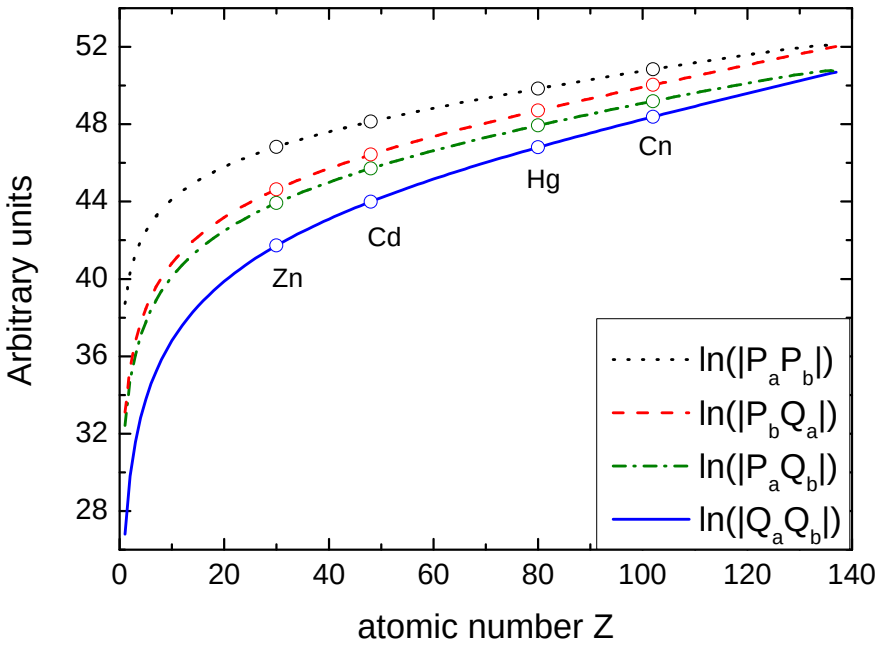

Figure 7.5.1: Z-dependence of the atomic EDM. The right hand side of the equation (7.5.4), calculated from (absolute values of) one-electron wave function factors P_aP_b, Q_aQ_b, P_aQ_b, and P_bQ_a. The factors were generated from the equations (7.5.2) and (7.5.3), and evaluated at $r = r_N$, as functions of atomic number Z. See text for details.

cally, as can bee seen in the Figure 7.5.1, that the polynomial Z^k shape dominates up to about $Z = 60$, then in the range $60 < Z < 120$ the function $d_{at}(Z)$ is approximately exponential, and eventually the approximation breaks down, because the analytic approximation in equations 7.5.2 and 7.5.3 is valid only within the atomic number Z range, where bound solutions of the Dirac equation exist ($Z \leq 137$ for point-like nuclei).

The analysis above has been made under the assumption of a point-like Coulomb field in the Dirac radial equation. The finite sizes of nuclei entered only when the equation (7.5.4) was evaluated. For extended nuclei the solution of the Dirac equation depends on the specific form of the nuclear charge distribution [35, 172, 173]. Flambaum and Ginges [56], and Dzuba *et al* [174] assumed uniform distribution of the electric charge inside a sphere (with the normalization factors from [29]), and obtained enhancement factors of a similar form as in equations (7.5.1) and (7.5.4), for angular symmetries $s_{1/2}$, $p_{1/2}$, and $p_{3/2}$.

In the present work the numerical calculations for the homologous series of the group 12 of the periodic table ($^{69}_{30}$Zn, $^{111}_{48}$Cd, $^{199}_{80}$Hg, $^{285}_{112}$Cn, and $^{482}_{162}$Uhb) were performed with extended nuclear model (2.2.3), for which bound solutions of the

Dirac-Fock equations exist up to $Z = 173$ [175]. The dependence of EDMs on atomic number Z along group 12 of the periodic table is presented in Fig. 7.5.2. The red circles represent our final results, calculated within the MCDHF-VOS.5 electron correlation model described above. The blue pluses represent the uncorrelated DF results. The green plus in the upper right corner represents the EDM value for Uhb. Due to very large spin-orbit splitting of the $8p$ shell, (see section 7.4 above), the Uhb energy denominators are distinctively different from those of other members of the homologous series. To compensate for this splitting, we also computed the EDMs for Uhb with energy denominators taken from Cn. The latter value is represented by the square in Fig. 7.5.2. The solid line is fitted to the four (Zn, Cd, Hg, Cn) final results. The dashed line is fitted to the four uncorrelated DF results. The Uhb results were excluded from the fitting. The regression analysis yields the following relations:

$$\begin{aligned} d^{TPT} &= [-1.22(8)\cdot e^{0.0766(6)\cdot Z} - 5(6)]\cdot 10^{-22} \\ d^{PSS} &= [\ -30(1)\cdot e^{0.0813(3)\cdot Z} - 8.54(1)]\cdot 10^{-26} \\ d^{NSM} &= [-1.77(7)\cdot e^{0.0626(3)\cdot Z} + 2(2)]\cdot 10^{-19} \\ d^{eEDM}/\mu &= [\ 2.74(8)\cdot e^{0.0841(2)\cdot Z} - 15(9)]\cdot 10^{-6}\ , \end{aligned} \tag{7.5.5}$$

where the numbers in parentheses represent RMSE deviations. The third line of the equation (7.5.5) is displayed in Fig. 7.5.2.

Similar regression analysis can be done for the semi-analytic relations presented for the point-nucleus case in the equation (7.5.4) and in the Fig. 7.5.1, but restricted to the range of atomic numbers $30 \leq Z \leq 112$, covered by the four elements (Zn, Cd, Hg, Cn). The analysis yields $d^{PSS} \sim e^{0.017\cdot Z}$ and $d^{NSM} \sim e^{0.022\cdot Z}$, somewhat smaller exponents than those presented in the equation (7.5.5).

The deviation of the EDM value for the element E162 from the fitted function in Figure 7.5.2 may be explained by several possible mechanisms: rearrangements of the valence shells, i.e. relativistic contraction of the $8s$ and $8p_{1/2}$ shells, which results in the above mentioned large spin-orbit splitting of the $8p$ shell; variation of transition energy denominators, induced by shell rearrangements; contribution of QED effects, which could be quite sizeable near the end of the periodic table at $Z = 173$ [175, 176]. However, the most likely explanation is the breakdown of the exponential approximation near the end of the periodic table. The analytic approximation in equations 7.5.2 and 7.5.3 is valid only within the atomic number Z range, where bound solutions of the Dirac equation exist

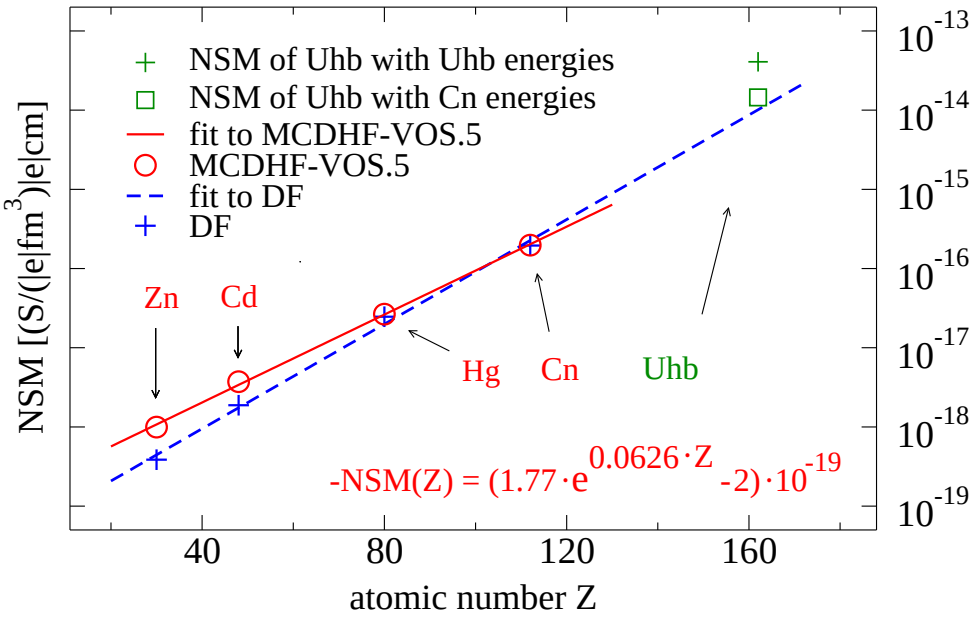

Figure 7.5.2: Atomic EDM (absolute values) induced by the NSM as a function of atomic number Z. Red circles = MCDHF-VOS.5 results with 5 virtual orbital sets. Blue pluses = uncorrelated DF results (0 sets). The lines are exponential functions fitted to the four points, representing Zn, Cd, Hg, and Cn. Solid red line = fit to MCDHF-VOS.5 results. Dashed blue line = fit to uncorrelated DF results. The lines are extrapolated beyond $Z = 112$. The two symbols in the upper right corner represent Uhb (excluded from the fitting). Green plus = DF result for Uhb with calculated Uhb energy denominators. Green square = DF result for Uhb with energy denominators taken from Cn. The sizes of circles represent approximately the relative accuracy of the MCDHF-VOS.5 calculations. See text for details.

($Z \leq 137$ for point-like nuclei, $Z \leq 173$ for extended nuclei). The element E162 is close to the end of the periodic table at $Z = 173$, where determination of a numerical wave function, even at the Dirac-Fock level, may be problematic or impossible, and one might expect a question whether perturbation theory still works in QED for elements close to Z = 173 [175].

At very short distances Z-dependence algebra is dominated by the cutoff radii r_N (related to the sizes of the nuclei), and by the power series solutions for $P_{n\kappa}$ and $Q_{n\kappa}$ at the origin [35]. The power series coefficients for $P_{n\kappa}$ and $Q_{n\kappa}$ depend on the nuclear potential (again related to the sizes of the nuclei), and are constrained by orthogonality of the one-electron functions with the same symmetry. The dominant contributions to the matrix elements of the $\hat{H}_{int}$ operators come from the valence ns^2 orbitals in the ground state, and from the lowest $np_{1/2}$ and $np_{3/2}$ orbitals in the excited states.

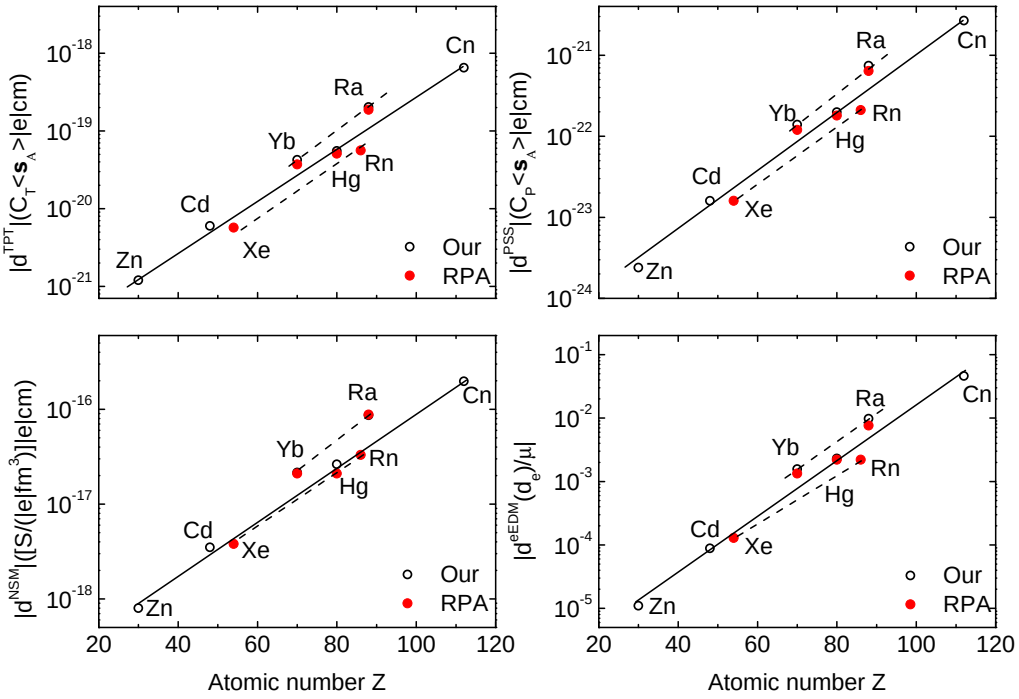

Figure 7.5.3: Atomic EDM induced by TPT, PSS, NSM, and eEDM as functions atomic number Z. Empty circles represents data obtained with MCDHF method [A6,A7]. Data from [A7] were used for Hg. Red circles represents data from random phase approximation [37]. Solid lines show trends along homologous sequence. Dashed lines connect two noble gases (Xe, Rn) and two closed-shell ns^2 elements (Yb, Ra).

Our computed EDM enhancement factors for all mechanisms are presented in figure 7.5.3, and compared with data obtained from random phase approximation [37]. Small differences with respect to random phase approximation for Yb, Ra, and Hg, may be explained by differences in correlation effects accounted for in the two calculations, as described in the section 6.7. One should not draw conclusions based only on two points, but the results obtained for two noble gases (Xe,Rn), and two closed-shell ns^2 elements (Yb,Ra) exhibit similar slopes as those for group 12 elements.

The left graph in the Fig. 7.5.4 shows the coefficient p_0 of the lowest order polynomial in the series expansion at the origin of the large component P of the radial function of the valence orbitals (ns, $np_{1/2}$, $np_{3/2}$) of the elements from the group 12 (plus beryllium). The quantum number n assumes the values 2, 4, 5, 6, 7, 8 for Be, Zn, Cd, Hg, Cn, Uhb, respectively. The right graph in the Fig. 7.5.4 shows the atomic EDMs induced by the TPT, PSS, NSM, and eEDM mechanisms, as functions of atomic number Z for the elements of the group 12 (plus Be). For the purpose of this comparison, all values in Fig. 7.5.4 were obtained in

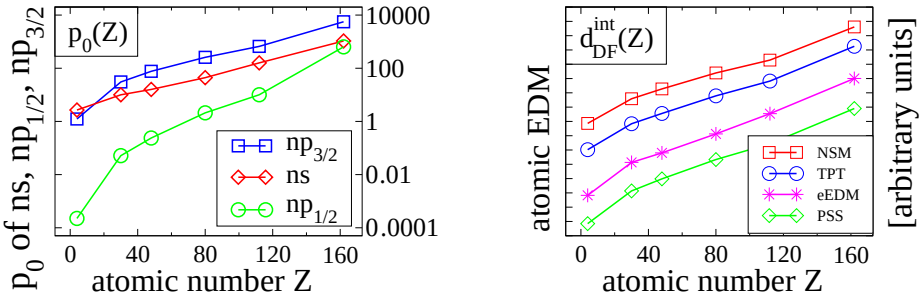

Figure 7.5.4: Left: power series coefficients p_0 of valence orbitals as functions of atomic number Z. Blue squares = $np_{3/2}$; red diamonds = ns; green circles = $np_{1/2}$; $n = 2, 4, 5, 6, 7, 8$ for Be, Zn, Cd, Hg, Cn, Uhb, respectively. Right: atomic EDM (in arbitrary units on logarithmic scale) induced by NSM (red squares), TPT (blue circles), eEDM (magenta stars), and by PSS (green diamonds), as functions of atomic number Z. All lines in both graphs are drawn only for the guidance of the eyes. See text for details.

the Dirac-Fock approximation, without account of electron correlation effects, and with the extended nuclear model (2.2.3). Analogously to the point nucleus case (represented by the equation (7.5.4)), the function $d_{at}(Z)$ is approximately exponential in the range $60 < Z < 120$, i.e. for heavy and superheavy elements relevant from the point of view of the EDM searches. Both graphs in Fig. 7.5.4 show similar Z-dependencies as those in Figure 7.5.1, i. .e. the polynomial shape up to about $Z = 60$, then approximately exponential in the range $60 < Z < 120$, and eventually the exponential approximation breaks down near the end of the extended Periodic Table of Elements [163, 175] at $Z = 173$. When comparing the shapes of the curves in the left and right graphs, one has to bear in mind that radial integrals in matrix elements of the $\hat{H}_{int}$ operators involve valence ns^2 orbitals in the ground state, and $np_{1/2}$ and $np_{3/2}$ orbitals in the excited states. The apparent similarity of the $np_{1/2}$ and $np_{3/2}$ curves in the left graph and the four curves in the right graph is a numerical confirmation of the dominant role of power series coefficients in the matrix element of the $\hat{H}_{int}$ operators, as well as of the proportionality relations between matrix elements, established in [174]. Beryllium does not belong to the group 12 (which results in the visible deviation of Be from the fitted function) but was included in Fig. 7.5.4 to indicate that the dominant role of power series coefficients, as well as the proportionality relations [174], are not limited to one group of elements. The other deviations from linearity in the Figure 7.5.4 are induced by electron correlation effects, whose contributions differ from element to element due to shell rearrangements.

7.6 Conclusions

The main conclusion of the present thesis is the suggestion for setting up an EDM experiment on a superheavy element, which would result in an order of magnitude increase of sensitivity, compared to a homologous heavy element. Such homologous pairs include (but are not limited to) Yb–No, Hg–Cn, Tl–Nh, Po–Lv, At–Ts, Rn–Og, Fr–E119, Ra–E120. The names recently approved by IUPAC: Nihonium (113-Nh), Tennessine (117-Ts), and Oganesson (118-Og). If the exponential Z-dependence derived in the present work is assumed for all above homologous pairs, an increase of sensitivity by a factor 8-30 should be expected. The best limit on the EDM of a diamagnetic atom comes from ^{199}Hg, for which $d(^{199}\mathrm{Hg}) < 3.1 \times 10^{-29} e\cdot$cm (95% C.L.) has been reported [15]. Our calculations indicate that for the Hg–Cn pair the increase of sensitivity would be 57.5/4.8, 236.9/17.0, 17.6/2.2, and 299.7/10.0 for TPT, PSS, NSM, and eEDM, respectively. Over the last 50 years the precision of EDM experiments has been improving by about an order of magnitude per decade [2, 15, 17, 177, 178, 179]. On this timescale an experiment on Cn would be equivalent to time travel into the future over a distance of about ten to twenty years.

Chapter 8

The main conclusions

All computation were performed using multiconfiguration Dirac-Hartree-Fock (MCDHF) [44] and relativistic configuration interaction methods (RCI) [42], implemented in the GRASP2K package [43].

1. For the 15 lowest states of nitrogen-like ions the mean relative energy differences are around 0.04% (NIST database) for the four ions Cr XVIII, Fe XX, Ni XXII, and Zn XXIV. This translates into wavelengths that are accurate to within ± 10 mÅ and thus of spectroscopic accuracy. The high accuracy carries over also to higher states. Differences between two gauges for electric dipole transition rates within lower states are 1.9% on average. We thus argue that the rates for 39 488 transitions of type E1, E2, and M1 are highly accurate and may serve as benchmark for other calculations.

2. Energies of Si-like ions Ti IX - Ge XIX, Sr XXV, Zr XXVII, and Mo XXIX are in excellent agreement with observations (up to 0.03%) and computed wavelengths are almost of spectroscopic accuracy, aiding line identification in spectra. Differences between two gauges for majority of stronger transitions are below 1%, and for weaker transitions they are larger, from a few percent up to 10%. We thus argue that the transition rates are highly accurate and may serve as benchmark for other calculations.

3. The analysis of Er^{3+} energy levels shows that values converge, when the core is opened up to shells with $n = 3$, and important valence, core, and core-valence correlations are included. With this strategy an accuracy up to 9.8% was achieved, compared to NIST database.

4. Our results demonstrated that $^{151}_{63}$Eu, $^{155}_{64}$Gd, $^{229}_{90}$Th, and $^{231}_{91}$Pa of He-like ions are the most promising for future experiments, due to high values of the transition rates induced by weak interaction and off-diagonal hyperfine structure.

5. The disagreement between calculations of electric dipole moments, arising from tensor-pseudotensor interaction varies from 4% for Hg (compared to coupled-cluster method in single-double approximation) up to 24% for Hg (compared to random phase approximation).

6. The discrepancy between calculations of electric dipole moments, arising from pseudoscalar-scalar interaction, varies from 4% for Hg 22% to for Yb (in both cases compared to random phase approximation).

7. Calculated electric dipole moment, arising from nuclear Schiff moment completely agrees with data from CI+MBPT (configuration interaction and many-body perturbation theory approach) (disagreement is 0% for Hg) and disagrees with data from random phase approximation (14%, also for Hg).

8. A reasonably good agreement was obtained for electric dipole moment, arising from electron electric dipole moment interaction with nuclear magnetic moment (eEDM), against data from CI+MBPT (configuration interaction and many-body perturbation theory approach) (5% for Ra), but no so good against data from random phase approximation (22% for Yb).

9. The results of atomic electric dipole moment calculations show, that multiconfiguration Dirac-Hartree-Fock method, our suggested electron correlation strategies, as well as programs written for this project are suitable for testing parity and time-reversal symmetries in atomic theory.

10. For the Hg–Cn pair our calculations indicate an increase of enhancement factors for an atomic electric dipole moment, 57.5/4.8, 236.9/17.0, 17.6/2.2, and 299.7/10.0, for tensor-pseudotensor, pseudoscalar-scalar, nuclear Schiff moment, and electron electric dipole moment, respectively.

11. Setting up an electric dipole moment experiment on a superheavy element would result in an order of magnitude increase of sensitivity, compared to a homologous heavy element. Such homologous pairs include (but are not limited to) Yb–No, Hg–Cn, Tl–Nh, Po–Lv, At–Ts, Rn–Og, Fr–E119, and Ra–E120.

References

[1] I. B. Khriplovich and S. K. Lamoreaux, *CP Violation Without Strangeness* (Springer, Berlin, 1997).

[2] K. Jungmann, Ann. Phys. **525**, 550 (2013).

[3] C. S. Wu, E. Ambler, R. W. Hayward, D. D. Hoppes, and R. P. Hudson, Phys. Rev. **105**, 1413 (1957).

[4] R. L. Garwin, L. M. Lederman, and M. Weinrich, Phys. Rev. **105**, 1415 (1957).

[5] J. I. Friedman and V. L. Telegdi, Phys. Rev. A **106**, 1290 (1957).

[6] J. H. Christenson, J. W. Cronin, V. L. Fitch, and R. Turlay, Phys. Rev. Lett. **13**, 138 (1964).

[7] A. Angelopoulos, A. Apostolakis *et al.* (CPLEAR Collaboration), Phys. Lett. B **444**, 43 (1998).

[8] L. Wolfenstein, Int. J. Mod. Phys. E **08**, 501 (1999).

[9] J. Bernabeu, A. Di Domenico, and P. Villanueva-Perez, Nucl. Phys. B **868**, 102 (2013).

[10] J. P. Lees *et al.* (BABAR Collaboration), Phys. Rev. Lett. **109**, 211801 (2012).

[11] N. Cabibbo, Phys. Rev. Lett. **10**, 531 (1963).

[12] M. S. Sozzi, *Discrete Symmetries and CP Violation. From Experiment to Theory* (OUP, Oxford, 2008).

[13] V. A. Dzuba and V. V. Flambaum, Int. J. Mod. Phys. E **21**, 1230010 (2012).

[14] B. C. Regan, E. D. Commins, C. J. Schmidt, and D. De Mille, Phys. Rev. Lett. **88**, 071805 (2002).

[15] W. C. Griffith, M. D. Swallows, T. H. Loftus, M. V. Romalis, B. R. Heckel, and E.N. Fortson, Phys. Rev. Lett. **102**, 101601 (2009).

[16] J. J. Hudson, D. M. Kara, I. J. Smallman, B. E. Sauer, M. R. Tarbutt, and E. A. Hinds, Nature (London) **473**, 493 (2011).

[17] T. A. C. J. Baron, W. C. Campbell, D. De Mille, J. M. Doyle, G. Gabrielse, Y. V. Gurevich, P. W. Hess, N. R. Hutzler, E. Kirilov, I. Kozyryev *et al.*, Science **343**, 269 (2014).

[18] C. A. Baker, D. D. Doyle, P. Geltenbor, K. Green, M. G. D. van der Grinten, P. G. Harris, P. Iaydjiev, S. N. Ivanov, D. J. R. May, J. M. Pendlebury, J. D. Richardson, D. Shiers, and K. F. Smith, Phys. Rev. Lett. **97**, 131801 (2006).

[19] J. S. M. Ginges and V. V. Flambaum, Phys. Rep. **397**, 63 (2004).

[20] *Advanced Series on Directions in High Energy Physics*, edited by B. L. Roberts and W. J. Marciano (World Scientific, Singapore, 2010), Vol. 20.

[21] C. E. Wieman, D. E. Pritchard, and D. J. Wineland, Rev. Mod. Phys. **71**, S253 (1999).

[22] S. De, U. Dammalapati, and L. Willmann, Phys. Rev. A **91**, 032517 (2015).

[23] D. J. Wineland, Rev. Mod. Phys. **85**, 1103 (2013).

[24] A. D. Ludlow, M. M. Boyd, and J. Ye, Rev. Mod. Phys. **87**, 637 (2015).

[25] R. H. Parker, M. R. Dietrich, M. R. Kalita, N. D. Lemke, K. G. Bailey, M. N. Bishof, J. P. Greene, R. J. Holt, W. Korsch, Z.-T. Lu, P. Mueller, T. P. O'Connor, and J. T. Singh, Phys. Rev. Lett. **114**, 233002 (2015).

[26] B. Cheal and K. T. Flanagan, J. Phys. G: Nucl. Part. Phys. **37**, 113101 (2010).

[27] V. Zagrebaev, A. Karpov, and W. Greiner, J. Phys.: Conf. Ser. **420**, 012001 (2013).

[28] Y. Oganessian, J. Phys.: Conf. Ser. **337**, 012005 (2012).

[29] I. B. Khriplovich, *Parity Nonconservation in Atomic Phenomena* (Gordon and Breach, Philadelphia, 1991).

[30] J. Ekman, P. Jönsson, S. Gustafsson, H. Hartman, G. Gaigalas, M. R. Godefroid, and C. Froese Fischer, A&A **564**, A24 (2014).

[31] E. Fermi, Zs. Phys. **88**, 161 (1934).

[32] V. G. Gorshkov and L. I. Labzovskiĭ, JETP Lett. **19**, 394 (1974).

[33] L. N. Labzowsky, A. V. Nefiodov, G. Plunien, G. Soff, R. Marrus, and D. Liesen, Phys. Rev. A **63**, 054105 (2001).

[34] C. Caso, G. Conforto, A. Gurtu *et al.* (Particle Data Group), Eur. Phys. J. C **3**, 1 (1998).

[35] I. P. Grant, *Relativistic Quantum Theory of Atoms and Molecules: Theory and Computation* (Springer, New York, 2007).

[36] G. Gaigalas, Z. Rudzikas, and C. Fischer Froese, J. Phys. B: At. Mol. Opt. Phys. **30**, 3747 (1997).

[37] V. A. Dzuba, V. V. Flambaum, and S. G. Porsev, Phys. Rev. A **80**, 032120 (2009).

[38] K. G. Dyall, I. P. Grant, C. T. Johnson, F. A. Parpia, and E. P. Plummer, Comput. Phys. Commun. **55**, 425 (1989).

[39] F. A. Parpia, C. Froese Fischer, and I. P. Grant, Comput. Phys. Commun. **94**, 249 (1996).

[40] I. P. Grant. Comput. Phys. Commun. **44**, 59 (1994).

[41] P. Jönsson, X. He, C. Froese Fischer, and I. P. Grant, Comput. Phys. Commun. **176**, 597 (2007).

[42] B. McKenzie, I. P. Grant, and P. H. Norrington, Comput. Phys. Commun. **21**, 233 (1980).

[43] P. Jönsson, G. Gaigalas, J. Bieroń, C. Froese Fischer, and I. P. Grant, Comput. Phys. Commun. **184**, 2197 (2013).

[44] C. F. Fischer, M. Godefroid, T. Brage, P. Jönsson, and G. Gaigalas, J. Phys. B: At. Mol. Opt. Phys. **49**, 182004 (2016).

[45] I.P. Grant, J. Phys. B **7**, 1458 (1974).

[46] G. Gaigalas, S. Fritzsche, and I. P. Grant, Comput. Phys. Commun. **139**, 263 (2001).

[47] J. Olsen, M. Godefroid, P. Jönsson, P.Å. Malmqvist, and C. Froese Fischer, Phys. Rev. E **52**, 4499 (1995).

[48] P. Jönsson, F. A. Parpia, and C. Froese Fischer, Comput. Phys. Commun. **96**, 301 (1996).

[49] P. Å. Malmqvist, Int. J. Quantum Chem. **30**, 479 (1986).

[50] V. Berestetskii, E. Lifshitz, and L. Pitaevskii, *Quantum Electrodynamics* (Pergamon Press, Oxford, U.K., New York, 1982).

[51] R. D. Cowan, *The Theory of Atomic Structure and Spectra* (University of California, Berkeley, 1981).

[52] W. R. Johnson, K. T. Cheng, and D. R. Plante, Phys. Rev. A **55**, 2728 (1997).

[53] P. G. H. Sandars, J. Phys. B **1**, 511 (1968).

[54] O. P. Sushkov, V. V. Flambaum and I. B. Khriplovich, Zh. Eksp. Teor. Fiz. **87**, 1521 (1984).

[55] E. N. Fortson and L. L. Lewis, Phys. Rep. **113**, 298 (1984).

[56] V. V. Flambaum and J. S. M. Ginges, Phys. Rev. A **65**, 032113 (2002).

[57] K. Wilhelm, P. Lemaire, W. Curdt *et al.*, Sol. Phys. **170**, 75 (1997).

[58] P. Lemaire, K. Wilhelm, W. Curdt *et al.*, Sol. Phys. **170**, 105 (1997).

[59] R. Mewe, A. J. J. Raassen, J. J. Drake *et al.*, A&A **368**, 888 (2001).

[60] R. Mewe, A. J. J. Raassen, J.P. Cassinelli *et al.*, A&A **398**, 203 (2003).

[61] K. J. van der Heyden, J. A. M. Bleeker, J. S. Kaastra, and J. Vink, A&A **406**, 141 (2003).

[62] J. K. Lepson, P. Beiersdorfer, J. Clementson, M. F. Gu, M. Bitter, L. Roquemore, R. Kaita, P. G. Cox, and A. S. Safronova, Phys. B: At. Mol. Opt. Phys. **43**, 144018 (2010).

[63] F. P. Keenan, D. B. Jess, K. M. Aggarwal, R. J. Thomas, J. W. Brosius, and J. M. Davila, Mon. Not. R. Astron. Soc. **376**, 205 (2007).

[64] T. Watanabe, H. Hara, N. Yamamoto, D. Kato, H. A. Sakaue, I. Murakami, T. Kato, N. Nakamura, and P. R. Young, ApJ **692**, 1294 (2009).

[65] G. Del Zanna, A&A **533**, A12 (2011).

[66] N. Yamamoto, T. Kato, H. Funaba, K. Sato, N. Tamura, S. Sudo, P. Beiersdorfer, and J. K. Lepson, ApJ **689**, 646 (2008).

[67] N. Nakamura, E. Watanabe, H. Sakaue, D. Kato, I. Murakami, N. Yamamoto, H. Hara, and I. Watanabe, ApJ **739**, 17 (2011).

[68] G. Del Zanna, A&A **558**, A73 (2013).

[69] G. Del Zanna, P. Storey, and H. E. Manson, A&A **567**, A18 (2014).

[70] L. Sturesson, P. Jönsson, and C. Froese Fischer, Comput. Phys. Commun. **177**, 539 (2007).

[71] M. J. Vilkas and Y. Ishikawa, Advances in Quantum Chemistry **261**, 39 (2001).

[72] G. Merkelis, M. J. Vilkas, R. Kisielius, and G. Gaigalas, Phys. Scr. **56**, 41 (1997).

[73] G. Merkelis, I. Martinson, R. Kisielius, and M. J. Vilkas, Phys. Scr. **59**, 122 (1999).

[74] S. Kotochigova, M. Linnik, K. P. Kirby, and N. S. Brickhouse, Astrophys. J. Suppl. Ser. **186**, 85 (2010).

[75] A. K. Bhatia, J. F. Seely, and U. Feldman, At. Data Nucl. Data Tables **43**, 99 (1989).

[76] S. N. Nahar, A&A **413**, 779 (2004).

[77] V. Jonauskas, P. Bogdanovich, F. P. Keenan, M. E. Foord, R. F. Heeter, S. J. Rose, G. J. Ferland, R. Kisielius, P. A. M. van Hoof, and P. H. Norrington, A&A **433(2)**, 745 (2005).

[78] M. F. Gu, Astrophys. J. Suppl. Ser. **156**, 105 (2005).

[79] P. Rynkun, P. Jönsson, G. Gaigalas, and C. Froese Fischer, At. Data Nucl. Data Tables **100**, 315 (2014).

[80] J. Ekman, M. Godefroid, and H. Hartman, Atoms **2(2)**, 215 (2014).

[81] A. Kramida, Yu. Ralchenko, J. Reader and NIST ASD Team (2016). NIST Atomic Spectra Database (version 5.4), [Online]. Available: `http://physics.nist.gov/asd [Fri Sep 30 2016]`. National Institute of Standards and Technology, Gaithersburg, MD.

[82] C. Froese Fischer, T. Brage, and P. Jönsson, *Computational Atomic Structure. An MCHF Approach* (Institute of Physics Publishing, London, 1997).

[83] F. J. Galvez, E. Buendia, and A. Sarsa, The Journal of Chemical Physics **123**, 034302 (2005).

[84] C. Froese Fischer, G. Tachiev, and A. Irimia, At. Data and Nucl. Data Tables **92**, 607 (2006).

[85] C. Kohstall, S. Fritzsche, B. Fricke and W.-D. Sepp, At. Data and Nucl. Data Tables **70**, 63 (1998).

[86] M. Huang, M. Andersson, T. Brage, R. Hutton, P. Jönsson, and T. Zou, J. Phys. B: At. Mol. Opt. Phys. **38**, 503 (2005).

[87] M. Andersson and T. Brage, J. Phys. B: At. Mol. Opt. Phys. **40**, 709 (2007).

[88] K. M. Aggarwal and F. P. Keenan, A&A **418**, 371 (2004).

[89] P. Storey and C. Zeippen, A&A **511**, A78 (2010).

[90] E. Landi and A. K. Bhatia, At. Data and Nucl. Data Tables **98**, 862 (2012).

[91] G. P. Gupta and A. Z. Msezane, Phys. Scr. **86**, 015303 (2012).

[92] Y. Ishikawa and M. J. Vilkas, Phys. Rev. A **63**, 042509 (2001).

[93] Y. Ishikawa and M. J. Vilkas, Phys. Scr. **65**, 219 (2002).

[94] Y. Ishikawa and M. J. Vilkas, J. Phys. B: At. Mol. Opt. Phys. **36**, 4641 (2003).

[95] Y. Ishikawa and M. J. Vilkas, Phys. Rev. A **68**, 012503 (2003).

[96] Y. Ishikawa and M. J. Vilkas, J. Phys. B: At. Mol. Opt. Phys. **37**, 1803 (2004).

[97] M. J. Vilkas and Y. Ishikawa, Phys. Rev. A **69**, 062503 (2004).

[98] E. Träbert, Y. Ishikawa, J. A. Santana, and G. Del Zanna, Can. J. Phys. **89**, 403 (2011).

[99] E. Träbert, J. H. Blanke, P. H. Heckmann, H. M. Hellmann, and R. Hucke, Z. Phys. Atoms and Nuclei **321**, 359 (1985).

[100] E. Träbert, Z. Phys. Atoms, Molecules, and Clusters **2**, 213 (1986).

[101] E. Träbert, P. H. Heckmann, R. Hutton, and I. Martinson, J. Opt. Soc. Am. B **5**, 2173 (1988).

[102] E. Träbert, N. Reistad, I. Martinson, and R. Hutton, Z. Phys. Atoms, Molecules, and Clusters **11**, 207 (1989).

[103] E. Träbert, Mon. Not. R. Astron. Soc. **297**, 399 (1998).

[104] E. Träbert, A. G. Calamai, G. Gwinner, E. J. Knystautas, E. H. Pinnington, and A. Wolf, J. Phys. B **36**, 1129 (2003).

[105] E. Träbert, Phys. Scr. **T120**, 56 (2005).

[106] E. Landi *et al.*, ApJS, 763, 86 (2013). CHIANTI (version 7) `http://www.chiantidatabase.org/referencing.html [Fri Sep 30 2016]`

[107] C. M. Brown, U. Feldman, J. F. Seely, and C. M. Korendyke, ApJS **176**, 511 (2008).

[108] S. Levchuk, H. Maier, H. Bolt, and A. Suzuki, J. Nucl. Mater **367**, 1033 (2007).

[109] D. Kato, A. H. Sakaue, I. Murakami, T. Tanaka, T. Muroga, and A. Sagara, Plasma and Fusion Res. **7**, 2405043 (2012).

[110] I. Lindgren and J. Morrison, *Atomic Many-Body Theory* (Springer, New York, 1982).

[111] V. A. Dzuba, V. V. Flambaum, and M. G. Kozlov, Phys. Rev. A **54**, 3948 (1996).

[112] M. J. Vilkas and Y. Ishikawa, Phys. Rev. A **69**, 062503 (2004).

[113] W. R. Johnson, D. R. Plante, and J. Sapirstein, Advances in Atomic, Molecular, and Optical Physics **35**, 255 (1995).

[114] V. A. Fock, *Selected Works; Quantum Mechanics and Quantum Field Theory* (Boca Raton, Chapman & Hall, CRC, 2004).

[115] C. Froese Fischer, G. Tachiev, G. Gaigalas, and M. R. Godefroid, Comput. Phys. Commun. **176**, 559, (2007).

[116] W. J. Carter Ph.D. Thesis, Johns Hopkins University. 1966.

[117] W. F. Krupke and J. B. Gruber, J. Chem. Phys. **39**, 1024, (1963).

[118] W.F. Krupke and J.B. Gruber, J. Chem. Phys. **41**, 1225, (1964).

[119] M. Vasile, N. Avram, P. Vlazan, I. Grozescu, and M. Miclau, J. of Optoelectronics and Advanced Materials **10**, 2898 (2008).

[120] M. J. Weber, Phys. Rev. **157** 262, (1967).

[121] B. G. Wybourne, *Spectroscopic properties of rare earths* (New York, Wiley, 1966).

[122] D. J. Newman and B. Ng, Rep. Prog. Phys. **52**, 699 (1989).

[123] W. R. Johnson, *Atomic Structure Theory* (Springer, New York, 2007).

[124] J. Olsen, B. O. Roos, P. Jorgensen, and H. J. Aa. Jensen, J. Chem. Phys. **89**, 2185 (1988).

[125] G. Gaigalas, Z. Rudzikas, and F. C. Fischer, At. Data Nucl. Data Tables **70(1)**, 1 (1998).

[126] B. G. Wybourne, J. Chem. Phys. **32**, 639 (1960).

[127] Z. B. Rudzikas and J. V. Čyplys, Phys. Scr. **T26**, 21 (1989).

[128] A. Bondarevskaya, A. Prozorov, L. Labzowsky, G. Plunien, D. Liesen, and F. Bosch, J. Phys.: Conf. Ser. **163**, 012012 (2008).

[129] J. G. Li, P. Jönsson, G. Gaigalas, and C. Z. Dong, Eur. Phys. J. D **55**, 313 (2009).

[130] A. Derevianko and W. R. Johnson, Phys. Rev. A **56**, 1288 (1997).

[131] D. R. Plante, W. R. Johnson, and J. Sapirstein, Phys. Rev. A **49**, 3519 (1994).

[132] A. Artemyev, V. Shabaev, V. Yerokhin, G. Plunien, and G. Soff, Phys. Rev. A **71**, 062104 (2005).

[133] M. Maul, A. Schäfer, W. Greiner, and P. Indelicato, Phys. Rev. A **53**, 3915 (1996).

[134] J. Bieroń, G. Gaigalas, E. Gaidamauskas, P. Indelicato, S. Fritzsche, and P. Jönsson, Phys. Rev. A **80**, 012513 (2009).

[135] J. Bieroń and P. Pyykkö, Phys. Rev. A **71**, 032502 (2005).

[136] J. Bieroń, C. Froese Fischer, P. Indelicato, P. Jönsson, and P. Pyykkö, Phys. Rev. A **79**, 052502 (2009).

[137] J. Bieroń, C. Froese Fischer, S. Fritzsche, and K. Pachucki, J. Phys. B: At. Mol. Opt. Phys. **37**, L305 (2004).

[138] B. M. Roberts, V. A. Dzuba, and V. V. Flambaum, Phys. Rev. A **89**, 042509 (2014).

[139] K. V. P. Latha and P. R. Amjith, Phys. Rev. A **87**, 022509 (2013).

[140] I. Ahmad, U. Griesmann, I. Martin, W. Dussa, M. A. Baig, and J. Hormes, J. Phys. B: At. Mol. Opt. Phys. **29**, 2963 (1996).

[141] A.-M. Mårtensson-Pendrill, Phys. Rev. Lett. **54**, 1153 (1985).

[142] K. V. P. Latha, D. Angom, R. J. Chaudhuri, B. P. Das, and D. Mukherjee, J. Phys. B: At. Mol. Opt. Phys. **41**, 035005 (2008).

[143] K. V. P. Latha, D. Angom, B. P. Das, and D. Mukherjee, Phys. Rev. Lett. **103**, 083001 (2009).

[144] V. A. Dzuba, V. V. Flambaum, J. S. M. Ginges, and M. G. Kozlov, Phys. Rev. A **66**, 012111 (2002).

[145] V. A. Dzuba, V. V. Flambaum, and J. S. M. Ginges, Phys. Rev. A **76**, 034501 (2007).

[146] A.-M. Mårtensson-Pendrill and P. Öster, Phys. Scr. **36**, 444 (1987).

[147] B. Engels, Theor. Chim. Acta **86**, 429 (1993).

[148] J. Bieroń, C. Froese Fischer, P. Jönsson, and P. Pyykkö, J. Phys. B: At. Mol. Opt. Phys. **41**, 115002 (2008).

[149] S. Verdebout, P. Rynkun, P. Jönsson, G. Gaigalas, C. Froese Fischer, and M. Godefroid, J. Phys. B: At. Mol. Opt. Phys. **46**, 085003 (2013).

[150] R. Eichler, N. V. Aksenov, A. V. Belozerov, G. A. Bozhikov, V. I. Chepigin, S. N. Dmitriev, R. Dressler, H. W. Gaåggeler, V. A. Gorshkov, F. Haenssler, M. G. Itkis, A. Laube, V. Ya. Lebedev, O. N. Malyshev, Yu. Ts. Oganessian, O. V. Petrushkin, D. Piguet, P. Rasmussen, S. V. Shishkin, A. V. Shutov, A. I. Svirikhin, E. E. Tereshatov, G. K. Vostokin, M. Wegrzecki, and A. V. Yeremin, Nature (London) **447**, 72 (2002).

[151] R. C. Barber, H. W. Gåggeler, P. J. Karol, H. Nakahara, E. Vardaci, and E. Vogt, Pure Appl. Chem. **81**, 1331 (2009).

[152] R. D. Cowan, E. Jörgen, and E. Hansen, J. Opt. Soc. Am **71**, 60 (1981).

[153] U. Fano and J. W. Cooper, Rev. Mod. Phys. **40**, 441 (1965).

[154] G. Gaigalas, T. Žalandauskas, and Z. Rudzikas, At. Data Nucl. Data Tables **84**, 99 (2003).

[155] G. Gaigalas, T. Žalandauskas, and S. Fritzsche, Comput. Phys. Commun. **157**, 239 (2004).

[156] Y. J. Yu, J. G. Li, C.Z. Dong, X. B. Ding, S. Fritzsche, and B. Fricke, Eur. Phys. J. D **44**, 51 (2007).

[157] T. H. Dinh, V. A. Dzuba, and V. V. Flambaum, Phys. Rev. A **78**, 062502 (2008).

[158] R. Smolańczuk, Phys. Rev. C **56**, 812 (1997).

[159] `http://www.nndc.bnl.gov/nudat2`

[160] B. Graner, Y. Chen, E. G. Lindahl, and B. R. Heckel, Phys. Rev. Lett. **116**, 161601 (2016).

[161] B. Fricke, W. Greiner, and J. T. Waber, Theoret. Chim. Acta **21**, 235 (1971).

[162] R. A. Penneman, J. B. Mann and C. K. Jørgensen, Chem. Phys. Lett. **8**, 321 (1971).

[163] P. Pyykkö, Phys. Chem. **13**, 161 (2011).

[164] D. Layzer, Ann. Phys. **8**, 271 (1959).

[165] D. Layzer, Z. Horák, M. N. Lewis, and D. P. Thompson, Ann. Phys **29**, 101 (1964).

[166] B. Edlén, *Handbuch der Physik* (Springer, Berlin, 1964).

[167] W. L. Wiese and A. W. Weiss, Phys. Rev. **175**, 50 (1968).

[168] M. A. Bouchiat and C. Bouchiat, J. de Physique **35**, 899 (1974).

[169] M. A. Bouchiat and C. C. Bouchiat, Phys.Lett. **48B**, 111 (1974).

[170] M. A. Bouchiat and C. Bouchiat, J. de Physique **36**, 493 (1975).

[171] J. W. Rohlf, *Modern Physics from* α *to* Z^0 (USA,Wiley, 1994).

[172] W. Greiner, *Relativistic Quantum Mechanics - Wave Equations* (Springer-Verlag, Berlin Heidelberg, 1990).

[173] W. Greiner, *Quantum Electrodynamics* (Springer-Verlag, Berlin Heidelberg, 1994).

[174] V. A. Dzuba, V. V. Flambaum and C. Harabati, Phys. Rev. A **84**, 052108 (2011).

[175] P. Indelicato, J. Bieroń, and P. Jönsson, Theor. Chem. Acc. **129**, 495 (2011).

[176] I. Goidenko, I. Tupitsyn, and G. Plunien, Eur. Phys. J. D **45**, 171 (2007).

[177] J. M. Amini, C. T. Munger, Jr., and H. Gould, Phys. Rev. A **75**, 063416 (2007).

[178] M. V. Romalis, W. C. Griffith, J. P. Jacobs, and E. N. Fortson, Phys. Rev. Lett. **86**, 2505 (2001).

[179] M. D. Swallows, T. H. Loftus, W. C. Griffith, B. R. Heckel, and E. N. Fortson, Phys. Rev. A **87**, 012102 (2013).